Computational modeling and analysis of complex muscle architecture

by

Dongwoon Lee

A thesis submitted in conformity with the requirements
for the degree of Doctor of Philosophy
Graduate Department of Computer Science
University of Toronto

Abstract

Computational modeling and analysis of complex muscle architecture

Dongwoon Lee
Doctor of Philosophy
Graduate Department of Computer Science
University of Toronto
2015

Muscle architecture is a primary determinant of the muscle function associated with body movement. An assessment of muscle architecture is therefore of great importance, not only for investigating anatomical aspects of muscle but also for predicting its functional capacity. Most muscles have a variable complexity in their architectures, making it challenging to accurately assess them. Previous cadaveric approaches only take into account limited portions of architecture. On the other hand, conventional radiological approaches, such as ultrasonography and MRI, examine two-dimensional projected images. Neither of these approaches provides a thorough understanding of the entire muscle architecture. This may lead to under- or over-estimation of architectural parameters that are significant for both clinical and computational studies. Therefore, the purpose of this thesis is to develop a computational modeling approach to facilitate quantification and reconstruction of complex muscle architecture. Cadaveric specimen data are used to investigate muscle architecture and to reconstruct accurate models. Associated geometric complexity and variation are carefully examined to yield consistent estimation of architectural parameters. This method demonstrates robustness against non-uniformity in the data and consistency over various types of muscle architecture; less than 10% error in PCSA estimation. By incorporating ultrasonographic assessment, this method is extended to approximate muscle architecture in living subjects, which enables estimation of PCSA for *in vivo* muscle in a more consistent manner. Validation experiments demonstrate $0.4 - 8.4$ % estimation errors between the original architecture and its approximation, depending on the anatomical complexity, which provides a practical insight into the quantification of PCSA for *in vivo* muscle.

Acknowledgements

First and foremost, praise and thanks goes to my savior, Jesus Christ, for everything in my life.

I cannot express my gratitude enough for my supervisor, Dr. Kenneth Jackson, for his guidance, encouragement, support and patience during the entire course of PhD studies. Without him, I would never have been capable of completing this project. I would also like to thank my co-supervisor, Dr. Eugene Fiume, who has always kept me motivated, inspired, confident and supported throughout my studies. It has been an honor to be their student. I am also profoundly grateful to Dr. Anne Agur for her invaluable clinical perspective and broad knowledge that greatly strengthened my studies and extended the application of this research. My sincere thanks also goes to Dr. Christina Christara for serving on my thesis committee and patiently providing helpful advice.

I would like to thank my external examiner, Dr. Sid Fels, whose valuable comments and feedback not only helped me to improve my thesis but also gave me insights into potential research projects beyond my PhD. I also owe my gratitude to Azam Khan, who provided me with my first opportunity to pursue computational-human studies during my internship at Autodesk. That initiated my PhD research on computational modeling and analysis of human skeletal muscles. I am also very thankful to Dr. Karl Zabjek, Dr. Sunita Mathur and Dr. Reinhard Zeller for their astute discussions and advice concerning clinical research.

I would like to thank all my collaborators, James Li, Shannon Roberts, Kajeandra Ravichandiran, Mayoorendra Ravichandiran, Dr. Soo Kim, Zain Sohail, Ali Mahdi, Mike Glueck, Jacky Bibliowicz, Dr. Jeremy Mogk, Anton Semechko, Stephanie Shaw, David Parente and all others from both Dr. Anne Agur's lab and Autodesk Research, for all their support and challenging discussions, which have consistently pushed me to be more productive and progressive in my research. Also, my thanks go to the ArtiSynth researchers at UBC, Dr. John Lloyd, Dr. Ian Stavness and Antonio Sanchez, for their insightful discussions about human modeling and simulation, which might be pursued in the future.

I would like to thank my friends in the CS department, Dr. Jingrui Zhang, Meng Han, Dr. Duy Minh Dang, Dr. Mohammad Shakourifar, Bo Wang, Dr. Hyonho Lee, Ben Kim, Kang-Nyeon Kim, Eunbyung Park and many more, for making school life fun and joyful. My special thanks and respect go to Joseph Laszlo for ardently helping me to get through difficult times, whose smile and humor will be missed forever.

Lastly, I wish to thank my parents, Youngil and Junghee, for their unconditional love, constant support and never-ending confidence in me. Also, I owe my gratitude to brothers, Minho

and Jaeho, sisters, Sooeun and Soyeon, and brother-in-law, Jaegyun, for all their support and encouragement. I would like to thank my lovely wife, Susan, for her encouragement, prayer and tremendous patience. Finally, I am very grateful to my beautiful daughter, Chloe, who is my most passionate supporter, but sometimes delivers the toughest critique of my research.

Thank you.

Contents

Chapter 1

Introduction

1.1 Motivation

Skeletal muscle provides force production and excursion capability to drive and stabilize body movement. Improper functioning of skeletal muscle can cause various health issues in the entire body system, such as musculoskeletal disorder and injury. In such cases, correct understanding of muscle is imperative not only to develop effective strategies for muscle injury prevention and therapeutic treatment, but also to plan surgical procedures, such as tendon transfer and replacement surgery. For instance, the surgical outcome of tendon transfer depends on a good matching between donor and recipient muscles that necessitates a careful pre-operative examination. Specifically, an assessment of muscle architecture is essential to evaluate its functional capacity because it is a primary determinant of the muscle function associated with body movement. Thus, it is of great clinical importance to accurately assess muscle architecture.

Accurate assessment of muscle architecture is important, not only for clinical studies but also for computational studies using an analytical model, such as the inverse-dynamics problem for neuromuscular control. The model complexity varies with respect to the purpose and application of those studies. For instance, muscle morphology can be simply represented by a single line segment or modeled in a more sophisticated manner by a detailed surface or volume mesh. Muscle dynamics can be modeled by a simple uni-directional, point-to-point mass-spring model or by a more complicated continuum-based material scheme. Regardless of the complexity and degree of freedom, architectural and structural parameters associated with studied muscles are directly used to build models. Thus, the model performance is highly dependent on the choice and accurate representation of those parameters. In building a muscle model, however, it is common practice to choose reference values reported in the literature or geometric measures simply determined by radiological assessment, such as magnetic resonance imaging (MRI) and ultrasonography. This may lead to imprecise parameter values and hence inaccurate models. For instance, even small changes in architectural parameters, specifically, physiological cross-sectional area (PCSA), may lead to considerable variation in simulation results. Therefore, it

is critical to use reliable modeling based on an accurate parameter estimation.

1.2 Problem statement

Muscle architecture is the geometric arrangement of muscle fascicles (or fibers) at the macroscopic level. An individual fiber is the elementary functional unit for force production and shortening. The functional outcome is aggregated over all fibers to characterize the entire muscle function. Force production per muscle is proportional to the number of fibers or total cross-sectional area of fibers but inversely proportional to the angulation of the fibers relative to the tendon axis. The length of the fiber from proximal to distal attachment determines the excursion limit for the associated joint. As the distribution of the angle and length of fibers are non-uniform in most muscles, the functional properties of muscle are characterized by how fibers are organized and arranged. Thus, the accurate assessment of the muscle architecture must take into account the structural complexity of muscles.

In general, muscle assessment can be classified into the following three approaches: cadaveric, radiological and biomechanical approaches. The cadaveric approach aims to obtain an in-depth understanding of anatomical structure. Detailed analysis can be achieved but it is not straightforward to apply to *in-vivo* studies directly. On the other hand, the radiological approach (e.g., ultrasonography and MRI) is non-invasive, so it is widely used for understanding living tissues. Additionally, it can be used effectively to quantify dynamically changing structural properties during muscle contraction. However, it is inherent that two-dimensional images impose constraints on the capacity to fully understand three-dimensional structure. The biomechanical approach provides functional analysis of muscle associated with skeletal movement. Kinetic and kinematic measures are commonly used to determine functional properties, which consequently permits us to evaluate muscle performance and functional contribution to movement. In contrast to cadaveric and radiological approaches, it may not enable us to quantify the underlying structure of muscle. None of those approaches alone provides a comprehensive understanding of muscle.

Since the focus of this thesis is to investigate architectural and structural aspects of muscle, cadaveric and radiological assessment are the main tools used throughout this thesis to address the following questions:

- How to reconstruct the complex geometry of muscle architecture based on the detailed cadaveric data.
- How to determine and predict functional and physiological properties of muscle from reconstructed muscle geometry.
- How to utilize computational modeling studies for clinical applications.

This thesis is based on existing data (e.g., fascicle data and ultrasound) that were already acquired in other anatomical studies [77, 78, 41, 9, 58, 89, 57, 81]. Thus, the protocol development for data acquisition is not within the scope of this thesis.

1.3 Contribution

The purpose of this thesis is to develop computational modeling approaches to reconstruct and understand the complex architecture of skeletal muscle. Cadaveric specimen data are used to conduct a detailed investigation of muscle architecture and to reconstruct geometric models. Ultrasonographic data are also used to extend this cadaveric modeling, which allows to conduct experiments based on *in-vivo* muscles. This thesis mainly consists of three sub-projects, each of which is presented with a corresponding method development and validation experiments.

First, this thesis presents a computational method to quantify architectural parameters based on cadaveric specimen data. Cadaveric data exhibit greater details in their structure, geometric properties of which have often highly non-uniform and variable complex patterns. Presumably, these complexities are highly correlated with many clinical implications but they are rarely accounted for in previous studies. In contrast, in this thesis, dissection and digitization is used to capture those properties in a more systematic manner, such as structural and volumetric modeling. The proposed method specifically focuses on geometric reconstruction of fascicle trajectory and arrangement within the muscle volume. Associated geometric complexity and variation are carefully examined to yield consistent estimation of architectural parameters, in which no adjustment is needed to deal with inter-subject and inter-specimen variability. Based on those estimated parameters, this thesis also presents a geometric approach to approximate muscle surface and volume.

Second, this thesis proposes a three-dimensional approach to pennation angle (PA) estimation based on geometric analysis of fascicle attachment. It is observed that some muscles (e.g., pennate muscles) exhibit stronger linearity in the distribution of distal attachment, whereas others (e.g., non-pennate muscles) exhibit much weaker linearity. Based on an estimate of the linearity, the proposed method effectively classifies a variety of skeletal muscles into two distinct groups: pennate and non-pennate muscles. This approach also allows to estimate the line of action and PA for a muscle. As the conventional method is based on two-dimensional images (e.g., ultrasonography), its estimation of the line of action and PA is sensitive to how these images are captured by the imaging device. Many studies stress that an anatomical knowledge is needed to manipulate the images correctly. To compare the proposed method to this more traditional approach, 2D ultrasonographic assessment is simulated by controlling the imaging plane to determine associated 2D image features from 3D cadaveric data. This experiment illustrates the correspondence between the architecture in space and its projected images, providing

practical insight into the difficulty of obtaining accurate parameters solely from 2D assessment for muscles having complex and variable architecture.

Third, the proposed cadaveric modeling is extended to understand the architecture of *in-vivo* muscle. Cadaveric assessment allows to reconstruct a detailed muscle architecture in 3D, but may not be directly applicable to *in-vivo* studies. On the other hand, radiological approaches, such as ultrasonography, enable to access the structure of living tissue but, as noted above, its assessment in 2D is limited. The proposed approach is to combine both assessments. More specifically, the 3D architectural model based on cadaveric specimens is geometrically transformed to match the 2D characteristics that can be determined by the ultrasound images in a standard clinical setting. This geometric approach is based on the following assumption: the same muscles in different subjects are sufficiently similar to each other in overall architectural and geometric morphology that inter-subject variability of architecture can be approximated in terms of global characteristics. This approach is validated by applying the transformation approach in three experimental settings: synthetic to synthetic muscles, cadaveric to cadaveric muscles and cadaveric muscle to ultrasound images. The quality of architecture approximation is evaluated by comparing PCSA estimation between muscles.

1.4 Outline of thesis

The subsequent chapters are organized as follows. Chapter 2 briefly outlines basic knowledge of muscle anatomy and biomechanics that are used as background material throughout the thesis. It also reviews existing muscle models that focus on representing muscle morphology. Chapter 3 presents the proposed approach to reconstruction and assessment of muscle architecture, PCSA estimation in particular. Chapter 4 presents the three-dimensional approach to PA estimation based on cadaveric specimens. By comparing it to the conventional image-based approach, it is demonstrated that the proposed method deals with anatomical complexity and variation more effectively than the conventional approach. Chapter 5 presents the geometric approach to reconstruction of muscle surface and volume from estimated architectural parameters. Chapter 6 discusses how to combine the cadaveric model with the radiological approach to obtain better approximations to the architecture of *in-vivo* muscle. It is demonstrate how PCSA of living muscle is estimated by using the proposed combined approach. Chapter 7 concludes with a discussion and some suggestions for future work.

Chapter 2

Background

Muscles are the active tissues in the body that generate forces to drive motion. Depending on their physiological functions, muscles can be classified into three types: cardiac, smooth, and skeletal muscle. Cardiac muscles make up the walls of the heart, while smooth muscles constitute the walls of other organs and blood vessels. Both of these classes of muscle are controlled by the autonomic nervous system and contract without conscious effort. Unlike the first two classes of muscle, skeletal muscle contraction is controlled through the somatic nervous system and, for the most part, is done so consciously. These voluntary contractions produce forces that are transferred to the underlying skeleton, resulting in human body movement. Most research in graphics and related fields, such as biomechanics and robotics, has focused on understanding the physiological features and functions of skeletal muscles. In this chapter, both fundamental and computational aspects of skeletal muscles are briefly reviewed.

Much of the material in this chapter also appears in the publication [48].

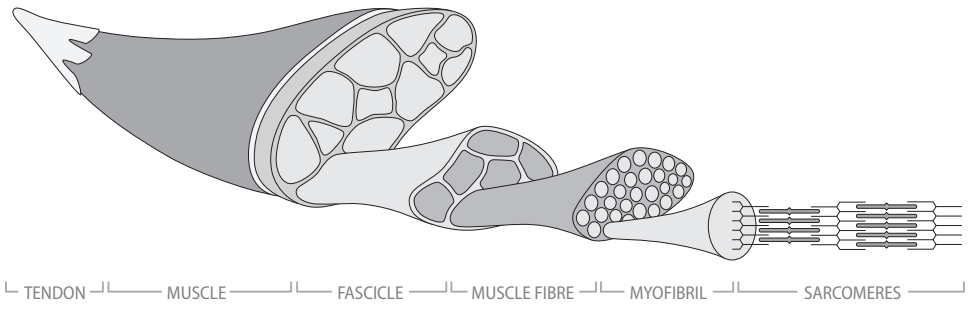

Figure 2.1: Major components of the hierarchical muscle structural system (adapted from Ng-Thow-Hing [69])

2.1 Muscle structure

Skeletal muscles are wrapped by the epimysium, a dense connective tissue that joins with the tendon. Internally, the muscle is composed of numerous muscle fiber bundles, called fascicles, which are separated from one another by a layer of connective tissue known as the perimysium. In turn, every fascicle consists of muscle fibers that are isolated from one another by the endomysium. Similarly, each muscle fiber consists of parallel bundles of myofibrils. Finally, each myofibril is made up of a serial array of contractile units, called sarcomeres, which are responsible for producing the contractions associated with muscles. The hierarchical structure of muscle is illustrated in Figure 2.1. Although fascicles and fibers are often graphically depicted as circular structures, it is important to note the true mosaic-like space-filling pattern of these components.

Another important component to be considered is tendon. It transmits forces produced by the attached muscle to bone. Tendon connects muscle to bone either at a narrow area or over a wide and flattened area, known as the aponeurosis. The attachment of muscle to more stationary bone (i.e., the proximal site) is called the origin while the other end, attached to more movable bone (i.e., distal site), is called the insertion. Tendons are mostly composed of parallel arrays of collagen fibers closely packed together and have the mechanical property that they are much stiffer than muscles when they are pulled. In addition to force transmission, tendons passively modulate force during locomotion, providing additional stability (for example, the Achilles tendon during a human stride).

2.2 Muscle architecture

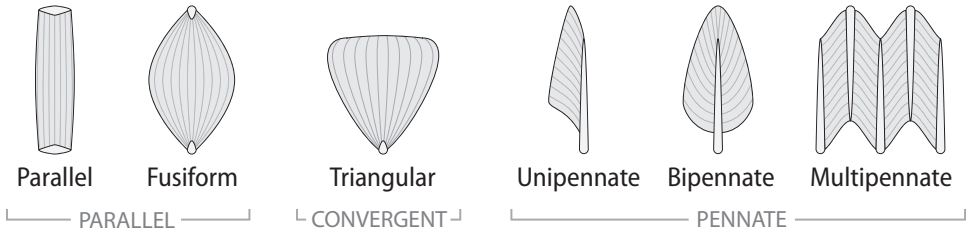

Figure 2.2: Exemplary muscle architecture types (adapted from Ng-Thow-Hing [69])

Muscle architecture refers to the internal arrangement of fascicles within a muscle. Some muscles have simple architectures, in which the fascicles are arranged parallel to one another along the length of the muscle. These are typically the larger muscles, such as biceps brachii. However, most muscles exhibit fascicles with an angular orientation, called the pennation angle, between their tendinous attachments (i.e., line of action) and orientation of each fascicle. Muscles with angular fascicle arrangements are known as pennate muscles. Several types of pennate patterns

are observed in skeletal muscles, as illustrated in Figure 2.2. Parallel muscles can have either longitudinally arranged fascicles (e.g., sartorius) or similarly oriented fascicles with tapering ends (e.g., biceps brachii and psoas major). Unipennate muscles have fascicles arranged in a diagonal pattern on one side of the tendon (e.g., lumbricals and extensor digitorum longus). Bipennate muscles have two rows of fascicles, running in opposite diagonal directions on both sides of a central tendon (e.g., rectus femoris). Multipennate muscles have multiple rows of diagonal fascicles, with a central tendon that branches into two or more tendons (e.g., deltoid). Convergent muscles have wider origin and narrower insertion (e.g., pectoralis major). These differences in muscle architecture determine the range of movement and power produced by a muscle. A muscle would contain a greater number of shorter muscle fascicles in a pennate configuration than in a parallel configuration. As such, pennate muscles do not shorten as much, but can produce more force than parallel muscles of the same size.

Since muscle architecture is a primary determinant for muscle function, it is common that functional capacity of the muscle is inferred from estimated architectural parameters, such as fascicle length (FL), pennation angle (PA), physiological cross-sectional area (PCSA) and muscle volume (MV). Specifically, FL is proportional to shortening velocity of muscle and excursion range for associated joints, because FL reflects the number of sarcomeres in series in the fascicles. PA determines the contribution that muscle fascicles make to the force acting along the attached tendon axis (i.e., the line of action). PCSA is proportional to the maximum capacity of force that muscle can produce. FL is defined as the distance between the origin of the most proximal fascicles to the insertion of the most distal fascicles. Or it is simply defined as the distance between the origin and insertion of one fascicle. PA is defined as the angle between the orientation of a fascicle and the line of action. For each fascicle i, its PA is simply calculated as

$$\mathrm{PA}^i = \cos^{-1}(\text{line of action} \cdot \text{fascicle orientation}^i). \tag{2.1}$$

MV is practically measured by either the sum of volumetric slices obtained from MRI images or using mass and density measures:

$$\begin{aligned} \mathrm{MV}[\mathrm{cm}^3] &= \sum_k C_k \Delta h_k && (2.2) \\ &= \frac{\mathrm{mass[g]}}{\mathrm{density[g/cm^3]}} && (2.3) \end{aligned}$$

where C_k is the area of cross-sectional slice k and Δh_k is the thickness of the slice. PCSA is defined as the sum of the cross-sectional areas of all muscle fascicles within the muscle. In practice, PCSA is simply measured using the algebraic method

$$\mathrm{PCSA}[\mathrm{cm}^2] = \frac{\mathrm{MV}[\mathrm{cm}^3] \cdot \cos(\mathrm{PA})}{\mathrm{FL[cm]}} \tag{2.4}$$

Maximum isometric force, F_0^M, is calculated by

$$F_0^M[\mathrm{N}] = \mathrm{PCSA}[\mathrm{cm}^2] \cdot \text{maximum isometric stress}[\mathrm{N/cm}^2] \tag{2.5}$$

If maximum isometric stress is assumed to be constant (e.g., 45 $\mathrm{N/cm}^2$ [31] or 25−35 $\mathrm{N/cm}^2$ [110]), PCSA is used to compare force capabilities of muscles.

2.3 Assessment of muscle architecture

Muscle architecture is generally investigated by either an invasive cadaveric or a non-invasive radiological approach. The cadaveric approach uses either a formalin-fixed or a fresh cadaveric specimen, whereas the radiological approach uses either ultrasonography or MRI imaging data.

Cadaveric assessment provides a unique opportunity to directly measure architectural properties. Many previous approaches [59, 102] use selectively sampled fascicles from the superficial layer of muscle, FL and PA of which are directly measured using a caliper, goniometer and protractor. On the other hand, PCSA and MV are estimated using (2.4) and (2.3), respectively. For more detailed investigation into architecture, Agur et al. [2], Kim et al. [42] and Rosatelli et al. [79] used dissection to collect fascicles throughout the muscle. Using a MicroScribe G2 digitizer, fascicle trajectories are traced and reconstructed three-dimensionally, which provides an in-depth understanding of muscle architecture. However, due to the invasiveness, the cadaveric approach is not straightforward to apply to *in-vivo* studies.

Ultrasonography produces a grey-scale image based on the variable response of tissue to ultrasonic waves, with hypo-echoic fascicle (dark) and hyper-echoic connective tissue (white). Due to its portability and flexibility, ultrasonography is widely used as a diagnostic tool to assess architectural properties *in-vivo* in both relaxed and contracted states. Specifically, FL, PA and anatomical cross-sectional area are estimated by varying images with respect to the alignment of a hand-held probe. As the parameter estimation is sensitive to the location and orientation of the probe, it is essential to determine the correct imaging plane [11, 76, 66].

MRI generates an oscillating magnetic field that excites hydrogen atoms in the body. The contrast between different tissues is determined by the rate at which those excited atoms return to the equilibrium state. MRI produces a sequence of axial images that are used to measure MV by (2.3) and reconstruct muscle geometry. However, MRI has difficulty in identifying specific muscles and capturing narrow areas.

Diffusion tensor imaging (DTI) produces magnetic resonance images of living tissues sensitized with the local characteristics of molecular diffusion: specifically, estimates of the rate of water diffusion at a spatial location. Thus, DTI effectively visualizes fibrous structure of living tissue,

such as brain and muscle. Since DTI is a non-invasive method, it enables *in-vivo* quantification of muscle architecture throughout the volume without any tissue damage [55, 26, 84]. However, it has some limitations related to low signal-to-noise ratio (SNR) and difficulties in differentiating between other connective tissues.

2.4 Muscle contraction

Muscle contraction is controlled by the central nervous system; nerve impulses originate from and travel down the motor neurons to the sensory-somatic branch in the muscle. The place at whitch the terminal of a motor neuron and a muscle fiber connect is called the neuromuscular junction. Each motor neuron innervates a set of muscle fibers in which the nerve impulses stimulate the flow of calcium into the sarcomeres, causing their filaments to slide [39]. Sarcomeres have protein-based structures composed of high-tensile "thin" filaments of actin and "thick" filaments of myosin. They are alternatingly stacked on one another and interact via cross-bridges to produce force. The sliding filament and cross-bridge theory [36, 37] describes the process of muscle contraction. During muscle contraction, the lengths of these filaments remain constant and slide past each other to increase their overlap, producing an overall shortening effect in the muscle, as illustrated in Figure 2.3. The myosin heads are considered to be elastic elements which oscillate about an equilibrium position (i.e., position of attachment to the myosin filament) due to biochemical energy. They are linked as the cross-bridges to the myosin binding sites located in the actin filament. When the heads oscillate, they continuously attach or detach from the myosin binding site. When they attach, they exert forces on the actin filaments, causing filaments to slide past each other. Muscle contraction can be classified according to length change or force level. In isotonic contraction, muscle length changes while producing force; the muscle either shortens (i.e., concentric contraction) or lengthens (i.e., eccentric contraction) depending on whether the produced force is sufficient to resist an external load. In isometric contraction, muscle length remains unchanged while producing force, as, for example, when holding up an object without moving.

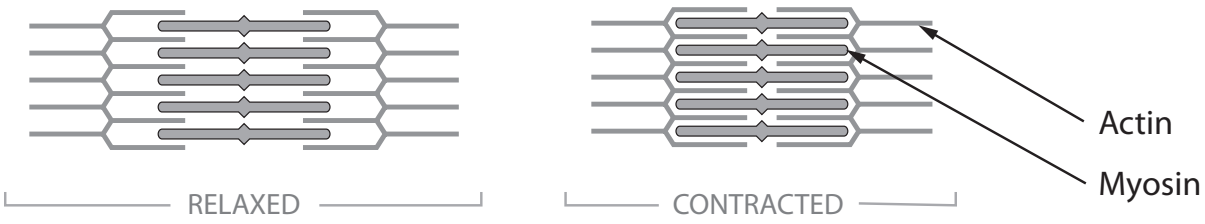

Figure 2.3: During concentric muscle contraction, the sarcomere shortens as filaments of myosin pull along the rigid filaments of actin. The more the filaments overlaps, the more the sarcomere thickens (adapted from [39]).

2.5 Functional properties of muscle

Functional properties of muscle associated with dynamic force development can be obtained from simple experiments using muscle isolated from tendon [28]. Two fundamental properties, force-length and force-velocity, have been frequently incorporated into a variety of biomechanical models to understand muscle function.

When the whole muscle is stretched or shortened to several different lengths (force-length property), the resulting force output is measured and plotted against the length. With no muscle activation, muscle only develops passive restorative force against increased stretching. With muscle activation, muscle contracts and generates active force. The total force is the sum of both active and passive forces (see Figure 2.4(a)). The curves for these forces are approximated in various ways, such as piecewise line segments [109], piecewise cubic splines [21] or quadratic functions [99]. The active force is found by subtracting the passive force from the total force. The non-linear force-length relationship is consistent with the sliding filament theory of muscle contraction.

The force-velocity property of muscle is the relationship between the velocity at which muscle shortens and the amount of force it produces (plotted in Figure 2.4(b)). To quantify this relationship, a fully activated muscle is clamped isometrically and then suddenly released to allow shortening against an external load. When there is no load on the muscle, the maximum velocity of shortening is experienced. As the external load increases, the velocity of shortening decreases. The curve for this property is modeled by following hyperbolic equation (which is also known as the Hill equation) [33]:

$$(F + a)(v + b) = (F_0 + a)/b \tag{2.6}$$

where F is the force generated by the muscle, v is the velocity of shortening, F_0 is the maximum isometric force, a and b are constants related to a specific class of muscle. This property is arguably thought to be associated with the dependence of muscle force on the number of attached cross-bridges [39]. During muscle contraction, cross-bridges attach to produce forces. Since it takes some amount of time for them to attach, as filaments slide past one another more quickly (i.e., muscle shortens with increasing velocity), the produced force decreases due to the lower number of attached cross-bridges. Conversely, as the relative velocity of filaments decreases (i.e., muscle shortens with decreasing velocity), more cross-bridges can attach, producing more force.

Another important property of muscle is line of action, which determines functional constraints on the behavior of muscle. There are two common methods to represent the line of action:

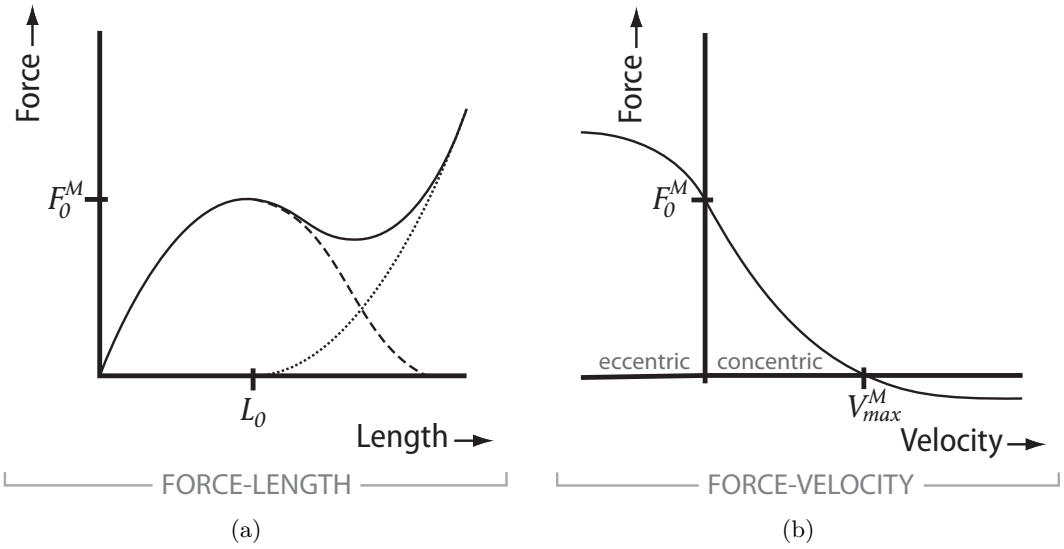

(a) (b)

Figure 2.4: Functional properties of muscles associated with force development (adapted from [109]). (a) A sample force-length plot shows the passive elastic (dotted), active (dashed), and total (solid) force generated by a muscle against its length. F_0^M is the maximum isometric force and L_0 is the rest/optimal length. F_0^M is experienced at L_0. (b) A sample force-velocity plot shows the force a muscle generates against the velocity of muscle contraction. V_{max}^M is the maximum shortening velocity.

piecewise line segments [22] and centroid curves [38]. Piecewise line segments specify the path of muscles to tendinous attachments. They can be wrapped around the joints or pass through the tendon sheaths. Centroid curves are constructed by interpolating approximate centroids of cross-sections throughout the muscle.

2.6 Modeling muscle contraction

A simple and phenomenological mechanical model (shown in Figure 2.5(a)) was suggested by Gasser and Hill [28] to capture the mechanical properties of muscle discussed above. This model has three major components: the series element (SE), the parallel element (PE), and the contractile element (CE). The series element (SE) represents mainly the elastic effects of tendon and intrinsic elasticity within the sarcomere. The parallel element (PE) represents the passive elasticity of the muscle resulting from the penetration of connective tissues into the muscle body. The contractile element (CE) accounts for generation of active force that is dependent on the muscle length, l^M, and the time-varying neural signal, $a(t)$, originating from the central nervous system. The Hill model was later refined by Zajac [109] to be a dimensionless aggregate or "lumped" model that can be scaled easily to represent any skeletal musculotendon unit. The force components are modeled from the measurement of isolated muscle fibers, which directly reflect the non-linear properties due to the sliding filaments. While the series elastic element can be lumped with the tendon and removed from the model, pennation effects are directly

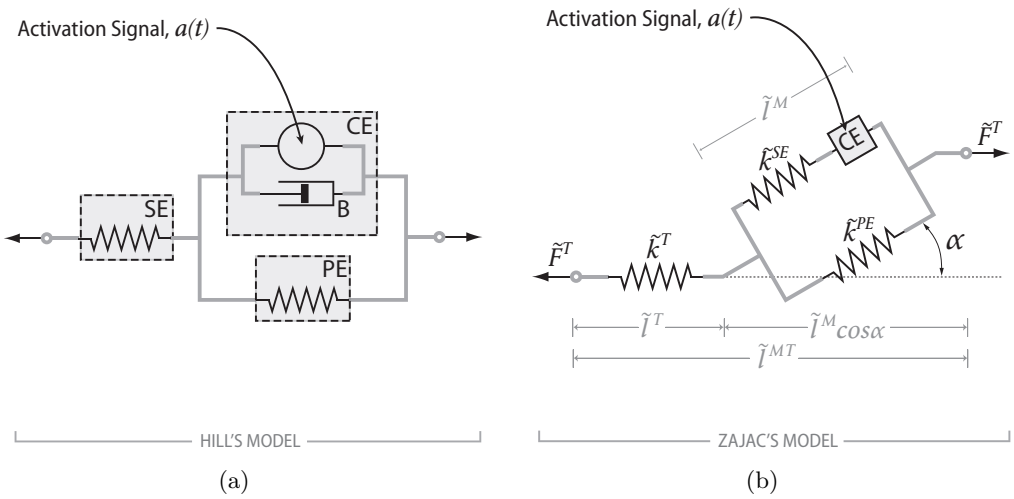

Figure 2.5: Mechanical muscle models (adapted from Chen and Zeltzer [21]). (a) Hill's model describes the force of a muscle contracting as the sum of three elements: the contractile element (CE), the series elastic element (SE) and the parallel element (PE) along with the viscous element (B) that depends on the shortening velocity. (b) Zajac's model extends Hill's model, adding the pennation angle, α, of a muscle fiber.

included into the model. In Zajac's model, muscle length, l^M, tendon length, l^T, muscle force, F^M, and shortening velocity, v^M, are respectively normalized as

$$\tilde{l}^M = \frac{l^M}{l_0^M}, \qquad \tilde{l}^T = \frac{l^T}{l_s^T}, \qquad \tilde{F}^M = \frac{F^M}{F_0^M}, \qquad \tilde{v}^M = \frac{v^M}{v_{max}^M}$$

where l_0^M is optimal muscle length at which F_0^M is developed, l_s^T is tendon rest length, F_0^M is the maximum isometric force of active muscle, and v_{max}^M is the maximum shortening velocity of muscle fibers. The relationship between muscle and musculotendon length is

$$\tilde{l}^{MT} = \tilde{l}^T + \tilde{l}^M \cos\alpha$$

where α is the pennation angle (see Figure 2.5(b)). The normalized active force $\tilde{F}_{active}^{CE}$ and passive force $\tilde{F}^{PE}$ can be approximated from the characteristic curves of force-length and force-velocity (shown in Figure 2.4). The production of contractile force $\tilde{F}^{CE}$ is the $\tilde{F}_{active}^{CE}$ scaled by activation level, $a(t)$, varying with time t, and the force-velocity relation, $F_v(\tilde{v}^M)$:

$$\tilde{F}^{CE} = a(t) F_v(\tilde{v}^M) \tilde{F}_{active}^{CE}(\tilde{l}^M)$$

Finally, the total force generated by the whole musculotendon unit is

$$\tilde{F}_M = (\tilde{F}^{CE} + \tilde{F}^{PE}) \cos \alpha$$

Another commonly used muscle model is the Huxley model [36] which combines the sliding filaments and cross-bridge theory that is reviewed in Section 2.4. While the Hill model has been used to describe macroscopic behaviors of muscle, the Huxley model has been used mainly to understand the properties of the microscopic contractile elements. To describe muscle contraction, the actin-myosin bonding reaction is expressed using first order kinetics as

$$\frac{dn}{dt} = \frac{\partial n}{\partial t} - v(t)\frac{\partial n}{\partial x} = (1-n)f(x) - ng(x). \tag{2.7}$$

Here, the function $n(x,t)$ is proportional to the number of attached cross-bridges with displacement x at time t, $v(t)$ is the velocity of contraction of a half sarcomere, $f(x)$ is the rate of attachment and $g(x)$ is the rate of detachment. The displacement x is the distance between the equilibrium position and the myosin binding position located in the actin filament. The cross-bridge is defined as the cross-link between the myosin head and the myosin binding position and its behavior is modeled using a Hookean spring. The total force exerted by muscle is calculated by summing the forces contributed by each bonded cross-bridge as

$$F(t) = \frac{mkAs(t)}{2l} \int_{-\infty}^{\infty} xn(x,t)dx \tag{2.8}$$

where m is the number of cross-bridges per unit volume, k is the spring constant, A is the cross-sectional area of the muscle, $s(t)$ is the sarcomere length and l represents the distance between successive binding positions.

2.7 Modeling muscle morphology

Muscle is not only a functional unit that drives body movement, it is also a fundamental component in defining the visual appearance of the human body. As such, realistic muscle deformation is needed for high-quality animated human characters. Several approaches have been proposed to model either muscle deformation or muscle-driven body deformation. Their application can be used to simulate different scales of systems, from a single muscle to an entire body. Based on their underlying fundamental methodology, these approaches are classified into three categories: geometrically-based, physically-based, and data-driven approaches.

2.7.1 Geometrically-based approaches

Geometrically-based techniques were employed in early systems because they are practical and efficient. Most proposed approaches have focused on modeling animation effects of muscle contraction, such as bulging or swelling, which can be key underlying factors for skin deformation or facial animation. They have been shown to be successful in modeling simple muscle (e.g., fusiform) but there may not be a straightforward extension to complex muscles [104, 83]. Furthermore, since muscle deformation is determined by skeleton arrangement, these techniques have difficulty in achieving a high order of realism from physiological or biomechanical perspectives. Thus, to better handle these problems, muscles are constructed as multiple layers or are often coupled with other physically-based approaches (see Section 2.7.2).

Space and free form deformation

A space deformation is a mapping from an input domain to a target domain within an Euclidean space, in which geometric control is manipulated to satisfy specified constraints. The Free Form Deformation (FFD) technique places a lattice around an object and creates a deformable space by using a trivariate Bézier volume defined by the points of the lattice [85]:

$$X(u,v,w) = \sum_{i=0}^{l}\sum_{j=0}^{m}\sum_{k=0}^{n} B_i(u)B_j(v)B_k(w)P_{ijk},\ \ 0 \le u,v,w \le 1 \tag{2.9}$$

where $B_i(u), B_j(v)$ and $B_k(w)$ are separable Bernstein polynomials and P_{ijk} is a point of the lattice (i.e., control point) and $X(u,v,w)$ is a deformed point (i.e., spatial point). Chadwick et al. [20] employed FFD to represent muscle deformation. Articulated skeletons, located inside muscle, transform a surrounding FFD lattice, which in turn represents a muscle shape change. Although FFDs provide simple and fast control, they do not permit direct manipulation of muscle shape. Also, the regular lattice spacing used by FFD prevents the detailed control needed to produce more refined and complex shapes (see Figure 2.6). Moccozet et al. [63] addressed this limitation by introducing Dirichlet Free From Deformation (DFFD) which is based on a scattered data interpolation technique. They removed the requirement for regularly spaced control points by replacing rectangular local coordinates by generalized natural neighbor coordinates (namely, Sibson coordinates). Given a point, its natural neighbors are collected based on Delaunay and Dirichlet/Voronoi diagrams and its displacement is computed using interpolation. They used a multi-layered deformation model to illustrate hand animation in which the muscle layer is modeled by a DFFD control point set corresponding to a simplified hand topography. In Skeleton-Subspace Deformation (SSD), deformation of surface points is determined by the weighted summation of the associated skeleton coordinate transformations. Muscle bulging or swelling can be modeled by manually defining skeleton subspaces and adjusting weights. Lewis et al. [56] introduced the Pose-Space Deformation (PSD) by generalizing the interpolation domain, which can be defined by a skeleton or even expression parameters.

They improved upon the blending problem, in which neighboring subspaces might incorrectly blend together in SSD, and permitted direct manipulation of the desired deformation.

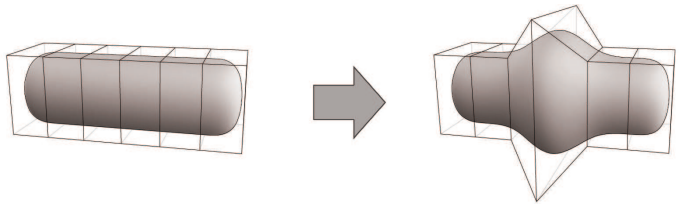

Figure 2.6: An exemplary FFD surface is defined by a control lattice around the muscle shape surface. (Left) The FFD surface before deformation. (Right) The FFD surface after deformation.

Parametric and polygonal surfaces

A parametric surface is represented by either parametric equations to control shapes or a collection of surface patches which are defined in terms of bivariate and single valued equations (i.e., $x = x(u, w), y = y(u, w), z = z(u, w)$). A polygonal surface is an approximate and discretized surface represented by many simple geometric primitives, such as vertices, edges and faces.

Komatsu [44] used biquartic Bézier surfaces to model body deformation. The Bézier surfaces are patched cylindrically around the skeleton and are jointly controlled to transform the body. Wilhelms [104] and Scheepers et al. [83] used a parametric ellipsoid as a basic primitive to model human skeletal muscles. Three principal axes are adjusted to represent the bulging of the muscle belly, while volume is preserved with respect to constrained ratios using predefined relationships among these three axes. Although an ellipsoid is sufficient for modeling simple shapes, such as fusiform muscle, it cannot be easily adapted to model more complex muscle shapes. Scheepers et al. extended their model to represent multi-belly muscles (e.g., pectoralis) in which n pairs of origin and insertion points are specified and n ellipsoids are laterally aligned along the path within the corresponding pair. Their model is further generalized to represent more complex muscles which are bent and wrapped around anatomical structure (e.g., brachioradialis in the forearm). The straight path between the origin and the insertion point is replaced by a cubic Bézier curve representing the direction of muscle force and ellipses of varying size along this curve to define the volume and shape of the muscle. Dow and Semwal [24] proposed the generalized cylinder based muscle model, in which muscle is represented by a cylinder axis and surrounding cross-sectional slices. The contour of each slice is modeled by B-spline curves and its radius is controlled to express volumetric changes of muscle (see Figure 2.7). Wilhelms and Gelder [105] presented a similar approach with the additional flexibility that a cylinder axis can be bent for modeling muscle bent over a joint. Furthermore, the muscle length, width and, thickness are scaled to maintain constant volume. Ng-Thow-Hing and Fiume [70, 69] used B-spline solids in which a cylindrical coordinate system is chosen to construct a control point

lattice from real specimen data. Their geometric parameterisation can model realistic muscle shape and also depict muscle fibers inside the muscle.

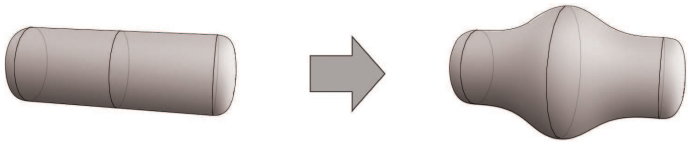

Figure 2.7: An exemplary parametric and polygonal surface: a muscle shape is defined by control of a set of cross-sectional slices. The surface before deformation (left) and after deformation (right).

Implicit surfaces

An implicit surface generated by a set of skeletons, s_i $(i = 1, 2, \cdots, n)$, with associated field functions, f_i, is defined at the isovalue c by

$$\{P \in \mathbb{R}^3 |\ f(P) = c\}, \quad \text{where } f(P) = \sum_{i=1}^{n} f_i(P). \tag{2.10}$$

The skeleton, s_i, can be any geometric primitive such as a point, a curve, a parametric surface, etc. The field function, f_i, is generally a decreasing function of the distance from a given point, P, to the associated skeleton (see Figure 2.8). Based on the type of field function, various implicit surfaces have been developed: blobs, metaballs, soft objects, and convolution surfaces [15, 106, 16].

Bloomenthal et al. [16] used convolution surfaces to model the human hand and arm by approximating bones, muscles, tendons and veins close to the underlying skeletons. Thalmann et al. [96] presented the multi-layered human model whose body primitives (e.g., muscle, limb, and fatty tissue) are additively constructed from a stick figure skeleton model and coated with the ellipsoidal metaball surfaces. Although the implicit surfaces are smooth and continuous in modeling objects, unwanted blending effects may often occur in modeling deformation over joints. This problem can be avoided by defining neighboring areas between the different skeletons, and specifying how the contributions from them are to be summed (e.g., blending graph [18] and weighted blending with the proximity [87]).

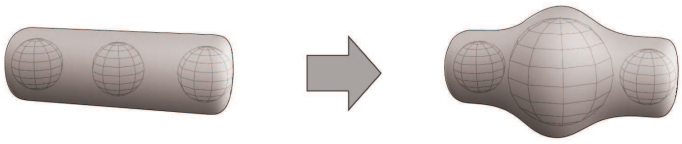

Figure 2.8: An exemplary implicit surface is defined by the sum of field functions around associated spherical skeletons. The surface before deformation (left) and after deformation (right).

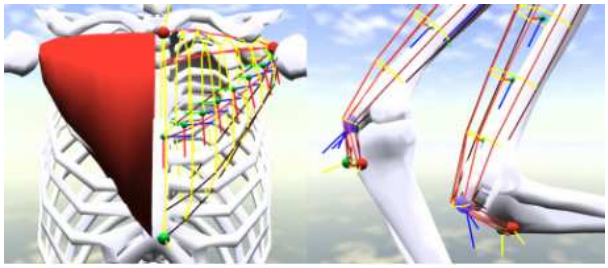

(a)

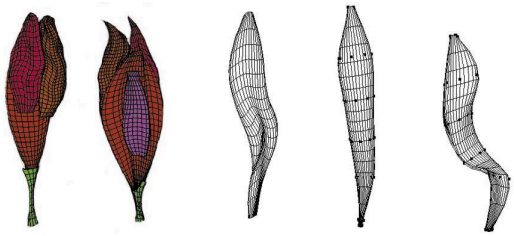

(b)

Figure 2.9: Geometrically-Based Approaches (a) deformed cylinders [104] and (b) B-Spline solids [69]

2.7.2 Physically-based approaches

While geometrically-based models have proven to be sufficient for some graphical applications demanding visually acceptable quality, their inherent simplicity and the need for human intervention often makes it difficult to extend them to represent complex scenes involving dynamics. Furthermore, they lack the physical or mechanical accuracy often required for realistic modeling and simulation. To overcome these deficiencies, many researchers have turned to physically-based approaches in which physical simulation is employed to solve for complex interactions involving muscle dynamics and tissue properties. To model physically-based muscles, the following two problems must be addressed: (1) determining the contractile muscle forces and (2) representing the changing muscle geometry during the contraction. To solve these problems, several muscle models have been proposed based on a variety of computational methods, such as mass-spring systems, FEM (Finite Element Method), and FVM (Finite Volume Method).

Mass-spring system

An object is modeled by a collection of point masses linked together with massless springs. An elastic force acting on mass i connected by a spring to mass j is given by

$$\mathbf{f}_{ij} = k(|\mathbf{x}_{ij}| - l_{ij})\frac{\mathbf{x}_{ij}}{|\mathbf{x}_{ij}|} \tag{2.11}$$

where $\mathbf{x}_{ij} = \mathbf{x}_j - \mathbf{x}_i$, and $\mathbf{x}_i$, $\mathbf{x}_j$ are the locations of point masses i and j, respectively, l_{ij}

is the rest length between them and k is the spring's stiffness. This linear spring model can be generalized by incorporating various types of spring forces, such as angular, bending, and shearing. Each force is derived from an energy minimization principle and serves as a constraint to cause the desired deformation effects.

Chadwick et al. [20] linked FFD control points to point masses in a mass-spring system, allowing this dynamic system to influence the geometrically-based deformation. By augmenting their FFD-based muscle model with a mass-spring system they were able to represent the viscoelastic properties that articulated skeleton-driven deformation often lacks. Lee et al. [52] and Albrecht et al. [3] embedded a muscle layer based on a mass-spring system between the skin surface and the skeleton structure to model facial expressions and hands, respectively. Spring forces generated by the movement of bones in the skeleton caused the attached skin surface to deform realistically. Nedel and Thalmann [68] and Aubel and Thalmann [10] proposed a two-layered muscle model consisting of a line of action and the muscle surface. The line of action is modeled using either a straight line [68] or a 1D mass spring [10] to define the profile of the muscle (e.g., orientation and bone attachment). The skeleton kinematically controls the line of action to deform the surrounding muscle surface based on a mass spring system (see Figure 2.10(a)). Besides linear springs representing the surface, angular springs have been incorporated to control the volume of the muscle [68]. Ng-Thow-Hing and Fiume [70, 69] proposed a more sophisticated model based on anatomical and biomechanical considerations. Their solid muscle is extracted from medical imaging data or cross-sectional sliced images (e.g., Visible Human [1]) and modeled using volumetric B-splines. For interior details, a muscle fiber architecture is constructed based on digitally scanned fiber data. While a Hill-based model is employed to express the dynamics of muscle fiber, a mass-spring system is used to represent viscoelastic deformation of muscle. Zordan et al. [114] developed a human torso model to animate breathing motions, such as inhalation and exhalation. The interplay of rib cage, diaphragm, and abdomen muscles while breathing was described based on respiration mechanics and was simulated using a mass-spring system (see Figure 2.10(b)). Furthermore, in order to preserve the volume of the human body, pressure forces based on anticipated volume change were incorporated. Delp et al. [23] used a set of line segments to define behavior of muscles. Additionally, wrapping surfaces (e.g., ellipsoids and cylinders) are employed to impose geometrical constraints, preventing muscles from penetrating into other surrounding tissues.

Finite element method (FEM)

In the finite element method (FEM), a body is subdivided into a set of domains or finite elements (e.g., hexahedra or tetrahedra in 3D, quadrilaterals or triangles in 2D). Displacements and positions in an element are approximated from discrete nodal values using interpolation functions:

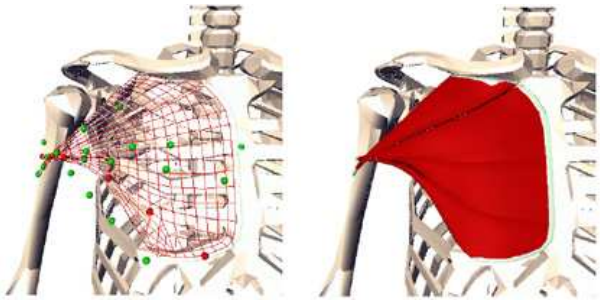

(a)

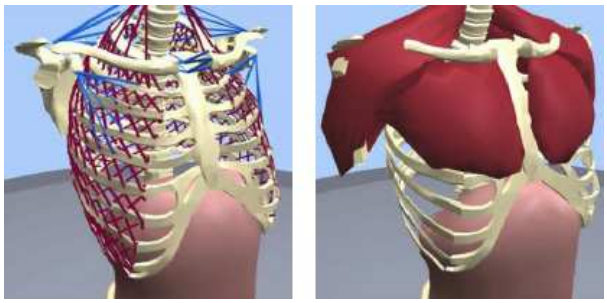

(b)

Figure 2.10: A mass-spring system is used to simulate behaviors of lines of action and wrapped surfaces of (a) pectoralis muscle [10] and (b) torso model [114]

$$\Phi(\mathbf{x}) \approx \sum_i h_i(\mathbf{x})\Phi_i \tag{2.12}$$

where h_i is a basis function and Φ_i is the scalar weight associated with h_i. There exist many choices for the element type and the basis functions. The choice depends on the object geometry, accuracy requirements, and computational budget. Higher order interpolation functions and more complex elements require greater computation per element, but may give a more accurate approximation. For a more complete discussion of the FEM, see [92]. Given a dynamic problem to be solved, equilibrium equations are derived in terms of quantities of interest (e.g., strain or stress) and are expressed as Partial Differential Equations (PDEs). These PDEs are then approximated by the FEM. For example, to represent solid deformation, the total strain energy as the potential energy is carefully designed to express desired material response and then equilibrium equations are derived according to the principle of *virtual work* [29, 67]. Resulting algebraic equations form a linear or nonlinear system, depending on the specified strain energy. While smaller linear systems can be solved by direct methods (e.g., Gaussian Elimination), large or nonlinear systems require iterative methods (e.g., Conjugate Gradient or Newton's method) [75].

Chen and Zeltzer [21] proposed a biomechanical approach by integrating a Hill-based muscle

model into a linear elastic solid model. Active muscle forces are approximated as parametric functions and embedded into selected edges between vertices of a FEM-based solid. While they animated flexion of muscles, they emphasized the biomechanical validity of their model by comparing it to experimental measurements, such as the force-length and quick-release properties. Zhu et al. [112] employed Stern's muscle model [91] in which simplified behaviors of bone-joint-muscle complexes are described. Both works employed a linear elastic material model for connective passive tissues of muscle, which is computationally efficient but valid only for infinitesimal deformation. In contrast, Hirota et al. [34] and Lemos et al. [53] adopted nonlinear material models that allowed the robust representation of large deformations. Hirota et al. combined the Mooney-Rivlin model [64], the Veronda model [101] and the fiber-reinforcement material model [43] to express passive response of tissues during body contact. Lemos et al. [53] used a rubber-like material model (e.g., hyperelastic material) and explicitly aligned Hill-based muscle forces to fiber orientations within the finite elements.

In biomechanics, FEM has been widely investigated for studying skeletal muscles. Various muscle models have been proposed to analyze and predict accurate strain distribution of muscle during contraction and its functional properties. Yucesoy et al. [107] modeled the mechanical behavior of skeletal muscle as the interaction between the intracellular domain (i.e., muscle fibers) and extracellular matrix domain (i.e., connective tissues). Thus, muscle geometry is represented by two separate meshes that are elastically linked to account for the force transmissions between these two domains. Blemker and Delp [12] and Blemker [14] developed a way to represent complex muscle geometry and architecture (see Figure 2.11(a)). A variation of the moment arms of fibers is modeled and the predicted changes to muscle shape are compared to magnetic resonance images. Tang et al. [93] proposed a constitutive muscle model in which active contraction of muscle fibers and hyperelastic material properties are coupled using the strain energy approach. They demonstrated different types of contractions, such as concentric and eccentric contractions, and effects of muscle geometry and fiber orientation on the stress distribution. Gielen et al. [30] and Oomens et al. [71] incorporated the Huxley model to represent contractile properties of skeletal muscle. The Huxley equations (Equation 2.7) are approximated using a Distribution Moments approach [108] and combined with the constitutive equation describing nonlinear and incompressible material response.

Finite volume method (FVM)

As with FEM, the finite volume method approximates PDEs piecewise by algebraic equations. More specifically, for the integration of conserved variables in PDEs, volume integrals are converted to surface integrals using the divergence theorem. These terms are then evaluated as fluxes at the surfaces of each finite volume. For example, computation of the internal force $\mathbf{f}$ at node $\mathbf{x}_i$ uses

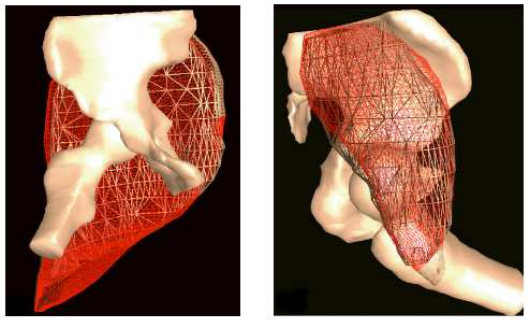

(a)

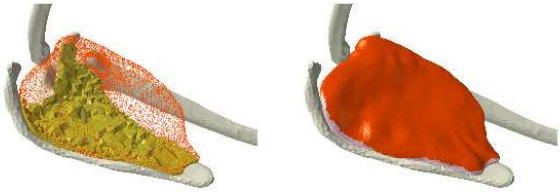

(b)

Figure 2.11: Physically-based Approaches: (a) gluteus maximus and medius muscle models with the hip extension and flexion (based on FEM, [14]) and (b) subscapularis muscle model attached to scapula bone model (based on FVM, [95])

$$\mathbf{f}_i = \frac{d}{dt}\iiint_{\Omega_i} \rho \mathbf{v} d\mathbf{x} = \frac{d}{dt}\iint_{\partial\Omega_i} \mathbf{t} dS = \frac{d}{dt}\iint_{\partial\Omega_i} \sigma \mathbf{n} dS \tag{2.13}$$

where Ω_i is a small volume containing $\mathbf{x}_i$, ρ is the density, $\mathbf{v}$ is the velocity, $\mathbf{t}$ is the surface traction on $\partial\Omega_i$, σ is the stress tensor, and $\mathbf{n}$ is the surface normal. From left to right in (2.13), note that a volumetric integral, requiring velocities and densities to be defined at every point in space, is replaced by a more tractable surface integral involving a stress tensor and a normal to the surface. For a more complete discussion of the FVM, see [54].

Teran et al. [94, 95] proposed a FVM-based approach to simulate deformable behavior of skeletal muscles (shown in Figure 2.11(b)). They argued that FVM inherently requires less computation and memory usage than FEM does. Moreover, they showed that FVM provides a geometric interpretation of stress inside the object (i.e., multidimensional forces pushing on each face of an element), allowing for a simpler and more intuitive way of integrating equations of motion compared to FEM. To represent highly nonlinear material response of muscle, they used a sophisticated constitutive model similar to [34]. Furthermore, they incorporated anisotropic properties based on fiber architecture, which are modeled using the B-spline solid technique [70].

2.7.3 Data-driven approaches

In contrast to many methods involving the modeling of physical human components and processes, some data-driven approaches forego anatomical mechanisms and directly model the skin shape in an 'outside-in' manner, deformed by the underlying muscle of a human in plausible poses. Data is captured on the surface of subjects, usually with markers on the skin, by a motion capture system or a range scanning device. Several techniques may then be used to generate a new skin surface given a novel skeleton pose. Although such data-driven approaches are relatively new, several key papers have already shown the power of this technique.

Early work by Min et al. [62] is based on the observation that skin shape in a human scan is determined by the underlying skeleton and muscle, and uses an anatomically-based approach having layers of skeleton, muscle, and skin. Moving the skeleton deforms the isosurface muscle in a volume-preserving fashion, which in turn deforms the skin layer. The upper body was modeled and the resulting animation showed realistic arm bending and stretching. Another approach to arm animation by Sloan et al. [88] used several exemplary arm shapes and a unique interpolation scheme using linear and radial basis functions to create a continuous range of well-behaved poses.

As example poses of human subjects became more accessible, more ambitious systems were created [60]. In the range-scanning technique, a person poses for a short time as a scanner creates tens of thousands of data points on the surface of the subject at a density of just a few millimeters. Allen et al. [5] created a high quality posable upper body model from range scan data together with many correspondence markers. This work was later expanded [6] to accommodate the large CAESER (Civilian American and European Surface Anthropometry Resource project) database of whole-body range scans, resulting in a compelling system with several desirable features. Morphing by interpolating between registered scans or fitting a model to a sparse marker set are two significant outcomes of this technique. The technique also supports transferring texture, surface data or animation between models to correct scanning problems, to alter the appearance, or to animate the characters. Multiple correlated parameters could be modified, such as a person's weight or height, or statistically correct human shapes could be preserved when locally modifying a character part, for example, lengthening an arm.

There are many steps involved in creating the reconstruction and parameterization of the CAESER data sets. Previous techniques, which were used primarily on morphable face models, are based on cylindrical mappings that could not be adapted to a complex branching object, like the complete human body. This work used an artist-generated template object together with a non-rigid registration technique to create a vertex correspondence between a set of skin surfaces that have substantial variation in shape, but a common overall human structure. An energy-minimization approach was used with a weighted sum error objective function that com-

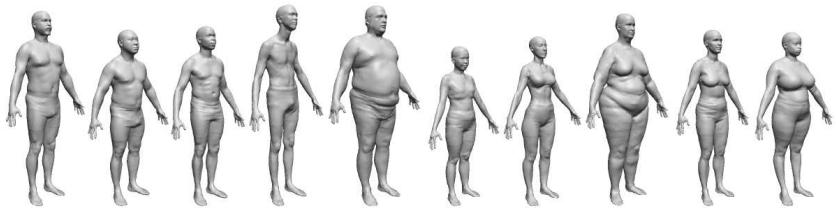

Figure 2.12: Data-driven approach: statistical model [6]

bines distance to a template object, smoothness, and marker distance.

Seo and Thalmann [86] presented a similar template-based system with additional tailoring parameters to generate new, instantly animatable, high-quality human forms, ideal for fashion design. An alternate technique uses many silhouettes from a video stream instead of range scan data to formulate the human shape in a re-animatable form [82]. Anguelov et al. [8] extended this work, focusing on representing muscle deformation resulting from articulated body motion, to perform Shape Completion and Animation of People (SCAPE), by using separate models for pose deformation and for body shape variation. By decoupling the skeleton (rigid) deformation from the muscle (non-rigid) deformation, the formulation, identification of the model, and the efficiency of the learning algorithms are all improved. A limitation is that a single muscle deformation model is used for all people so that a more muscular person may not exhibit as much muscle deformation as they should.

Data-driven modeling of skin and muscle deformation was further refined by Park and Hodgins [73, 74] by modeling static deformations, as a function of skeleton pose, and dynamic deformations, as a function of the acceleration of each body part. Animated motions of an actor were captured using a high density of 350 markers, while performing slow motions and then fast motions. The two classes of deformation were then modeled and new animations could be generated from more typical marker counts (40 to 50 markers) in additional motion-capture sessions. Although this approach still has the limitation of being skeleton-driven and does not express muscle motion without joint angle changes, it does produce very high quality results.

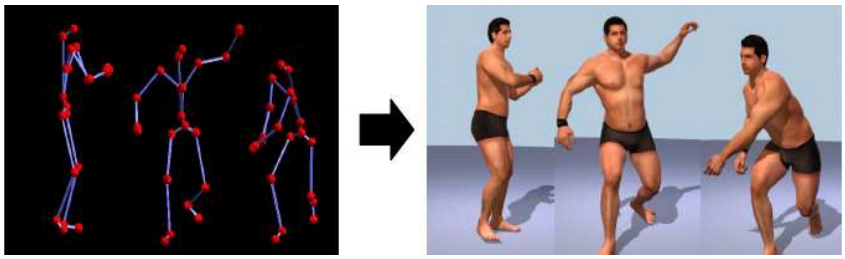

Figure 2.13: Data-driven approach: motion-capture [74]

Chapter 3

Estimation of physiological cross-sectional area for skeletal muscle

3.1 Introduction

Skeletal muscle has been actively studied in biomechanics to discover its mechanical functions associated with body movement. As muscle functions are closely related to architectural parameters [109], such as pennation angle, fiber length and physiological cross-sectional area (PCSA), musculoskeletal simulation needs their accurate determination. Current biomechanical modeling techniques rely on PCSA to estimate peak muscle force production during body movement [72, 7]. Force predictions are known to be highly sensitive to changes in PCSA [17]. Hence, accurate PCSA determination is important for reliable modeling and simulation. In contrast to pennation angle and fiber length, which can be directly measured, PCSA is generally not straightforward to calculate because the functional capacity of all fibers inside the muscle must be accounted for. Ideally, a cross-sectional plane can be specified with respect to the anatomical axis to identify a complete set of cross-sections of all fibers. In parallel muscle, PCSA is usually well determined in the anatomical plane transverse to the longitudinal axis of the muscle. For other muscles having more complex architecture, such as pennate and convergent muscles, an appropriate plane in which to determine PCSA may not be so easily defined [77] (See Figure 3.1). Therefore, for robust estimation of PCSA, the underlying muscle architectural variations must be carefully taken into account.

In most muscle models, PCSA is calculated simply as [4, 80]

$$\text{PCSA}[\text{cm}^2] = \frac{\text{mass}[\text{g}] \cdot \cos(\text{pennation angle})}{\text{density}[\text{g/cm}^3] \cdot \text{fiber length}[\text{cm}]} \tag{3.1}$$

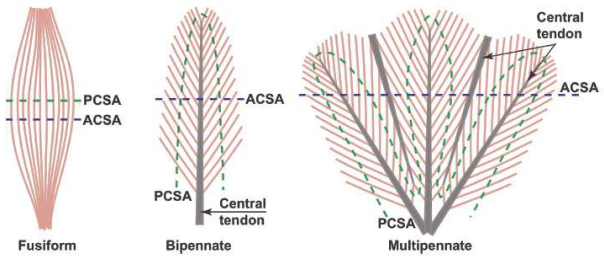

Figure 3.1: Anatomical (ACSA) and physiological cross-sectional area (PCSA)

However, except for parallel muscle having uniform architecture, (3.1) may lead to inconsistent PCSA estimation, because non-uniformities, such as variable fiber length and pennation angle, occur in the architecture of many other muscles. Furthermore, this algebraic method requires the determination of other parameters, some of which are difficult to estimate accurately. For instance, the commonly used density value of 1.0597g/cm^3 [61], which was derived from unfixed rabbit and canine muscle tissue, may be inaccurate for human skeletal muscles and generally density varies by hydration and fixation time [103]. Muscle volume can be measured directly by water displacement [47], volume reconstruction from MRI scans [35] or indirectly by dividing muscle mass by density [65]. However, water displacement may include internal tendons in volume calculation and MRI has difficulty in identifying specific muscles and capturing narrow areas. In general, architectural parameters are measured by fascicles selectively sampled from the superficial layer of muscle [59, 102]. For an in-depth understanding of architectural parameters and more reliable quantification, Agur et al. [2], Kim et al. [42] and Rosatelli et al. [79] used dissection to collect and digitize fascicles throughout the entire muscle of a human cadaveric specimen. In contrast to these invasive approaches, David et al. [55] proposed a non-invasive method to reliably reconstruct muscle fiber architecture from dense but noisy diffusion tensor images. Based on the digitized fascicle data, Ravichandiran et al. [77, 78] proposed the Fiber Bundle Element (FBE) method to calculate volume and PCSA by representing muscle geometry by a collection of cylinders. Each fascicle is approximated piecewise by a cylinder, the diameter of which is estimated by the distance to the nearest neighboring fascicle. With complete access to volumetric muscle data and geometrical adaptation to its architecture, their method enjoys more reliable estimation of architectural parameters than do other algebraic methods. However, as the diameter of the circular cylinder which they use is always chosen as the distance to the nearest digitized point on a neighboring fascicle, their method may often underestimate the volume of fascicles that are unevenly spaced within muscle. Also, their pointwise calculation for the distance may lead to an inconsistency under certain circumstances. For example, if a fiber point has no collateral neighbors, the estimated thickness of the associated fascicles may be undesirably enlarged because the cross-section is not parallel to the transverse plane.

For robust estimation of PCSA, this study extends the approaches outlined above. PCSA is

estimated by using polygons that are approximated by considering all immediate neighboring fascicles. Also, Cross-sections are forced to be perpendicular to the associated fascicle's orientation. This considerably reduces gaps that may be produced by the FBE method.

Much of the material in this chapter also appears in the publication [51].

3.2 Methods

3.2.1 Data acquisition for muscle specimens

This study is based on data obtained from 24 muscle specimens: 7 specimens for *Extensor carpi radialis bevis (ECRB)*, 7 specimens for *Extensor carpi radialis longus (ECRL)*, 4 specimens for *Pectoralis major (PM)* and 6 specimens for *Supraspinatus (SS)*. Muscle specimens with visible abnormalities, such as muscle atrophy, fat infiltration or surgery, are excluded from the data acquisition. During dissection and digitization, associated skeletons and joints are stabilized in the anatomical position with metal plates and screws. Fascicles are sequentially dissected and digitized from superficial to deep throughout the muscle volume. A MicroScribe G2 digitizer with 0.23 mm accuracy is used to mark trajectories of fascicles with sampled points. The fascicles that are digitized in the same plane from medial to lateral constitute a layer. Digitized fascicles are removed, exposing the next layer about $1-2$ mm deeper. To identify fascicles accurately, a surgical microscope is used throughout dissection and digitization. Ethics approval was obtained from the Research Ethics Board at the University of Toronto (Protocol Reference Number: 17108).

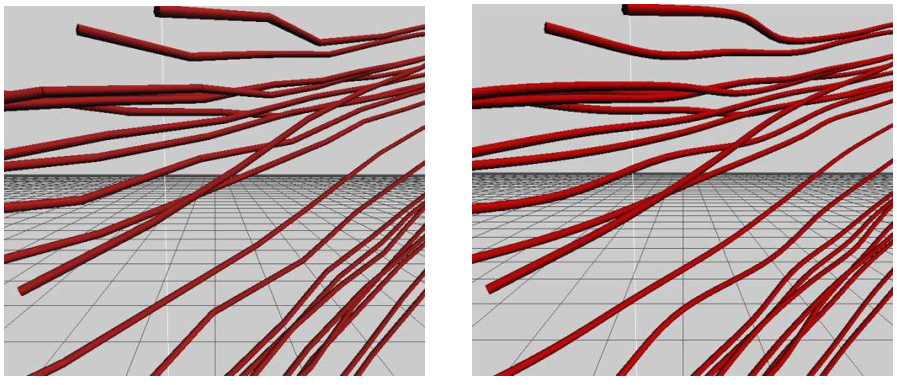

(a) (b)

Figure 3.2: Representation of fascicles. (a) piecewise linear approximation. (b) Catmull-Rom spline interpolation.

3.2.2 Data generation for synthetic muscle

To test and evaluate the proposed method and compare it to the FBE and algebraic methods, both synthetic data and real specimen data are used. To produce the synthetic data, parametric equations are first chosen to represent targeted geometries: cylinder and ellipsoid. Fascicles are then populated and arranged with respect to predefined architectures: parallel for cylinder (Figure 6.3(a)) and unipennate for ellipsoid (Figure 3.7). For each architecture, nonuniform data are also created by varying the interval between fascicles, their length or their pennation angles.

3.2.3 Reparameterisation of digitized fascicles

The original fascicle data are modeled as piecewise lines which simply connect those points (Figure 3.2(a)). However, this modeling may lead to a poor approximation because fascicles are geometrically closer to smooth curves. Thus, a higher-order representation (Figure 3.2(b)) is preferable over the piecewise linear approximation. Ravichandiran et al. [77, 78] used the cubic Bézier spline to model fascicles as smooth curves. However, their curves are not guaranteed to pass through all the original points, resulting in geometric deviation from the original data. Instead, a cubic Catmull-Rom spline is employed to ensure that the interpolating curves do pass through all the original points. Like the cubic Bézier spline, a cubic Catmull-Rom spline is a subset of the class of Hermite cubic splines whose tangents are defined by extra control points and a 0.5 tension parameter [19]. Each line segment in the original fascicle is replaced by a cubic and these cubics are joined to form a smooth curve. Once the entire curve is constructed, fiber points are redistributed or resampled to make the curve representation uniform because the original spacing between adjacent points is often irregular. To this end, an arc-length parameterisation is used. An arc-length function $l(t)$ is defined by

$$l(t) = \int_{t_0}^{t} \left\| \frac{d\mathbf{p}(u)}{du} \right\| du \tag{3.2}$$

where $\mathbf{p}(u) = (x(u), y(u), z(u))$ represents the curve under consideration. As measured fascicles are generally smooth curves, their arc-length can be approximated by chord-length:

$$l_i \approx \| \mathbf{p}_{i+1} - \mathbf{p}_i \| . \tag{3.3}$$

Moreover, this approximation is sufficiently good to give a reparameterized spline curve with nearly equal arc-length between points because fascicles are very unlikely to have high curvature in their trajectories.

Using (3.3), a sequence of parameters c_k for $k = 0, ..., n-1$, can be defined as

$$c_k = \frac{\sum_0^{k-1} \parallel \mathbf{p}_{i+1} - \mathbf{p}_i \parallel}{\sum_0^{n-1} \parallel \mathbf{p}_{i+1} - \mathbf{p}_i \parallel} \tag{3.4}$$

c_k denotes the ratio of the chord length from point $\mathbf{p}_0$ to $\mathbf{p}_k$ over the total length of the entire curve. Using (3.4), an initial curve representation $(c_k, \mathbf{p}_k)$ is obtained at the original points. A new set of parameters is then constructed to be equally spaced by adjusting the interval or sampling rate, producing an interpolated curve $(c'_k, \mathbf{p}'_k)$ (Figure 3.3). For each specimen, data are re-sampled with $0.5 - 1.0\ mm$ intervals, yielding $50 - 90K$ points.

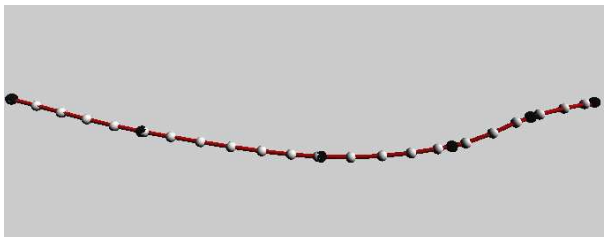

Figure 3.3: Reparameterisation of fascicle: Original points $\mathbf{p}_k$ (black) and the resampled, evenly spaced points $\mathbf{p}'_k$ (white) on the interpolated curve.

3.2.4 Estimation of PCSA

Digitized fascicles provide position and orientation information only for muscle. To calculate PCSA, relevant volumetric information must also be recovered. The FBE method [78] is based on the assumption that the volume of connective tissues inside a muscle is negligibly small. Thus, the thickness of a fascicle can be approximated by the distances to neighboring fascicles. Ravichandiran et al. calculate the radius (i.e., half of the thickness) of a fascicle at every fiber point, $\mathbf{p}$, as

$$r = \min_{\mathbf{q} \in \mathbf{Q}} ||\mathbf{p} - \mathbf{q}||/2 \tag{3.5}$$

where $\mathbf{Q}$ is a set of digitized points on neighboring fascicles. Each fascicle is modeled by a piecewise cylinder, so the average radius, $\overline{r}$, of the fascicle is given by the mean of the radii of all cylindrical segments, and the resulting PCSA is calculated as

$$\text{PCSA} = \sum_{i=1}^{n} \pi \overline{r}_i^2 \cos(\alpha_i), \tag{3.6}$$

where n is the number of fascicles and α_i is the pennation angle of fascicle i. The angle α_i is calculated as the average of the proximal and distal pennation angles of fascicle i. Both angles are measured as the angle between the line of action and tangents at ends of the fascicle (i.e., proximal and distal site) [77, 78]. Recall that the true calculation of PCSA must account for all fascicles occupying the muscle, which exhibits its cross-sections to be densely filled with

fascicles. However, since it is not feasible to capture all fascicles using currently available techniques, acquired data are always represented in various patterns of sample distribution (See Figure 3.4). Thus, if the smallest circle is chosen as the best fit to the spacing between fascicles by (3.5), this spacings may be mishandled (e.g., left as an empty gap), which often underestimates the actual thickness of fascicles. Furthermore, since the radius in (3.5) is based on pointwise distance within a neighborhood, the distance may not always be perpendicular to the orientation of the fascicle, which could overestimate the thickness of fascicles. This problem may be worse at the ends of fascicles (e.g., tendinous attachments) where fascicles often appear in a staggered pattern. These possible over- and under-estimates compromise the reliability of the PCSA computation, depending on the muscle specimen and digitization accuracy.

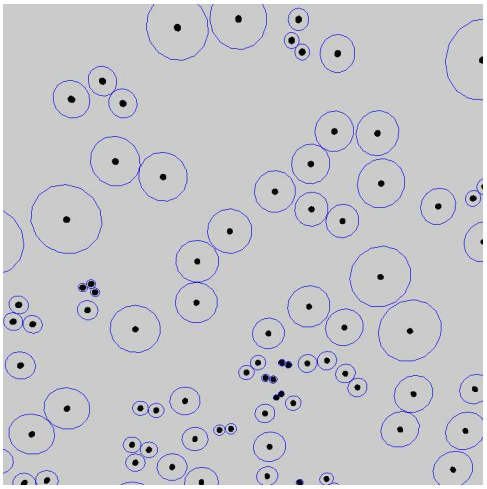

Figure 3.4: The FBE method. smallest circle (blue) is sought at every fiber point, $\mathbf{p}$. These points are on the same transverse plane as the one in Figure 3.5(a).

To improve consistency and reliability, the following extensions are suggested. Instead of the smallest circle, a polygon is used to approximate the cross-sectional area that is formed by a set of points which are equidistant from $\mathbf{p}$ and its neighboring fascicles. Let

$$S(\mathbf{p}) = \{\mathbf{v} | \mathbf{v} = (\mathbf{q} + \mathbf{p})/2, \mathbf{q} \in N(\mathbf{p})\} \tag{3.7}$$

where $N(\mathbf{p})$ is determined by the intersection of the transverse plane at $\mathbf{p}$ and the neighboring fascicles. In contrast to the FBE method that chooses among digitized points, $\mathbf{q}$ in (3.7) can be an arbitrary point on the spline curve representing the fascicle. However, since a cross-section of the fascicle is adjoined by a finite number of neighboring fascicles, only immediate neighbors must be taken into account. Instead of explicitly determining those neighbors, in practice, the Voronoi tessellation is used to directly identify $S(\mathbf{p})$ which consists of vertices and edges equidistant to $\mathbf{p}$ and all its neighbors, $\mathbf{q}$. Thus, the cross-sectional area, A, at $\mathbf{p}$, is simply approximated by the polygon formed by $S(\mathbf{p})$ (i.e., Voronoi region) (Figure 3.5(d)), and the

resulting PCSA is calculated as

$$\text{PCSA} = \sum_{i=1}^{n} \overline{A_i} \cos(\alpha_i) \tag{3.8}$$

where $\overline{A_i}$ is the mean cross-sectional area of fascicle i. Figure 3.5(d) shows that the proposed method always yields a cross-sectional area that is completely filled with polygons, independently of how their centers are arranged. Figure 3.4 illustrates that this is not the case for the FBE method that can be quite sensitive to the data (e.g., sparsity and sampling) whereas the proposed method is much more robust against this deficiency of data.

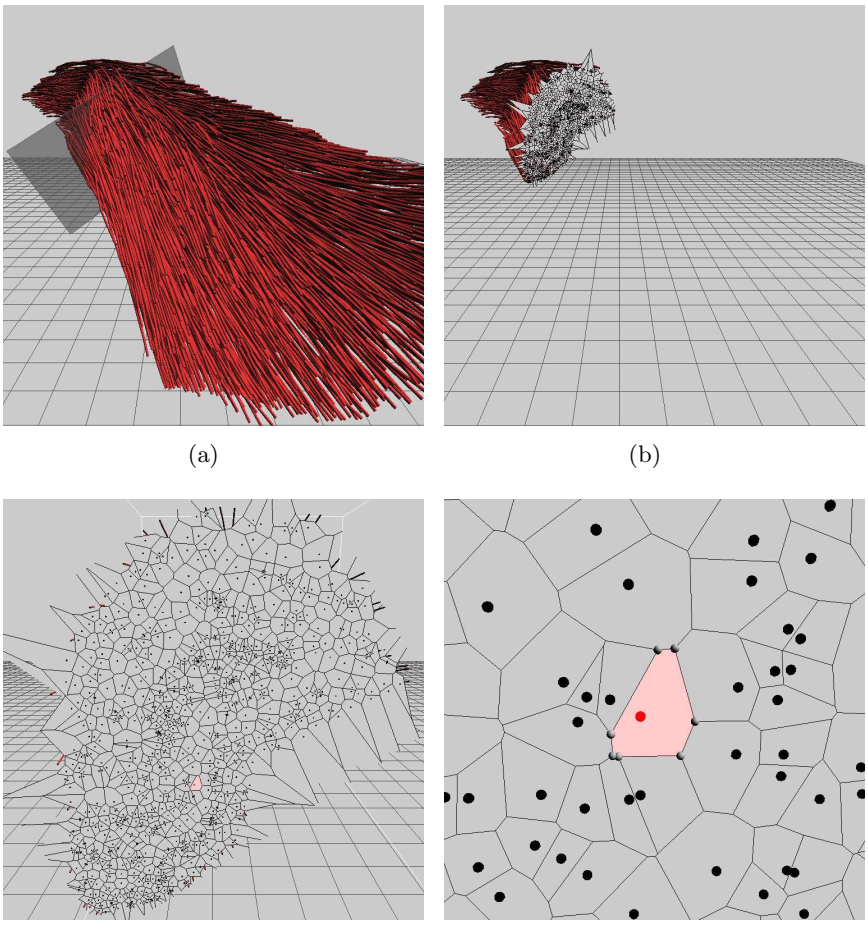

Figure 3.5: Proposed method. (a) a transverse plane defined at $\mathbf{p}_i$ on the chosen fascicle. (b) Voronoi tessellation. (c)(d) close-up view of Voronoi tessellation with a cross-sectional area A at $\mathbf{p}_i$ (red), approximated as a polygon (pink) defined by $S(\mathbf{p}_i)$ (gray).

Generally, fascicles located on superficial layers have some degree of deficiency in that they are surrounded by a few neighboring fascicles only, not completely enclosed by them. This may result in an unbounded Voronoi region, the vertices of which are not completely connected.

This boundary problem is handled by incorporating an angle-based adjustment:

$$A' = A\frac{2\pi}{\sum_i Angle(\mathbf{p}, \mathbf{v}_i, \mathbf{v}_{i+1})} \tag{3.9}$$

where $Angle(\mathbf{v}_0, \mathbf{v}_1, \mathbf{v}_2)$ is the angle formed by $(\mathbf{v}_0 - \mathbf{v}_1)$ and $(\mathbf{v}_0 - \mathbf{v}_2)$.

3.3 Results

3.3.1 Synthetic muscle data

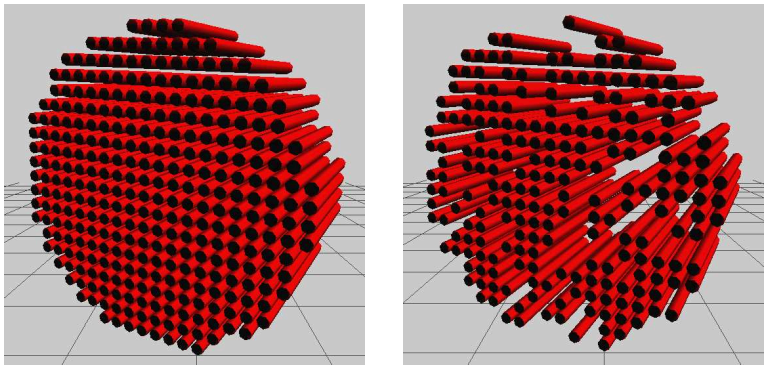

(a) (b)

Figure 3.6: Synthetic parallel muscles. Fascicles are created within a cylinder having radius and length of 5 cm and pennation angle of 0. (a) uniform muscle. (b) nonuniform muscle (intervals between fascicles are variable).

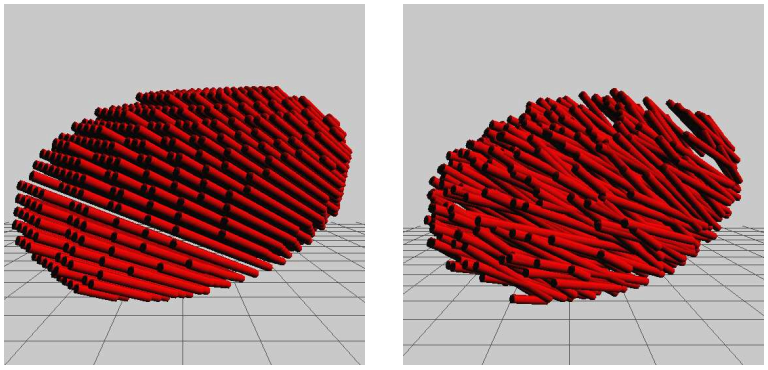

(a) (b)

Figure 3.7: Synthetic unipennate muscles. Fascicles are created within an ellipsoid, having axes of length 5, 5 and 10 cm. (a) uniform muscle (only fascicle length is variable) (b) nonuniform muscle (fascicle length, pennation angle and interval between fascicles are variable).

As the exact geometry is known for each problem, the algebraic method (3.1) gives the exact PCSA for the problem, by assuming that this algebraic method accounts for all fascicles distributed in a uniform and continuous form. On the other hand, the synthetic data only represent sampled fascicles. Furthermore, some amount of non-uniformity is introduced to simulate the deficiency of data acquisition. This exact PCSA value is used to compute the error associated with either the proposed method or the FBE method applied to those synthetic data. The PCSA results for these three methods and the relative errors for the proposed method and the FBE method are presented in Table 3.1. The results show that the proposed method performs much more reliably than the FBE method. Note that the FBE method underestimates PCSA

Muscle	Algebraic Method	Proposed Method	FBE Method
Parallel[1]	78.5	78.7 (+0.3)	61.7(−21.4)
Parallel[2]	78.5	79.1 (+0.8)	42.2(−46.2)
Unipennate[1]	97.3	101.8(+4.6)	78.8(−18.9)
Unipennate[2]	94.3	102.4(+8.7)	32.6(−65.3)

Table 3.1: Comparative results for PCSA (cm^2) using the algebraic method, the proposed method and the FBE method. Superscripts 1 and 2 indicate uniform and nonuniform representation, respectively. Percentage of relative errors are given in parenthesis.

by nearly 20% even in uniform muscles. Because spacings between fascicles are equal vertically and horizontally but not diagonally, there are substantial gaps between diagonal neighbors. The larger the variance of those spacings is, the more the gaps between fascicles are not accounted for in the FBE method. This results in the FBE method's vulnerability to nonuniformity of data that often exists in specimen data or can be induced by digitization error. On the other hand, the proposed method considers the entire proximities around fascicles. Hence, it produces more robust PCSA estimates with less sensitivity to data. The results computed by the proposed method are always slightly larger than the results for the algebraic method. This is caused by how the boundary is treated by the proposed method. As cross-sectional areas of boundary fascicles are adjusted by extrapolation in this method, outer areas located beyond the predefined boundary also are added into the calculation. This adjustment can be larger in nonuniform muscle than in uniform muscle.

3.3.2 Digitized specimen data

The new PCSA and volume estimation for specimen data are given in Table 3.2, and a comparison with the FBE method is presented in Table 3.3. The results clearly show that PCSA and volume vary by specimen and muscle. Similar to the results for synthetic data, the proposed method yields larger PCSA estimation than does the FBE method. The two methods differ by $45-50\%$ for *ECRB*, *ECRL* and *PM*, and $20-35\%$ for *SS* in specimen to specimen comparison. This may be because *SS* is more uniform than other muscles in terms of fascicle arrangement or cross-sectional area. Note that the FBE results by the proposed method are smaller than the original results [78]. That may be explained by the difference of resampling fascicle data. In the proposed method, fiber points are resampled very densely and equally spaced. That reduces over-estimation for fascicle thickness that point-wise calculation of the FBE method could produce (as discussed in Section 3.2.4).

Muscle	n	PCSA	Volume^c	Volume^t
ECRB	128	4.18	21.33	20.33
	93	2.09	12.01	12.23
	117	2.65	17.32	16.36
	106	2.84	18.72	18.24
	106	2.43	14.45	12.18
	178	2.11	8.81	8.47
	126	3.03	16.83	16.22
ECRL	116	4.14	28.37	26.49
	87	1.63	13.37	13.68
	62	1.65	15.66	15.23
	74	2.74	27.92	24.1
	76	1.59	15.54	14.74
	105	1.9	11.86	11.44
	92	2.02	17.67	16.66
PM	634	14.87	277.1	246.78
	679	12.1	224.4	171.36
	767	12.32	206.7	169.69
	873	10.41	188.7	140.3
SS	1750	6.16	45.7	38.23
	1081	5.07	33.7	25.35
	1684	6.31	39.18	28.68
	1061	7.68	38.38	31.71
	1294	7.16	52.26	42.91
	1556	9.16	64.71	53.7

Table 3.2: PCSA (cm^2) and volume (cm^3) estimation for specimen data by the proposed method; n is the number of digitized fascicles.

Muscle	Proposed Method	FBE
ECRB	2.76 ± 0.72	1.26 ± 1.37
ECRL	2.24 ± 0.93	1.13 ± 0.29
PM	12.43 ± 1.84	7.43 ± 0.69
SS	6.92 ± 1.42	4.31 ± 1.49

Table 3.3: Comparative results for PCSA (cm^2) between the proposed method and the FBE method. The number before the $\pm$ is the mean PCSA for all specimens of that muscle type in Table 3.2, while the number after the $\pm$ is the associated standard deviation.

3.4 Discussion

Human cadaveric muscle specimen data provide the potential for an in-depth understanding of human skeletal muscle and accurate parameter estimation. However, most muscles have highly non-uniform architecture, in that their fascicles vary in orientation, thickness and cross-section. Thus, determining the associated parameters, specifically, PCSA, is not straightforward. Furthermore, any measurement error may induce more non-uniformity. To maximize utilization of the cadaveric data, this non-uniformity needs to be dealt with appropriately. The commonly used algebraic method (3.1) only uses average values of associated parameters, such as volume, density and fascicle length, which does not account for architectural complexity well. By using this method, it is hard to investigate region-specific variation of architecture that is existent in most muscles. Furthermore, those parameters are not all easy to determine accurately. For instance, MRI provides direct volume calculation but it has some limitations: difficulty in differentiating specific muscle from others and inaccuracy in narrow areas. The FBE method only uses the coordinate of digitized fascicles to directly calculate PCSA without the need for any other parameters. However, its performance varies with the application. While it works well for uniform data, it shows inconsistency for non-uniform data. It is often observed that its overall performance is very sensitive to the quality of data (e.g., poorly digitized fascicles), which in turn necessitates additional efforts and time in data acquisition. To effectively deal with those problems, therefore, this study proposes an adaptive geometric approach. By carefully considering the local proximity around each fascicle, the proposed approach finds a piecewise cylinder to completely fill the non-uniform spacing between fascicles. A collection of cylinders is then used to determine overall architectural parameters. This approach shows consistent estimation over various types of muscle without any modeling adjustment. It also shows robustness against some deficiency of data, such as noise and under-sampling, which is often inherent in current data acquisition procedure.

Although the proposed approach exhibits improved parameter estimation capability compared to earlier approaches, there are some problems to overcome. Firstly, in the PCSA estimation, no connective tissues or other tissues (e.g., blood vessels) are considered. Even though they occupy volume to some extent between fascicles, all partitioned areas are simply included in the PCSA. Thus, the PCSA calculated by the proposed method may be slightly larger than the actual PCSA. This may be more problematic in understanding pathological muscle having fat infiltration, which could over-estimate its functional capacity. It would be also potential studies to investigate structural tissue components in the cross-section of muscle specimen, and then compare them with the reconstruction based on the Voronoi tessellation. Secondly, parameterisation of cross-sections needs to be improved. These cross-sections are individually and locally approximated by parametric ellipses. Even though the thickness of a fascicle changes smoothly, the least squares based estimation of serial cross-sections may vary abruptly depending on the availability of their neighbors. Incorporating the correlation between adjacent cross-sections or

global constraints may produce more reliable and consistent parameterisation than the localized method does. Thirdly, only four sets of synthetic data are used to validate the proposed method. For a more extensive validation study, it is needed to increase the sample size of data (e.g., more random data generated for each architecture) or introduce other variations, such as variable spline curves rather than straight lines. However, to conduct rigorous validation, real muscle data must be used. To this end, two problems need to be addressed; how to approximate *in vivo* architectural parameters by using the cadaveric modeling approach and how to relate the architecture-based PCSA estimation with some phenomenological approach (e.g., maximum force or torque measure). Fourthly, even though the proposed method is not very dependent on modeling parameters (e.g., arc-length and boundary condition), it would be desirable to demonstrate this in a more analytical way. For instance, a fascicle trajectory can be digitized with various sampling rates and intervals, and then compared against its reconstructed model based on the spline method. Finally, there is another important aspect of the problem that is currently handled in an ad hoc way. To extract muscle geometry, level sets of all fascicles must be properly interpolated with acceptable overlaps. As the overlap increases, the resulting muscle surface becomes smoother but shrinks. Otherwise, the surface breaks into disjoint fascicles. Thus, accurate reconstruction of muscle geometry needs the determination of appropriate overlaps, which are left as a topic for future work.

Chapter 4

Estimation of pennation angle for skeletal muscle

4.1 Introduction

The physiological and mechanical functions of muscle are characterized by associated architectural parameters, such as thickness, fascicle length, pennation angle and physiological cross-sectional area [111]. Specifically, pennation angle (PA) is an important determinant of the contribution that muscle fascicles make to the force acting along the line of action. PA is defined as the angle between the orientation of a fascicle and the attached tendon axis (i.e., the line of action) (see Figure 4.1(a)). For each fascicle i, its PA is simply calculated as

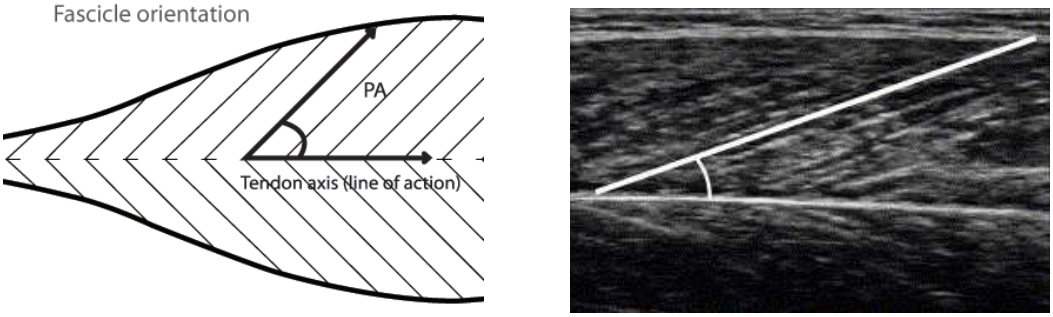

(a) (b)

Figure 4.1: Pennation angle. (a) Schematic of definition. (b) Measurement on an ultrasonographic image.

$$\mathrm{PA}^i = \cos^{-1}(\text{line of action} \cdot \text{fascicle orientation}^i). \tag{4.1}$$

As the muscle fascicle force, $\mathbf{f}_m^i$, is in the direction of the fascicle orientation and the tendon force, $\mathbf{f}_t$, is in the direction of the line of action, their functional relation is expressed as

$$\mathbf{f}_t = \sum_i \mathbf{f}_m^i \cos(\mathrm{PA}^i). \tag{4.2}$$

Since fascicles have variable length and arrangement within a muscle, the associated PA differs from fascicle to fascicle [27, 98, 59]. For its quantification, two-dimensional (2D) ultrasonography is widely used in many clinical and biomechanical studies, because it is non-invasive, portable and applicable to dynamic measurements (e.g., muscle contraction). However, since a muscle is only assessed by 2D images, the accuracy of the measurement (up to 23% error) relies on the alignment of the imaging plane (or ultrasound probe) [11, 76]. Since fascicles form complex and variable structures within a muscle, it is challenging to find the correct imaging plane (namely, true fascicle plane) that provides a more precise assessment of the entire three-dimensional (3D) architecture. Thus, in practice, the optimal plane is determined by satisfying the following criteria: maximum visibility of fascicles and perpendicular to the skin or deep aponeurosis. However, it is evident that individual 2D images may be subject to a limited assessment of volumetric geometry. Limited visibility and image resolution also impose further constraints on conducting detailed investigations.

In contrast to ultrasonographic assessments, the use of cadaveric specimens allow direct measurement of PA. Lieber and Friden [59], Murray et al. [65] and Ward et al. [102] collected a small number of fascicles from specimen surfaces and measured PA using a hand-held goniometer or protractor. Although their direct measurements would in principle be more accurate than ultrasonographic assessments, any internal variation was not accounted for in their quantifications. On the other hand, Agur et al. [2], Kim et al. [42], Rosatelli et al. [79], Ravichandiran et al. [77] and Lee et al. [51] conducted assessment of PA based on volumetric fascicle data that were collected throughout the muscle using dissection and digitization procedures. Those studies assumed that the line of action was aligned to the longitudinal axis of muscle [100, 45] that was approximated as an average of orientation of all fascicles. PA was then calculated as the relative angle between this axis and the fascicle orientation. However, this approximation may still fail if it is inconsistent with the underlying muscle architecture. For example, in pennate muscles, this muscle axis may not coincide with the tendon axis, because fascicles run parallel to one another, but they are variably oblique to the attached tendon axis (see Figure 4.2). Therefore, for consistent quantification, PA must be estimated with respect to the tendon axis. Digitizing tendons may be an immediate solution for this problem, but certain types of tendons (e.g., intramuscular or aponeurotic tendon) may have irregular shapes and arrangements that make reconstruction challenging.

The purpose of this study is to provide insight into the correspondence between underlying 3D

architecture and 2D assessment. To this end, a 3D method was developed to directly quantify PA based on 3D architectural data [51]. Those data were then assessed two-dimensionally by simulating ultrasound imaging. Using anatomically defined reference frames, region specific variation of PA within a muscle was investigated.

Figure 4.2: Problematic line of action estimation. Average orientation of fascicles is apparently oblique to the patellar tendon, the axis of which is directed horizontally in the given configuration.

Much of the material in this chapter also appears in the publication [50].

4.2 Methods

This study is based on cadaveric specimen data obtained through serial dissection and digitization procedures. Fascicles were collected and geometrically reconstructed to represent the muscle architecture. Based on the reconstructed architecture, the geometric arrangement of fascicle attachments was used to estimate PA. A reference coordinate frame was determined to evaluate region-specific variation of PA and also used to initialize the imaging plane for simulated ultrasound scans.

4.2.1 Data acquisition for muscle specimens

The experimental data are acquired from a variety of muscles including two lower extremity muscles — abductor hallucis (ABH) and vastus medialis (VM) — and sixteen upper extremity muscles — anconeus (ANC), abductor pollicis longus (APL), brachialis (BR), extensor carpi radialis bevis (ECRB), extensor carpi radialis longus (ECRL), extensor carpi ulnaris (ECU), extensor digitorum (ED), extensor digitorum (EDM), extensor indicis (EI), extensor pollicis brevis (EPB), extensor pollicis longus (EPL), flexor carpi ulnaris (FCU), pectoralis major (PM), pronator teres (PT), pronator quadratus (PQ) and supraspinatus (SS). Muscle specimens with

visible abnormalities, such as muscle atrophy, fat infiltration or surgery, were excluded from the data acquisition. During dissection and digitization, associated joints were stabilized into anatomical position with metal plates and screws. Fascicles were sequentially dissected and digitized from superficial to deep throughout the muscle volume. A MicroScribe G2 digitizer with 0.23 mm accuracy was used to mark trajectories of fascicles with sampled points. Digitized fascicles were removed, exposing the underlying fascicles about $1-2$ mm deeper. To identify fascicles accurately, a surgical microscope was used throughout the dissection and digitization process. [1]

4.2.2 Orientation of fascicles

Using the digitized points, each fascicle is first approximated by a smooth piecewise cubic spline, $\mathbf{p}(u) = (x(u), y(u), z(u))$, where $u \in [0, 1]$. The orientation of a fascicle is represented by a series of tangent vectors, $\mathbf{p}'(u) = (x'(u), y'(u), z'(u))$, along the curves (See Figure 4.3).

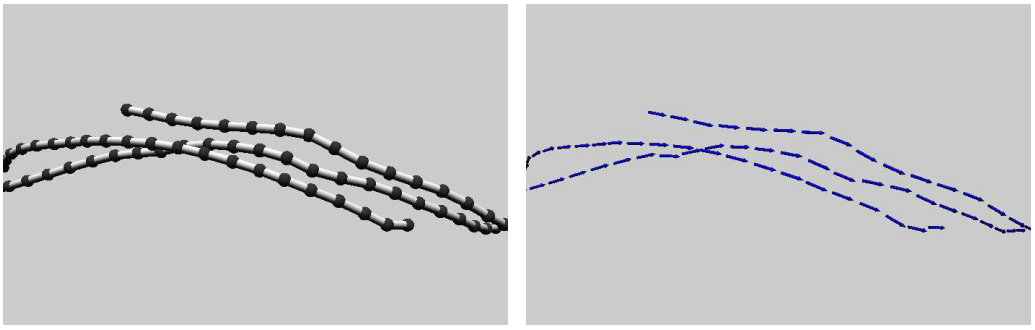

(a) (b)

Figure 4.3: Representation of fascicles. (a) Spline curves and resampled points, $\mathbf{p}$. (b) Tangents, $\mathbf{p}'$, evaluated along the curves.

Using an arc-length parameterization, fascicle points are redistributed (i.e., resampled) to make the curve representation uniform [51]. As reconstructed spline curves are clamped at their ends (i.e., tendinous attachments), tangent vectors at these points must be approximated from neighboring points, using formulas such as $\mathbf{t}(0) = \mathbf{p}'(0) \approx (\mathbf{p}(u_1) - \mathbf{p}(u_0))/(u_1 - u_0)$ and $\mathbf{t}(1) = \mathbf{p}'(1) \approx (\mathbf{p}(u_n) - \mathbf{p}(u_{n-1}))/(u_n - u_{n-1})$. To determine proximal and distal orientation, previous studies [77, 51] simply chose tangent vectors evaluated at the end points (i.e., approximations to $\mathbf{p}'(0)$ and $\mathbf{p}'(1)$). However, the positions of tendinous attachments may be slightly perturbed due to errors that may occur in the dissection and digitization procedure. This may affect the angular measurement in (4.1). For more reliable quantification, the proposed method takes an average of the tangent fields evaluated over a local area close to these attachments. More specifically, for each fascicle i, the averaged tangent vectors for proximal, $\overline{\mathbf{t}_p^i}$, and distal, $\overline{\mathbf{t}_d^i}$,

[1] Ethics approval was obtained from the Research Ethics Board at the University of Toronto (Protocol Reference Number: 27210).

orientations are calculated as

$$\overline{\mathbf{t}_p^i} = \frac{1}{n_p}\sum_{u=0}^{u_p}\mathbf{t}^i(u) \tag{4.3}$$

$$\overline{\mathbf{t}_d^i} = \frac{1}{n_d}\sum_{u=u_d}^{1}\mathbf{t}^i(u) \tag{4.4}$$

where $\mathbf{t}^i(u)$ is the tangent vector for fascicle i defined at the point $\mathbf{p}(u)$, n_p and n_d are the number of points in the local proximal and distal regions, respectively, and $u \in [0, ..., u_p, ..., u_d, ..., 1]$. In practice, $0.15 - 0.2$ is used for u_p and $0.8 - 0.85$ is used for u_d, whence approximately $15 - 20\%$ of the entire fascicle length is included in each of the proximal and distal regions.

4.2.3 Line of action

The line of action of a muscle can be approximated by the long axis of the internal tendon onto which the fascicles attach. For non-pennate muscles, such as fusiform and parallel muscles, the average direction of collective forces exerted by all fascicles is parallel, or nearly parallel, to the axis of the attached tendon. Thus, the line of action can be approximated as [77, 51]

$$\begin{aligned}\text{line of action}_p &= \frac{1}{n}\sum_{i=1}^{n}\overline{\mathbf{t}_p^i}\\ \text{line of action}_d &= \frac{1}{n}\sum_{i=1}^{n}\overline{\mathbf{t}_d^i}\end{aligned} \tag{4.5}$$

where n is the number of fascicles. This approach, based on Equation (4.5), is conceptually similar to the method described in [45]: the estimated centre line corresponds to an average direction of all fascicles (see Figure 4.4). However, equation (4.5) may be inappropriate for pennate muscles, because fascicles are often oblique, rather than parallel, to attached tendons. Thus, the averaged direction of fascicles may produce a poor estimate of the line of action (see Figure 4.2). Digitized tendons or aponeuroses could be used to determine the line of action, but, compared to fascicle data, they are often observed to be irregular and non-homogeneous in terms of arrangement or shape. Thus, the fascicle data may be more straightforward and simpler to deal with computationally.

From the specimen data, it is observed that the geometric arrangement of fascicle attachments reveals the directionality of the tendons. For instance, in pennate muscles, tendinous attachments are linearly arranged, whereas in non-pennate muscle, they are arranged in more diverse patterns. To be more specific, for pennate muscles, the distribution of the attachment points is approximately represented as a long and thin ellipsoid, the principal axis of which roughly matches the tendon axis. The least square regression method can be used to find this axis:

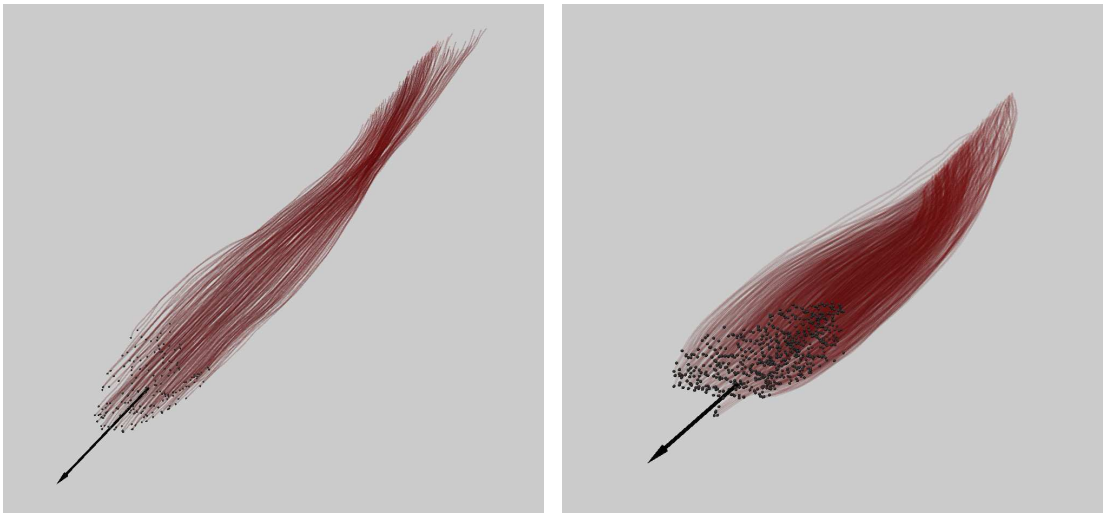

(a) (b)

Figure 4.4: Estimated line of action (black arrow) and distal attachments (black dots) of fascicles (red) for fusiform muscle. (a) Brachioradialis. (b) Extensor carpi radialis longus.

$$\min_{\beta_1\,\beta_2} \sum_i \|S(\mathbf{p}_i) - \boldsymbol{\beta}_1 t_i - \beta_2\|^2 \tag{4.6}$$

where $S(\mathbf{p})$ denotes the attachment points and $\boldsymbol{\beta}_1 t + \beta_2$ is the linear regression model to fit. The vector $\boldsymbol{\beta}_1$ is the estimated principal axis for the line of action (see Figure 4.5).

4.2.4 Pennate and non-pennate muscles

Depending on pennation, the line of action in (4.1) is determined by using either (4.5) or (4.6). For reliable quantification of PA, the method for determining the line of action must be chosen consistently. To this end, recall that attachments of fascicles are arranged linearly in pennate muscle, but are more complex in non-pennate muscle. To utilize this characteristic in determining the type of muscle, the quality of the fit in (4.6) is evaluated by considering

$$r^2 = 1 - \frac{\sum_{i=1}^n \|S(\mathbf{p}_i) - \boldsymbol{\beta}_1 t_i - \beta_2\|^2}{\sum_{i=1}^n \|S(\mathbf{p}_i) - \overline{S(\mathbf{p})}\|^2} \tag{4.7}$$

where $\overline{S(\mathbf{p})} = \frac{1}{n}\sum_{i=1}^n S(\mathbf{p}_i)$ and n is the number of attachment points. Here, $r^2 = 1.0$ indicates a perfect fit of the regression model, while $r^2 = 0.0$ is associated with the poorest fit. Because of the linearity of their attachment arrangement, pennate muscles have high values of r^2, whereas non-pennate muscles have lower values of r^2. Based on this difference, a threshold for the r^2 value can be chosen to classify muscles as either pennate or non-pennate. However, some pennate muscles, which are directly attached to bones without any external tendons, may need to be classified differently. In such cases, the line of action is approximated as the average orientation of fascicles using (4.5) instead (see Figure 4.6). Attachment types (i.e., tendinous

(a) (b)

Figure 4.5: Estimated line of action (black arrow) and distal attachments (black dots) of fascicles (red) for pennate muscle. (a) Supraspinatus. (b) Vastus medialis.

or bony attachment) can be determined during the dissection and digitization process.

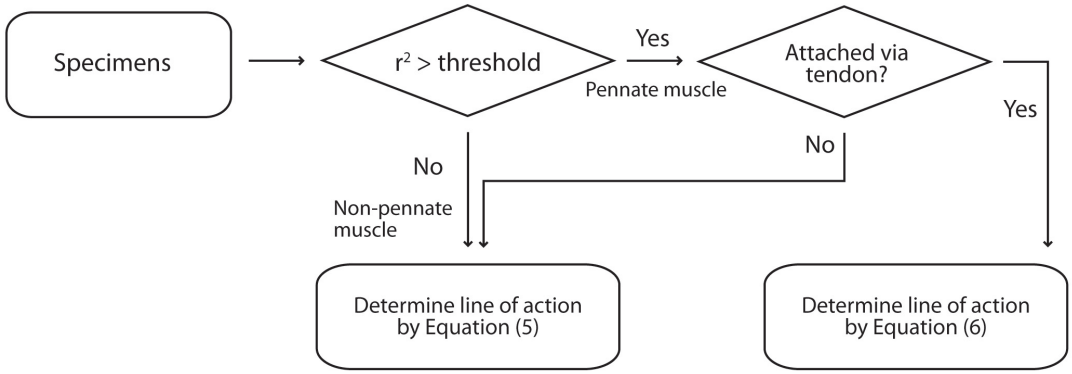

Figure 4.6: Flow chart for the proposed method to determine the line of action.

4.2.5 Anatomical reference frame

A reference coordinate frame is determined for the further analysis of the correlation between the PA distribution and the fascicles' anatomical positions within the muscle volume. To this end, a three-dimensional Cartesian coordinate system is formed by the three orthogonal axes that originate from the geometric centre of the muscle and correspond to the standard anatomical directions: proximo-distal, superficial-deep and latero-medial (or anterior-posterior) (see Figure 4.7).

The estimated line of action (described in Section 4.2.3) is used to represent the proximo-distal

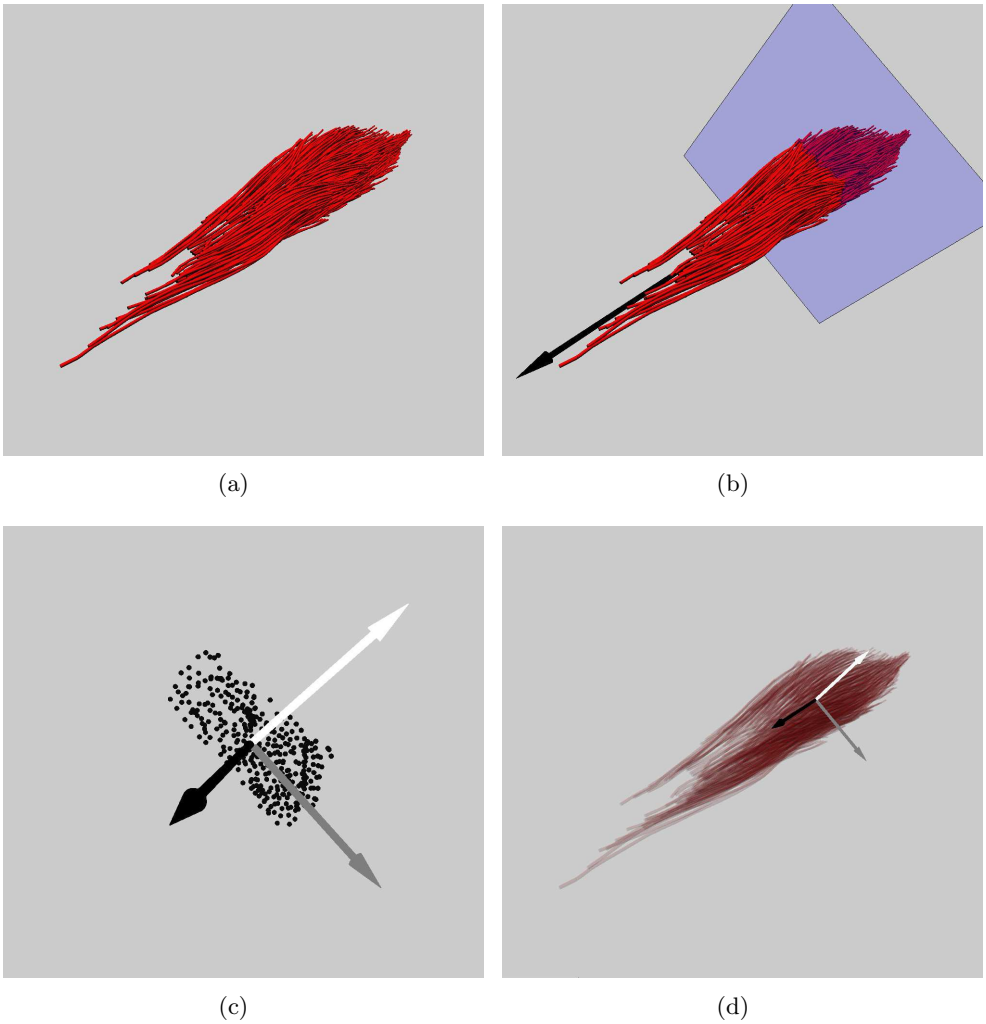

Figure 4.7: Anatomical reference frame. (a) Fascicles of extensor digitorum muscle. (b) Illustration of the line of action, shown as the black arrow in the distal region, and the corresponding cross-section, π_C, shown as the purple plane. (c) Intersection points of π_C with the fascicles and the estimated anatomical directions, superficial-deep (white arrow) and the medial-lateral (gray arrow). (d) Reference coordinate frame shown with the fascicles.

axis. Subsequently, the cross-section, π_C, is defined as the plane that is transverse to the proximo-distal axis and located at the origin of the coordinate frame (see Figure 4.7(b)). The intersection of π_C and the fascicles yields a two-dimensional point-set, $\{S(\mathbf{p}_c)\}$. Many superficial muscles have elliptical cross-sections, the longer and shorter axes of which approximately correspond to the latero-medial and the superficial-deep axes, respectively (See Figure 4.7(c)). These axes can be effectively estimated by a principal component analysis (PCA): the eigenvector associated with the larger eigenvalue approximates the major axis of the ellipse whereas the eigenvector associated with the smaller eigenvalue represents its minor axis. In the case of muscles that have circular cross-sections (e.g., ECRL), the axes determination may be inconsistent, as those eigenvectors may not coincide with the corresponding anatomical axes. Consequently, manual adjustment may be required. With regard to the proximo-distal axis, all distal attachments of the fascicles are projected onto this axis and their relative positions are used to evaluate correlation. Regarding the latero-medial and superficial-deep axes, the geometric deviations of all fascicles from the centre of the muscle are calculated and then assessed in relation to the axes.

4.2.6 Simulated ultrasound assessment

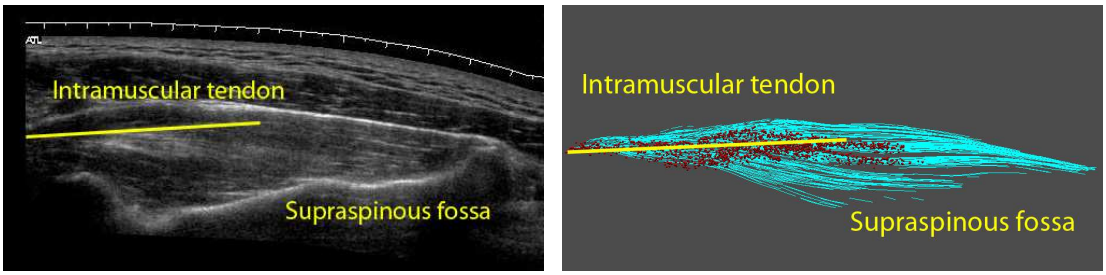

(a) (b)

Figure 4.8: Mid-longitudinal images of Supraspinatus: (a) living subject by ultrasound. (b) cadaveric specimen (digitized fascicle data) by simulated ultrasound.

Two-dimensional (2D) ultrasound assessment is simulated by projecting fascicles onto the imaging plane, which is determined by the linear combination of two reference axes (see Figure 4.8). The longitudinal plane is defined by either the proximo-distal and the latero-medial axes or the proximo-distal and superficial-deep axes. The transverse plane is defined by the latero-medial and superficial-deep axes. Translating and rotating these planes imitates the alignment control of the ultrasound probe. To create a 2D image, viewable fascicles are identified by evaluating their proximity to the imaging plane and then they are projected onto that plane. To be comparable to an ultrasound scan, the simulated imaging plane is initially positioned at the geometric centre of the muscle and aligned to the mid-longitudinal plane. Then, the position and orientation of the plane are adjusted by up to ± 10 mm and $\pm 15^\circ$, respectively, to maximize the number of viewable fascicles. PA is then calculated based on the projected fascicle image

using the projected 2D fascicles and the line of action. In some cases, only the middle portion of a fascicle is visible in the projected image. In such cases, it may be inaccurate to estimate the fascicle's tangent vector at the attachments points by extrapolation. Thus, in practice, when calculating PA, the proposed method uses only the projected fascicles that have a viewable portion that includes at least $15 - 20\%$ of the proximal and distal regions (similar to Section 4.2.2). Since the focus of this study is specifically to understand the correspondence between 2D imaging data and 3D volumetric data, the simulation approach is simplified by excluding any other factors, such as tissue deformation, anisotropic image features and volume rendering, that are often discussed in realtime ultrasound simulation studies.

4.3 Results

The PA estimation results for 18 muscles, using both 2D and 3D methods, are given in Table 4.1. The 2D method is based on the simulated ultrasound imaging method described in Section 4.2.6. The proposed 3D method is described in Sections 4.2.1–4.2.5. The PA estimation results are also presented graphically in Figures 4.9, 4.10 and 4.11.

Muscle	N (N_{2D})	Pattern	r^2	PA_{3D}	PA_{2D}
ABH	396 (136)	pennate	0.98	18.9 ± 8.9 (0.7 – 52.1)	13.8 ± 9.6 (0.4 – 46.5)
ANC	728 (64)	non-pennate	0.96	16.8 ± 12.3 (0.5 – 78.8)	10.2 ± 6.3 (0.9 – 29.5)
APL	620 (184)	pennate	0.98	13.1 ± 5.6 (0.6 – 40.2)	11.3 ± 7.7 (0.1 – 37.0)
BR	182 (24)	non-pennate	0.67	3.1 ± 2.2 (0.1 – 10.8)	4.3 ± 3.7 (0.1 – 15.6)
ECRB	630 (306)	pennate	0.93	14.2 ± 4.9 (1.8 – 35.1)	8.2 ± 6.1 (2.5 – 54.3)
ECRL	629 (84)	non-pennate	0.82	11.9 ± 5.1 (1.0 – 33.4)	12.8 ± 7.8 (0.2 – 31.6)
ECU	449 (126)	pennate	0.99	6.4 ± 2.9 (0.4 – 19.0)	5.5 ± 4.0 (0.1 – 17.7)
ED	460 (89)	pennate	0.97	9.3 ± 3.5 (0.3 – 22.1)	9.2 ± 5.9 (0.4 – 29.8)
EDM	158 (82)	pennate	0.99	5.6 ± 2.5 (0.4 – 10.7)	4.8 ± 3.5 (0.0 – 22.4)
EI	176 (89)	pennate	0.98	9.6 ± 4.4 (0.6 – 21.9)	7.6 ± 6.2 (0.2 – 27.1)
EPB	155 (63)	pennate	0.96	22.9 ± 8.8 (9.5 – 49.9)	21.5 ± 17.9 (0.6 – 85.0)
EPL	201 (65)	pennate	0.99	6.4 ± 3.0 (0.8 – 15.8)	5.2 ± 3.5 (0.2 – 17.8)
FCU	1047 (442)	pennate	0.99	15.4 ± 6.9 (0.5 – 37.6)	10.1 ± 7.6 (0.1 – 42.2)
PM	792 (64)	non-pennate	0.78	13.6 ± 10.2 (0.2 – 41.3)	7.2 ± 5.1 (0.2 – 20.9)
PQ	910 (78)	non-pennate	0.69	19.6 ± 10.3 (2.9 – 59.6)	12.3 ± 13.7 (0.1 – 76.8)
PT	1218 (313)	pennate	0.98	15.8 ± 7.0 (0.3 – 43.1)	12.2 ± 8.3 (0.1 – 44.1)
SS	1750 (723)	pennate	0.92	16.5 ± 9.5 (0.4 – 43.9)	13.1 ± 3.6 (0.9 – 43.2)
VM	703 (370)	pennate	0.97	34.5 ± 15.7 (2.6 – 70.0)	30.4 ± 13.6 (1.6 – 83.2)

Table 4.1: Estimation of PA at distal attachments. N is the total number of digitized fascicles. N_{2D} is the number of projected fascicles in the imaging plane. PA_{3D} and PA_{2D} are the estimated PA using the 3D method and the 2D method, respectively. The value of PA (in degrees) is given as 'the mean $\pm$ the standard deviation (min-max)'.

4.3.1 Pennate and non-pennate muscles

The linearity of the geometric arrangement of the distal attachments is evaluated using (4.7). All pennate (i.e., unipennate and bipennate) muscles have r^2 values ranging from 0.92 to 0.99, indicating a highly linear arrangement of the attachment. Other muscles having lower r^2 val-

ues are classified as non-pennate muscles (i.e., fusiform and convergent). A value of 0.9 was selected as the dividing threshold between pennate and non-pennate muscle. This agrees with the general classification suggested in gross anatomy. However, there exist exceptional cases that may need to be dealt with differently, such as ANC. Although the distal attachment for ANC muscle exhibits a strong linear arrangement ($r^2 = 0.962$), the estimated axis may not represent its tendinous axis, since the ANC muscle is attached directly to the ulna without an external tendon. Consequently, this estimated axis may coincide with the longitudinal axis of the bone. In such cases for which a muscle is attached directly to a bone, the line of action is approximated as an average orientation of fascicles using (4.5) instead of (4.6).

Fan-shaped muscles (ANC, PM and PQ) have substantial variation in their PA, whereas fusiform or parallel muscles (BR, ECRL) have a relatively small range of PA values. In fan-shaped muscles, fascicles are spread over a broad area and converge into a narrow attachment site. Their PA varies considerably from the fascicles located farthest from the central axis (78.81° in ANC) to ones located closest to this axis (0.48° in ANC). In pennate muscles, fascicles are inserted more obliquely at the distal end of the tendon, whereas they are nearly parallel to the axis of the tendon at the proximal end.

4.3.2 Region-specific variation of PA

To effectively visualize local variation of PA throughout a muscle, its distribution is normalized and mapped onto a color gradient ranging from red (PA_{min}) to blue (PA_{max}). The correlation between region and PA is mathematically quantified by associating the geometric location of the fascicle with the three anatomical axes as described in Section 4.2.5. With respect to these axes, the distribution of PA is depicted in plots and the observed correlations are expressed using fitted polynomial functions. The results demonstrate that the correlation patterns may differ from muscle to muscle and furthermore that one axis may have a stronger correlation than another. In relation to the anatomical axes, PA changes either monotonically (e.g., decreasing or increasing) or non-monotonically (e.g., decreasing and then increasing). In most cases, these patterns are well-fitted by either a linear or a quadratic function.

Among the muscles investigated in this study, the pennate muscles are commonly observed to have increasing PA in the proximo-distal direction. This correlation is stronger for unipennate muscles (e.g., EPB and VM) than for other types of muscles, because these unipennate muscles have a relatively simple architectural pattern in that the fascicles are attached to only one side of the tendon (see Figure 4.9). The correlation with the proximo-distal direction rarely occurs for non-pennate muscles (e.g., BR and ECRL). Instead, these muscles are observed to have a changing pattern of PA in the transverse direction, such as lateral to medial or superficial to deep (see Figure 4.10). Similarly, in bipennate muscles, PA distribution may be characterized

with respect to the latero-medial direction, because, in those muscles, the geometric deviation of fascicles from the line of action (i.e., extramuscular tendon for non-pennate muscles and intramuscular tendon for bipennate muscles) can be quantified in the transverse direction, which is proportional to their PA. Fascicle arrangement may be nearly symmetric (e.g., ECRB) or asymmetric (e.g., APL) in relation to the tendon, which leads to either non-monotonic or monotonic PA distribution (see Figure 4.11).

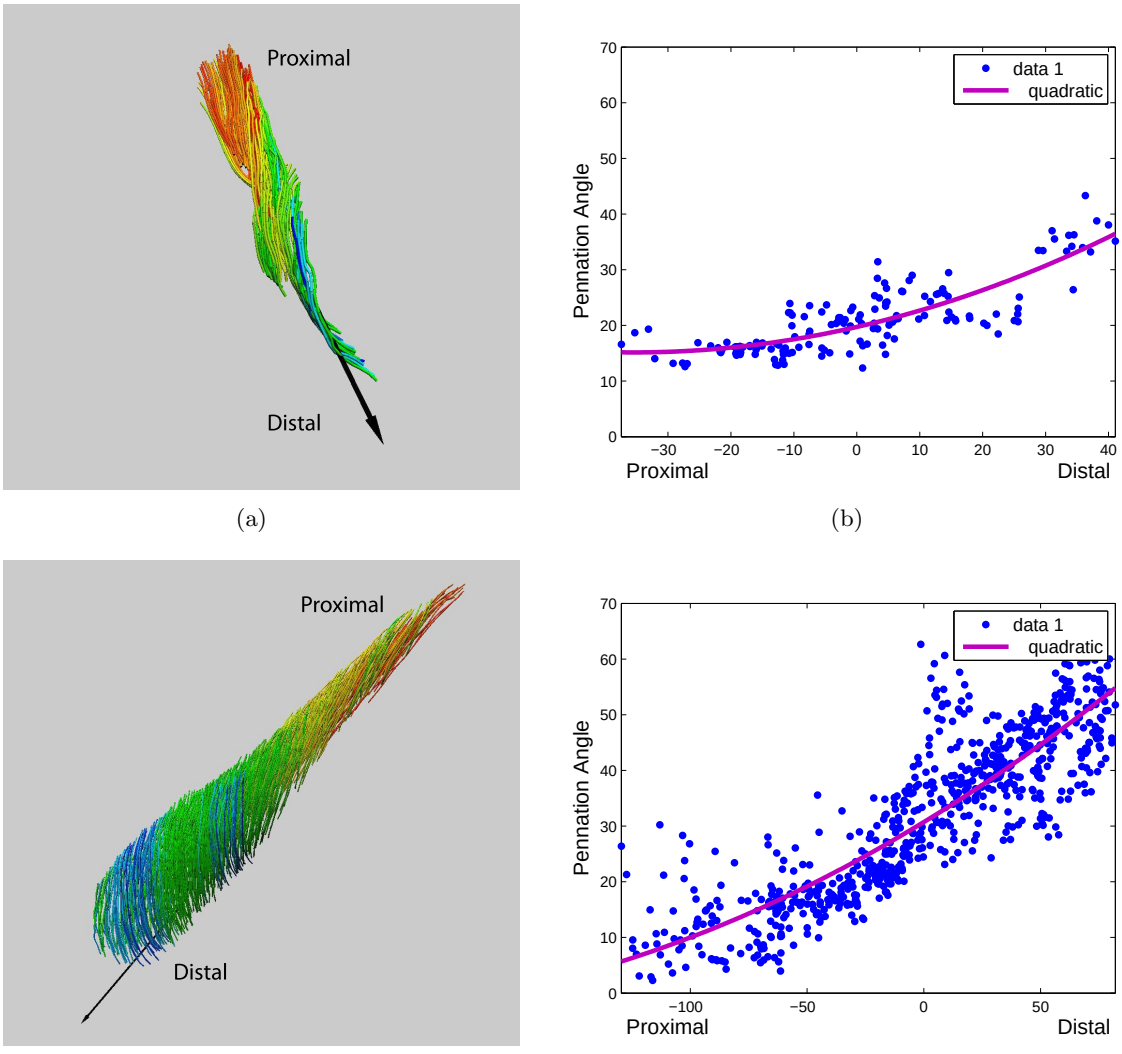

Figure 4.9: PA variation and its correlation with the proximal-distal direction for unipennate muscles. (a) Entire color field of PA for EPB. (b) PA distribution and its fitted model: $y = 0.0036373\,x^2 + 0.25795\,x + 19.721$. (c) Entire color field of PA for VM. (d) PA distribution and its fitted model: $y = 0.00047506\,x^2 + 0.25476\,x + 30.719$.

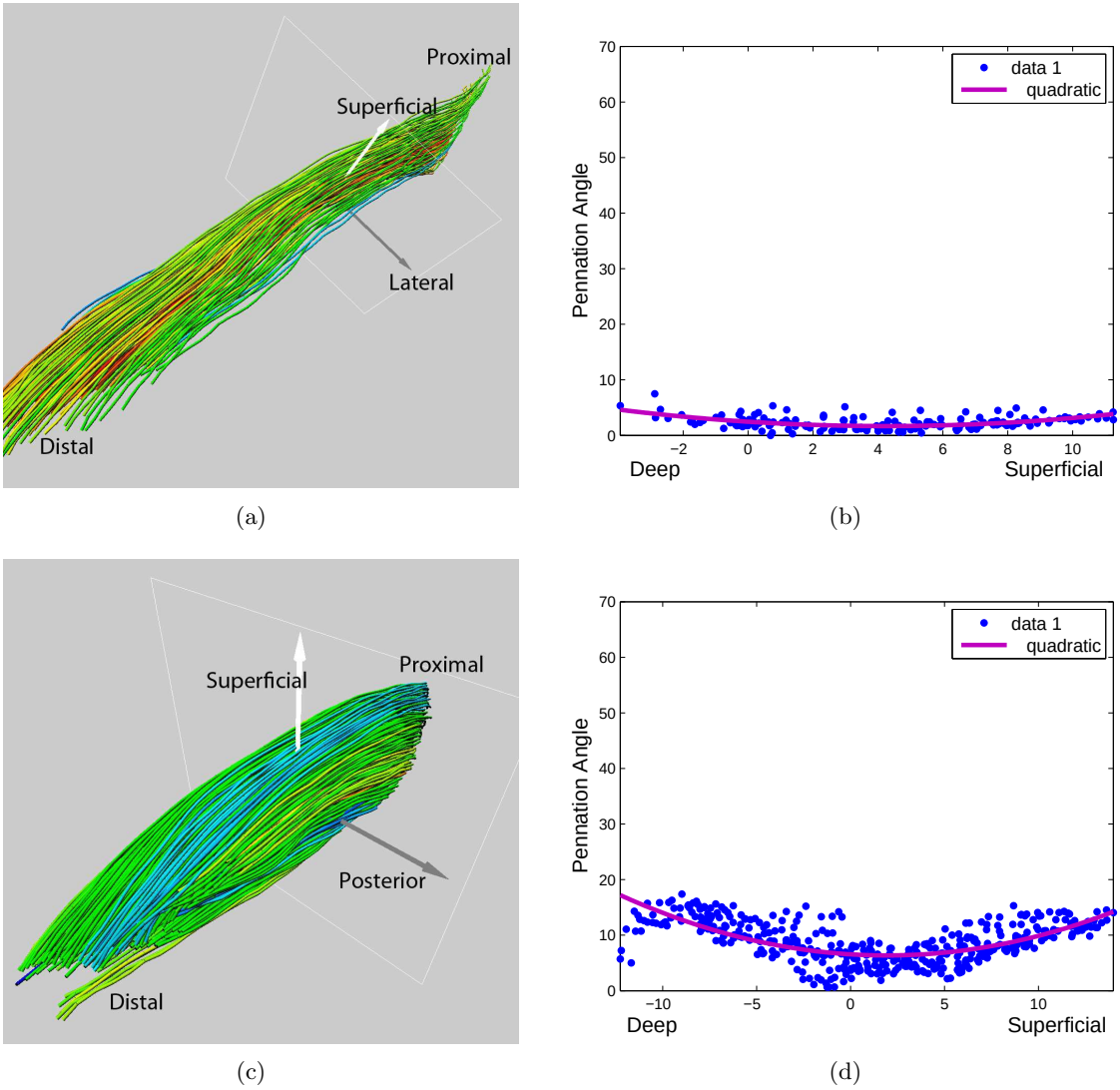

Figure 4.10: PA variation and its correlation with the superficial-deep direction for fusiform muscles. (a) Entire color field of PA for BR. (b) PA distribution and its fitted model: $y = 0.043905\,x^2 - 0.37168\,x + 2.4642$. (c) Entire color field of PA for ECRL. (d) PA distribution and its fitted model: $y = 0.05396\,x^2 - 0.20736\,x + 6.5558$.

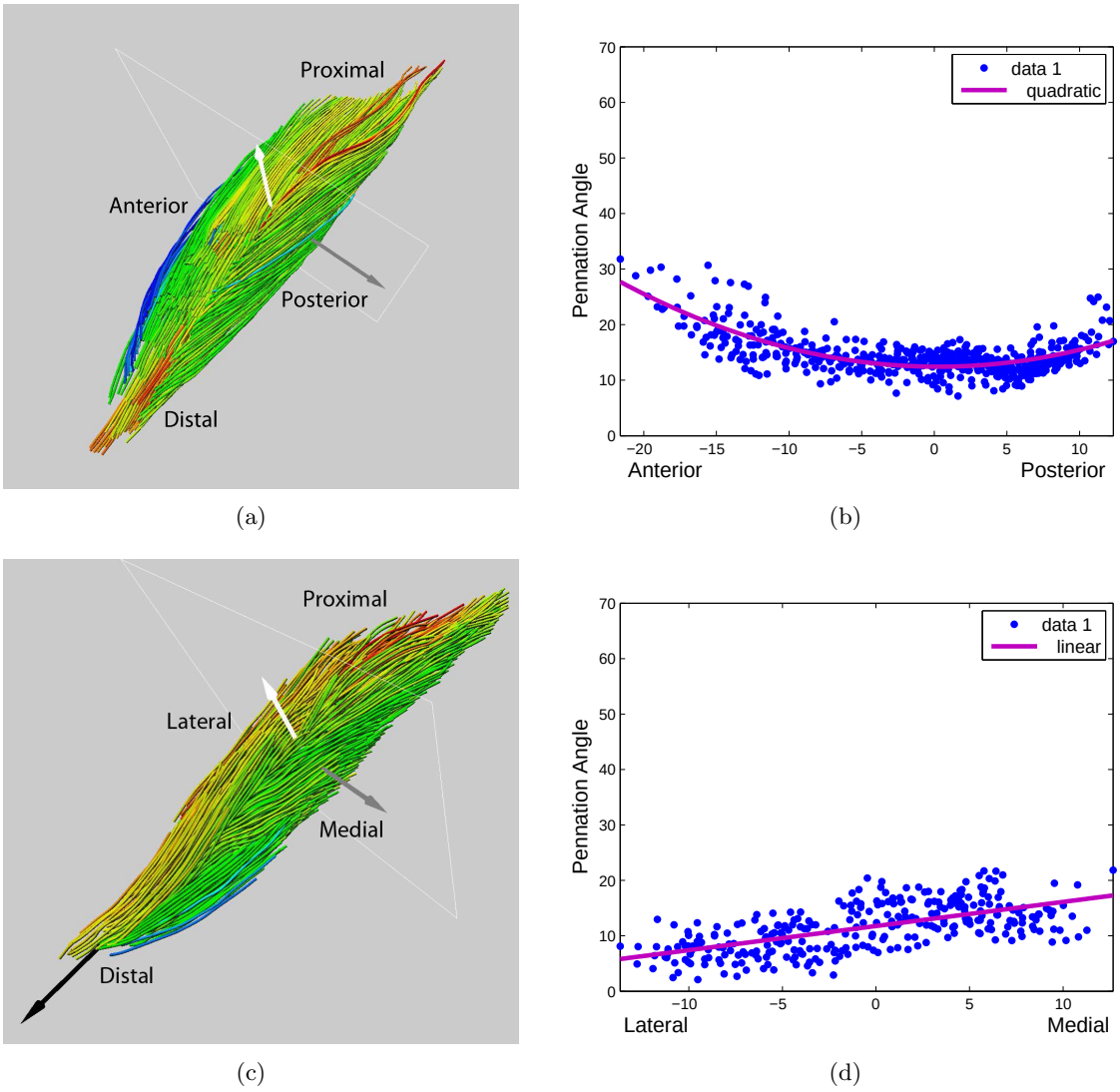

Figure 4.11: PA variation and its correlation with the medial to lateral (or anterior to posterior) direction for bipennate muscles. (a) Entire color field of PA for ECRB. (b) PA distribution and its fitted model: $y = 0.031945\,x^2 - 0.015641\,x + 12.433$. (c) Entire color field of PA for APL. (d) PA distribution and its fitted model: $y = 0.43524\,x + 11.766$.

4.3.3 Comparison of 3D and 2D estimation of PA

The difference between the estimated PA computed by the 3D and 2D methods varies substantially ($1.1\% - 47.1\%$) and depends on the architectural pattern of the muscle. The 2D method yields a smaller estimation of PA than does the 3D method for all but fusiform muscles (BR and ECRL). A significant difference of PA ($37.2\% - 47.1\%$) occurs for fan-shaped muscles (ANC, PM and PQ). For bipennate muscles, the difference of PA varies widely ($1.1\% - 42.2\%$), whereas for unipennate muscles (EPB and VM), the difference is smaller ($6.1\% - 11.9\%$).

Unlike the 3D method, the 2D method does not take all fascicles into account when estimating PA. More specifically, in the 2D method, only a subset of fascicles ($8.1\% - 52.6\%$) that intersect the imaging plane contribute to PA estimation. Furthermore, 2D projection may introduce an angular error. Ultimately, this comparative result is mainly due to how closely the 2D distribution of projected fascicles approximates the entire architecture of the muscle For the 2D method, the mid-longitudinal imaging plane is defined by the proximo-distal and superficial-deep axes. Among the studied muscles, fusiform muscles and unipennate muscles have substantial variation of PA along either the proximo-distal or superficial-deep axis. Since the imaging plane contains both axes, it is likely that the 2D distribution of fascicles shows a similar variation pattern to what is observed in 3D. As fascicles are located farther from the plane, some become more parallel (e.g., BR and ECRL) while others remain oblique to the tendon axis (e.g., EPB and VM). Thus, their PA is close to zero or still considerable, respectively. Since those fascicles do not appear in 2D images, the resulting average PA using the 2D method can be slightly larger or smaller than the PA computed by the 3D method. Fan-shaped muscles and some bipennate muscles (e.g., ECRB and FCU) have a stronger pattern of fascicle angulation along the latero-medial axis than along the other axes. This is rarely captured in the imaging plane. In such cases, the 2D method yields much smaller PA estimates than does the 3D method.

4.4 Discussion

PA is an important architectural parameter used to characterize muscle functions. Ultrasonography is the most commonly used approach to measure PA. It provides 2D assessment based on a hand-held probe. However, 2D assessment is subject to some uncertainty and ambiguity, which may result in under- or over-estimation of PA. This may lead to critical problems in both computational studies and diagnostic treatments. Thus, when using ultrasonography, it is important to find the optimal imaging plane so that PA can be reliably quantified. To do so, requires a good understanding of 3D muscle architecture and the corresponding 2D assessment of the imaging scan. To this end, this study focuses on developing both 3D and 2D approaches to quantifying PA. The proposed 3D approach directly quantifies PA from digitized fascicle data. The geometric analysis of fascicle attachment permits it to handle architectural variation

consistently, without any dependency on it. The volumetric data enable detailed investigations of PA variation that may be characterized with respect to the anatomical axes. The 2D approach, based on simulated ultrasound imaging, is used to compare 3D and 2D measurements. Their difference can be used to assess the resemblance between 3D arrangement of fascicles in space and their projected 2D arrangement.

The proposed 3D method can be directly applied to fascicle data that are obtained by diffusion tensor MRI [55, 26]. However, since this study is based on cadaveric specimen data that were collected invasively, it may not be directly applicable to *in vivo* quantification based on ultrasonography. Nevertheless, it could provide insight into determining a good scanning plane with respect to the underlying muscle architecture. For instance, it is observed that some bipennate muscles (e.g., ECRB and FCU) and fan-shaped muscles have strongly varying PA along the latero-medial axis. If the imaging plane is aligned to include this axis, 2D measurements become more compatible with 3D measurements. This study also suggests that multiple scans should be performed at different positions for muscles having multiple bellies or distinct regions that may have functional differences.

Although this study provides improved capability for PA estimation, there are some limitations to overcome. First, the presented comparative study should be extended to include true ultrasonographic assessment, not just simulated results. This could include a discussion of the structural differences between cadaveric specimens and *in vivo* tissue, which ultimately may help to clarify the association between diagnostic ultrasound imaging and the true underlying anatomical structure. Second, the inter-subject variability, including pathological aspects, is not even discussed because only one specimen was available for most muscles when this study was conducted. More specimens are needed to enable assessment of inter-subject variability using the proposed analytical approach. Last, the proposed 3D method needs to be extended to a variety of *in vivo* problems, including architectural changes associated with muscle contraction. To this end, it would be essential to investigate the integration of 3D architectural modeling and *in vivo* measurements based on medical imaging data.

Chapter 5

Geometric reconstruction of surface and volume for skeletal muscle

5.1 Introduction

Skeletal muscle has a mixture of materials with various physical properties, such as hyperelasticity, incompressibility, contractility and non-homogeneity. Depending on the application, some properties are more accurately accounted for in muscle models than others. Due to their simplicity and versatility, lumped-parameter models are commonly used in a variety of computational musculoskeletal studies. Those one-dimensional models effectively represent uni- or bi-directional muscle contraction but have difficulty in representing volumetric behavior. Furthermore, they may not simulate reliably *in vivo* muscles having complex architecture due to their oversimplification of muscle structures, such as assuming uniform fiber length and arrangement. By comparing with experimental measurements, previous studies [32, 97] demonstrated that force prediction derived from lumped-parameter models unfaithfully varies with respect to change in joint angle, especially for complex muscles. Blemker and Delp [12, 13] circumvent this problem by incorporating varying fiber arrangement with simulated fiber excursions during body movement. For this, the fiber arrangement was modeled as a volumetric vector field and then embedded into hexahedral meshes that were created from magnetic resonance imaging (MRI) data using a finite element mesh generator. This allows them to study complex muscle as well as its *in vivo* behavior. However, since the fiber arrangement is synthesized using predefined templates, the anatomical accuracy and reliability are considerably compromised in their model.

Therefore, this study suggests a geometric method to reconstruct surface and volume of muscle from digitized fascicle data. By assuming that each fascicle can be well approximated by an elliptical cylinder, associated geometric parameters, such as cross-sectional area, are determined and aggregated to represent the entire surface and volume of muscle.

Much of the material in this chapter also appears in the publication [51].

5.2 Methods

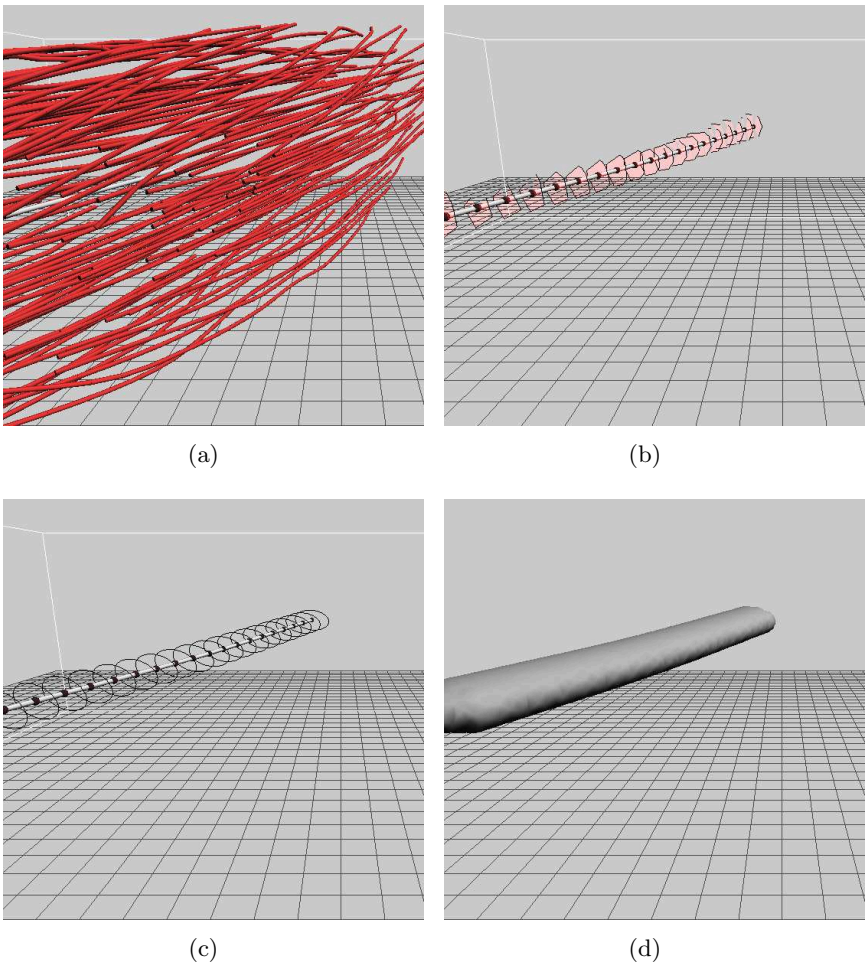

Figure 5.1: Geometric reconstruction of a single fascicle. (a) a chosen fascicle (white). (b) a series of polygons estimating cross-sections of that fascicle. (c) a series of ellipses to approximate those polygons (d) a reconstructed surface.

To reconstruct muscle geometry from digitized fascicles, the polygonal representation of each fascicle (Figure 5.1(b)) is further approximated in parametric form, specifically, elliptical cylinders (Figure 5.1(c)). This parametric form facilitates shape operations (e.g., average, sum and blend) for each fascicle geometry in a simpler but more controlled manner than is possible with the polygonal representation. The least-square-based optimization [25] is used to find an ellipse that fits the polygonal cross-section, $S(\mathbf{p})$. Then, a level set method (otherwise known as an implicit surface method) is used to convert the parametric elliptical representation into a continuous form (Figure 5.1(d)). The elliptical cross-section may be a poor approximate for

certain fascicles having irregular shapes (e.g., concavity) but this is not too problematic for reconstruction of a muscle surface. Because multi-layers of connective tissues (e.g., epimysium and endomysium) and other tissue components (e.g., fat) around fascicles can be considered as additional factors to moderate those irregularities and make their shapes more uniformly smooth. Typically, a level set function is defined as

$$\phi(\mathbf{x}, \mathbf{p}, r) = \| \mathbf{x} - \mathbf{p} \| - r \tag{5.1}$$

where $\mathbf{x}$ is a position to be evaluated and r is the desired strength of the field at $\mathbf{p}$. The set of $\mathbf{x}$ for which (5.1) is zero forms a bounding solution surface (i.e., isosurface). Taking into account that ellipses of a particular orientation are used in this study, equation (5.1) is extended to

$$\begin{aligned} \phi_a(\mathbf{x}', \mathbf{p}, \mathbf{A}) &= [(\mathbf{x}' - \mathbf{p})^T \mathbf{A} (\mathbf{x}' - \mathbf{p})]^{\frac{1}{2}} - 1.0 \\ \mathbf{A} &= \begin{bmatrix} A & B/2 & D/2 \\ B/2 & C & E/2 \\ D/2 & E/2 & F \end{bmatrix} \end{aligned} \tag{5.2}$$

where the symmetric positive-definite matrix $\mathbf{A}$ is built from an ellipse in the quadratic polynomial form, $Ax^2 + Bxy + Cy^2 + Dx + Ey + F = 0$, and $\mathbf{x}'$ is a point which lies on the transverse plane at $\mathbf{p}$ on the fascicle. Equation (5.2) is evaluated on the transverse plane and swept along the fascicle to create a cylindrical geometry.

Because fascicles are reconstructed individually, they may become disjoint, thereby separating from each other (Figure 5.2(b)). To model an entire muscle surface, including all other connective tissues, such as epimysium, perimysium and endomysium, level sets associated with each fascicle should be joined with appropriate overlaps. For this, the proposed method uses interpolation based on weighted local averaging [113] of neighboring fascicles (Figure 5.2(c)). To this end, let

$$\begin{aligned} \phi_p(\mathbf{x}', \overline{\mathbf{p}}, \overline{\mathbf{A}}) &= [(\mathbf{x}' - \overline{\mathbf{p}})^T \overline{\mathbf{A}} (\mathbf{x}' - \overline{\mathbf{p}})]^{\frac{1}{2}} - 1.0 \\ \overline{\mathbf{p}} &= \sum_i w_i \mathbf{p}_i \\ w_i &= \frac{k(\| \mathbf{x}' - \mathbf{p}_i \|)/R}{\sum_j k(\| \mathbf{x}' - \mathbf{p}_j \| /R)} \end{aligned} \tag{5.3}$$

where $\overline{\mathbf{A}}$ represents a locally averaged ellipse and k is a kernel function which is symmetric and smoothly decays with local support, R. $k(t) = \mathrm{MAX}(0, (1 - t^2)^3)$ is used. Using (5.2) or (5.3), a scalar field is densely sampled on a 3D grid, with spacing specified as 1.0 mm in this study, and the corresponding mesh is extracted using a polygonisation technique. A BCC grid-based technique [46] is used to directly extract a tetrahedral mesh (Figure 5.2).

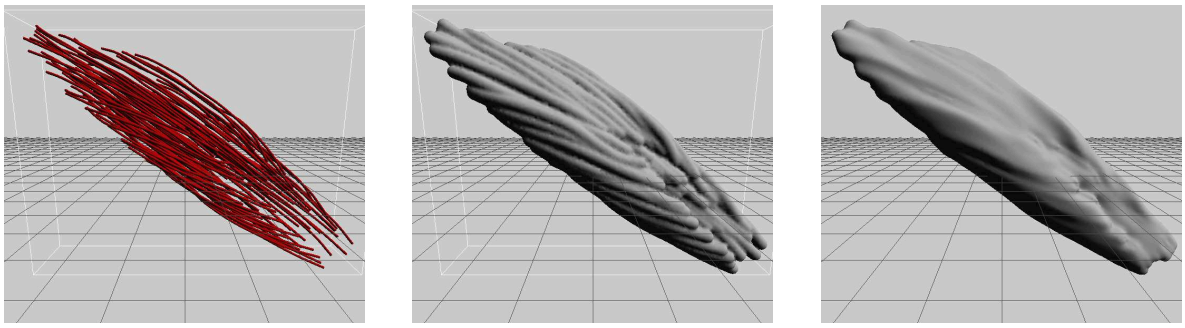

(a) (b) (c)

Figure 5.2: Reconstruction of muscle geometry. (a) spline-based fascicles. (b) reconstruction of fascicles (without interpolation). (c) reconstruction of entire muscle (with interpolation).

Muscle	Volume	Volume^c	Volume^t
Parallel^1	392.7	393.5 (+0.2)	342.3(−12.8)
Parallel^2	392.7	395.5 (+0.7)	350.2(−10.8)
Unipennate^1	1047.2	979.3(−6.4)	934.1(−10.8)
Unipennate^2	1047.2	981.8(−6.2)	965.9(−7.7)

Table 5.1: Comparative results for volume (cm^3). Volume^c is an approximate volume computed by a collection of cylinders. Volume^t is an approximate volume computed by a tetrahedral mesh. Percentage of relative errors are given in parenthesis.

5.3 Result

For geometry reconstruction, a 1 mm grid is used for all specimens except PM for which a 2 mm grid is used instead because the size of PM demands a tremendous memory allocation. The level-set method performs poorly for PM and SS, in which many cross-sections of fascicles are estimated to be smaller than the grid-size. Thus, a finer grid must be used to reduce the difference. To validate the proposed method, volume estimates of synthetic data (described in Section 3.2.2) are compared in Table 5.1. First, the volume (Volume^c) is approximated by a collection of cylinders, formed by cross-sections along the fascicle length. That is, $\sum_{i=1}^{n} \overline{A_i} l_i$ where $\overline{A_i}$ is the approximate cross-sectional area of fascicle i and l_i is its length. Volume can also be calculated from the reconstructed muscle geometry. Since the proposed approximation to the muscle geometry consists of tetrahedra, muscle volume (Volume^t) is approximated by the sum of volumes of tetrahedra. As only fascicle volume is considered, muscle geometry is reconstructed by (5.2). Volume^c in Table 5.1 is close to the exact volume. On the other hand, Volume^t in Table 5.1, which is computed from the volume of tetrahedral mesh, has significantly larger errors ($8 - 13\%$). This is caused mainly by errors that arise in both obtaining the parametric form and polygonising the level set surfaces.

Muscle	n	Volume^c	Volume^t
ECRB	128	21.33	20.33
	93	12.01	12.23
	117	17.32	16.36
	106	18.72	18.24
	106	14.45	12.18
	178	8.81	8.47
	126	16.83	16.22
ECRL	116	28.37	26.49
	87	13.37	13.68
	62	15.66	15.23
	74	27.92	24.1
	76	15.54	14.74
	105	11.86	11.44
	92	17.67	16.66
PM	634	277.1	246.78
	679	224.4	171.36
	767	206.7	169.69
	873	188.7	140.3
SS	1750	45.7	38.23
	1081	33.7	25.35
	1684	39.18	28.68
	1061	38.38	31.71
	1294	52.26	42.91
	1556	64.71	53.7

Table 5.2: PCSA (cm^2) and volume (cm^3) estimation for specimen data by the proposed method; n is the number of digitized fascicles.

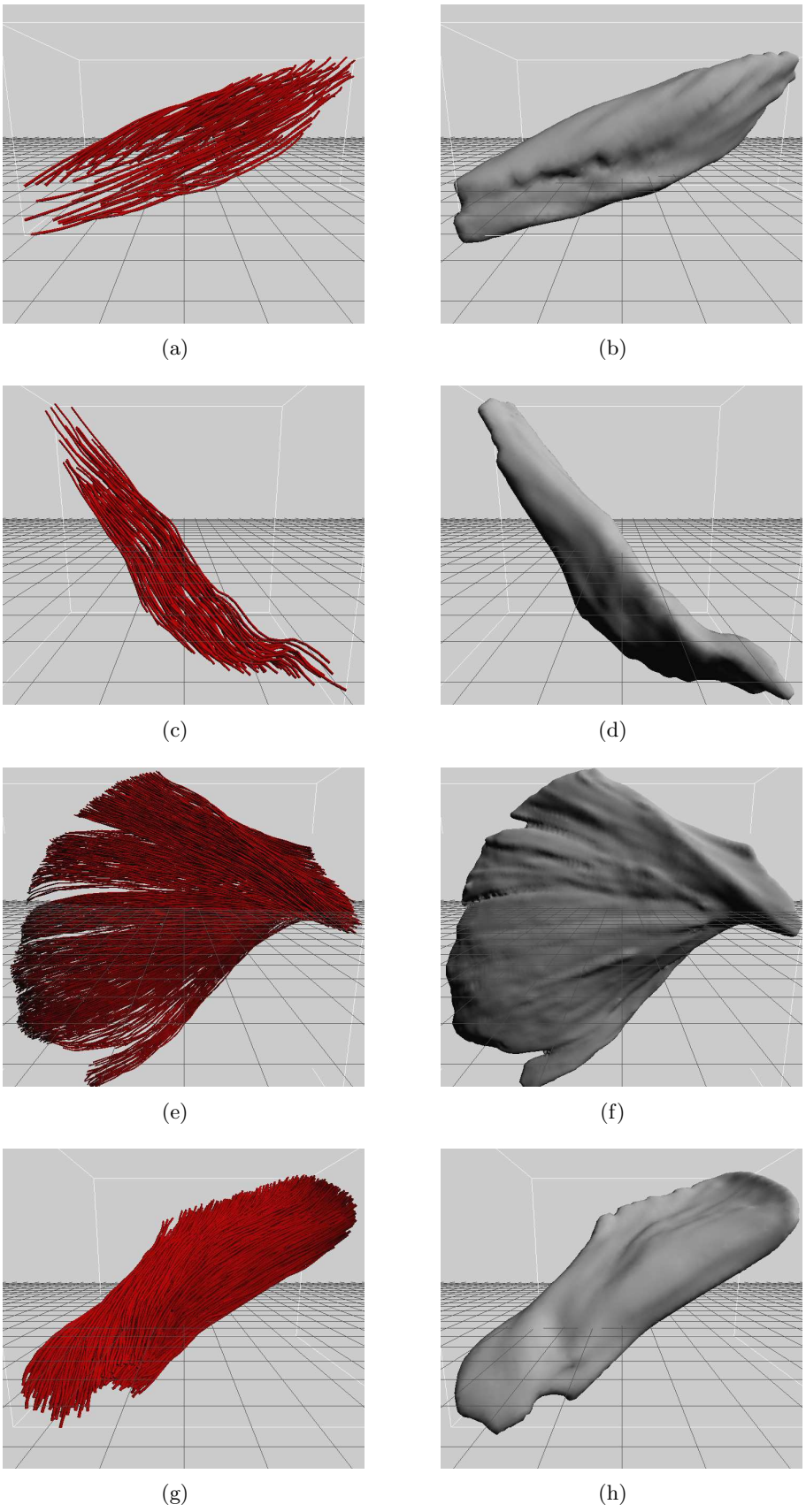

Figure 5.3: Reconstruction of muscle geometry. Muscles are illustrated in two representations: fascicles (on left) and reconstructed surface geometry (on right). ECRB (a,b), ECRL (c,d), PM (e,f) and SS (g,h).

5.4 Discussion

The geometric method is proposed to reconstruct the entire surface and volume of muscle from digitized cadaveric specimens. As associated geometric parameters are determined based on the underlying architecture, the reconstructed surface and volume geometries fit well into the fascicle arrangement. Thus, any further mapping or registration is not needed. Those geometries are represented by polygonal meshes that can be used to visualize the approximated shape of muscle and its dynamic simulation as well. Not only the entire surface and volume of a muscle, but also region-specific reconstruction (e.g., anterior, posterior, superficial or deep region) can be provided, which allows for further intramuscular analysis.

However, there are some issues to discuss. Firstly, the accuracy of the reconstruction needs to be assessed by further validation, such as other medical imaging (e.g., MRI) or 3D scanning methodologies. Secondly, parameterisation of cross-sections needs to be improved. These cross-sections are individually and locally approximated by parametric ellipses. Even though the thickness of a fascicle changes smoothly, the least-squares-based estimation of serial cross-sections may vary abruptly depending on the availability of their neighbors. Incorporating the correlation between adjacent cross-sections or global constraints may produce more reliable and consistent parameterisation than the localized method does. Thirdly, there exist some limitations inherent to the geometric methods that used in this study. The proposed approach does not model very thin muscles very well. As this muscle can be digitized with having thickness of one or two fascicles, associated cylindrical parameters may not be approximated accurately due to insufficient proximity around every fascicle. Also the level set method is not capable of modeling thin objects well. One possible solution is to create a thicker volume of muscle then adaptively re-scale it until the fascicles are tightly enclosed. Lastly, there is another important aspect of the problem that is currently handled in an ad hoc way. To extract muscle geometry, level sets of all fascicles must be properly interpolated with acceptable overlaps. As the overlap increases, the resulting muscle surface becomes smoother but shrinks. Otherwise, the surface breaks into disjoint fascicles. Thus, accurate reconstruction of muscle geometry needs the determination of appropriate overlaps, which is left as a topic for future work.

Chapter 6

A practical approach to *in-vivo* quantification of PCSA for skeletal muscle

6.1 Introduction

Physiological cross-sectional area (PCSA) is an important determinant of peak muscle force production during body movement. Since force predictions are known to be highly sensitive to changes in PCSA [17], reliable functional analysis requires accurate determination of PCSA. An algebraic method is commonly used to calculate PCSA based on muscle volume (MV), fascicle length (FL) and pennation angle (PA) that are estimated by magnetic resonance imaging (MRI) and ultrasonographic assessments. However, this method does not account well for intramuscular variation of architecture, which may lead to under- or over-estimation of PCSA. Furthermore, the high cost of an MRI examination may limit its application. On the other hand, cadaveric specimen-based studies determine the muscle architecture at the fascicular level to provide capacity for an in-depth understanding of PCSA associated with architectural complexity and variation of muscle. However, as detailed architectural and structural data are nearly impossible to obtain from living tissues, this approach may not be directly applicable to *in vivo* studies. Furthermore, compared to living tissues, cadaveric tissues are subject to volumetric shrinkage during the embalming and dehydration processes, necessitating an appropriate adjustment for accurate quantitative analysis.

The purpose of the study in this chapter is to propose a practical approach to the quantification of PCSA for *in-vivo* muscle by integrating both cadaveric studies and *in-vivo* ultrasonographic assessments. This study hypothesizes that three-dimensional *in-vivo* muscle architecture can be approximated by mapping 3D cadaveric data onto 2D *in-vivo* ultrasound imaging data. This hypothesis is based on two assumptions: (1) the same muscles in different subjects are

similar to each other in overall architectural pattern and geometric topology and (2) the inter-subject variability can be globally estimated by representative geometric measurements, such as cross-sectional area and muscle length. The 3D internal architecture and the external surface reconstructed from cadaveric specimens are referred to as the source data and a set of 2D measurements (e.g., cross-sections, length and sampled fascicle orientation) from ultrasound images are referred to as the target data. However, it is not straightforward to directly match the source data with the target data, using an approach such as the point to point correspondence, due to the dimensionality difference between these data (i.e., 3D volume vs 2D image). Instead, a feature-based matching approach is used, in which by using simulated ultrasound, corresponding 2D features (e.g., cross-section, length, 2D fascicle orientation) are obtained from the source data and compared with those of the target data. By either expanding or shrinking the volume of the source muscle, the 3D architecture and surface geometry in the source data are transformed so that the measurement difference between those features is minimized. The three-dimensional estimation method for PCSA is then applied to the transformed muscle architecture that is the proposed *in-vivo* muscle model.

Much of the material in this chapter also appears in the publication [49].

6.2 Methods

6.2.1 *In-vivo* ultrasonographic assessment

For the ultrasonographic assessment of the supraspinatus, five subjects were recruited. Subjects with a history of rotator cuff pathology or neuromuscular disease were excluded. An HDI 5000 Advanced Technology Laboratories (ATL) real-time ultrasound scanner with a linear (38 mm) 12 MHz transducer (resolution 0.3 mm) was used to scan all subjects in relaxed states, with respect to the protocol developed by Kim et al. [41]. A longitudinal image was obtained by positioning the probe at the anterior region of the muscle and aligning it to the intramuscular tendon. A transverse image was captured by positioning the probe at the middle of muscle belly and aligning it to the sagittal plane. Two additional transverse images were obtained by translating the probe proximally or distally (one-fourth and three-fourths of the proximo-distal length). The intramuscular tendon and the observed fascicles were manually determined by superimposing lines onto the longitudinal image. Anatomical cross-sections of the muscle were also manually digitized by smooth curves in the transverse images (See Figure 6.1).

6.2.2 Cadaveric modeling

Cadaveric assessment uses seven supraspinatus specimens that were acquired using dissection and digitization. Specimens with visible abnormalities, such as muscle atrophy, fat infiltration

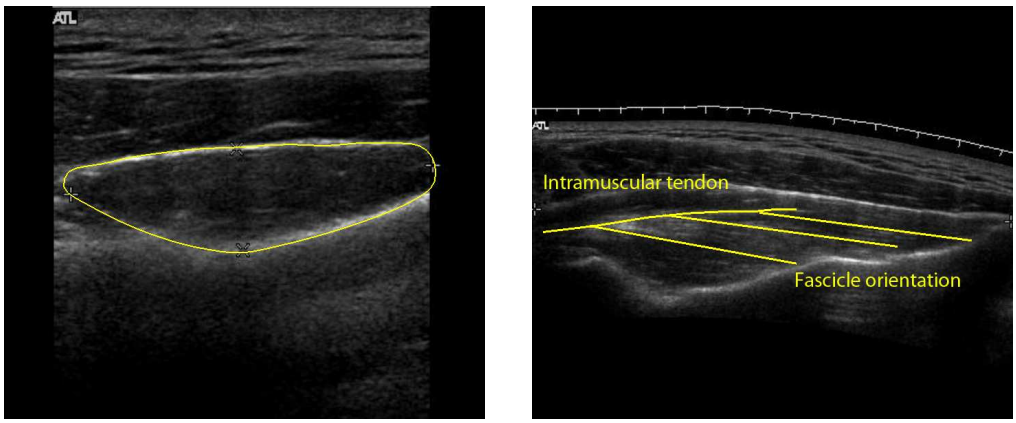

(a) (b)

Figure 6.1: *In-vivo* ultrasonographic assessment for the supraspinatus: (a) Segmented cross-sectional area of the transverse image. (b) Sampled fascicles and intramuscular tendon of the longitudinal image.

and surgery, were excluded from the data acquisition. During dissection and digitization, associated joints were stabilized into anatomical position with metal plates and screws. Fascicles were sequentially dissected and digitized from superficial to deep throughout the muscle volume. A MicroScribe G2 digitizer with 0.23 mm accuracy was used to trace trajectories of fascicles with sampled points. Digitized fascicles were removed, exposing the underlying fascicles about $1-2$ mm deeper. To identify fascicle trajectory accurately, a surgical microscope was used throughout the dissection and digitization process. A cubic Catmull-Rom spline was used to reconstruct fascicles and associated architectural parameters, such as FL, PA, PCSA and MV, were quantified [51, 50]. Based on these parameters, an external surface geometry was reconstructed (See Figure 6.2(a)). To be comparable to the ultrasonographic assessment, transverse and longitudinal images are created by the intersection of muscle geometry and imaging planes (See Figure 6.2(b) and 6.2(c)). Section contours are represented by 2D polygons, whereas fascicles are shown as intersection points (in the transverse image) or projected 2D line segments (in the longitudinal image) [50].

6.2.3 Data generation for synthetic muscles

In addition to an analysis based on specimen data, synthetic data are used to validate the proposed method. The synthetic data are produced by choosing parametric equations to represent targeted geometries: cylinder and ellipsoid. Fascicles are then populated and arranged with respect to predefined architectures: parallel for cylinder and bipennate for ellipsoid (See Figure 6.3). The validating experiment uses two parallel muscles, parallel_1 (length of 20 mm and radius of 12 mm) and parallel_2 (length of 20 mm and radius of 10 mm), and two bipennate muscles, bipennate_1 (length of 25 mm, width of 13 mm, height of 13 mm and pennation angle of

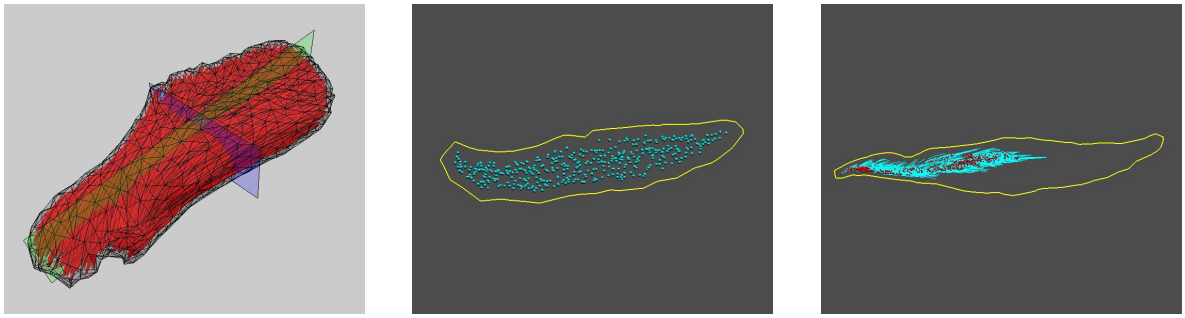

(a) (b) (c)

Figure 6.2: Cadaveric assessment of the supraspinatus: (a) Reconstructed architecture and surface with the transverse (mid-sagittal) and mid-longitudinal planes. (b) Cross-section image produced by the intersection of the transverse plane and the muscle geometry. (c) Longitudinal image produced by the intersection of the mid-longitudinal plane and the muscle geometry. Contour outlines (yellow), fascicles (cyan) and distribution of distal attachment (red) are shown in images (b) and (c).

20°) and bipennate$_2$ (length of 20 mm, width of 10 mm, height of 10 mm and pennation angle of 25°). These synthetic data have uniform architecture without any intramuscular variation of FL and PA within the muscle.

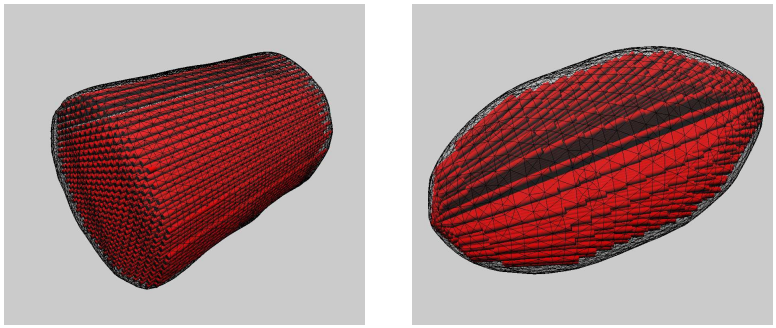

(a) (b)

Figure 6.3: Synthetic muscles. (a) Parallel muscles are created within a cylinder. (b) Bipennate muscles are created within an ellipsoid.

6.2.4 Mapping of muscle architecture

To map the architecture of the source muscle onto that of the target muscle, this study uses two ways to represent muscle volume. One is to estimate volume based on the architecture (by (6.1)); the other is to determine volume based on the external geometric measurement (by (6.2)). Using these two representations, it is possible to approximately associate the internal architecture with the external measurement per muscle and then determine architectural variation between the source and target muscles, which is used for the mapping. In a cadaveric muscle, the volume of each fascicle is approximately modeled by a cylinder along its trajectory. As the entire muscle

architecture is represented by a collection of those cylinders, the muscle volume (MV) can be estimated by

$$\mathrm{MV} = \sum_{i=1}^{n} a_i l_i \tag{6.1}$$

where a_i is the cross-sectional area of fascicle i, l_i is the length of fascicle i and n is the number of fascicles. As the reconstructed surface encloses all fascicles, muscle volume is also approximated by summing the cross-sectional slices times their thickness:

$$\mathrm{MV} = \sum_{k=1}^{m} c_k \Delta h = \sum_{k=1}^{m} c_k \frac{h}{m} = \bar{c} h \tag{6.2}$$

where c_k is a cross-sectional area of k-th slice of the muscle, m is the number of cross-sections, h is the length of the muscle, $\Delta h = \frac{h}{m}$ is the average thickness of each cross-section and $\bar{c} = \frac{1}{m}\sum_{k=1}^{m} c_k$ is the average cross-sectional area. Using (6.2), an inter-subject variability of muscle volume can be approximated. For a target muscle having volume MV^t and source muscle having volume MV^s, let $\alpha = \frac{\mathrm{MV}^t}{\mathrm{MV}^s}$ be the scaling factor between the target and source muscles. The scaling factor α can be estimated as the product of relative cross-sectional area (α_c) and length (α_h) between muscles:

$$\alpha = \alpha_c \alpha_h,\ \alpha_c = \frac{\overline{c^t}}{\overline{c^s}},\ \alpha_h = \frac{h^t}{h^s} \tag{6.3}$$

where $\overline{c^s}$ and $\overline{c^t}$ are the average c_k of the source and target muscles, respectively, and h^s and h^t are the length of the source and target muscles, respectively. Using the results above, the volume of the target muscle can be rewritten in terms of the architecture of source muscle as

$$\mathrm{MV}^t = \sum^{n^t} a_i^t\, l_i^t = \alpha_c \alpha_h \sum^{n^s} a_i^s\, l_i^s \tag{6.4}$$

where superscript s and t indicate the source and target muscles, respectively. Since $\bar{c}$ and h can be measured from both cadaveric and ultrasonographic assessments, it is straightforward to determine α_c and α_h. The values of α_c and α_h are used to explicitly transform the source muscle so that its volume approximates the volume of the target muscle. For simplicity, the transformation is decomposed into two sub-transformations: transverse and longitudinal transformation. The transverse transformation minimizes the difference in the cross-sectional areas between the source and the target muscles, whereas the longitudinal transformation is used to match the lengthes of the muscles.

6.2.5 Transverse transformation

A 3D geometry of the target muscle is approximated by either shrinking or expanding that of the source muscle. For simplicity, the transformation is restricted to the transverse plane.

The amount of shrinking or expanding is determined by the scaling factor, α_c in (6.3), which is used to minimize the difference in the cross-sectional areas between the source and the target muscles. In transverse ultrasound images, the cross-sectional area of a muscle is approximated by a polygon, the area of which is calculated by manual digitization. The value of $\overline{c^t}$ is obtained by averaging cross-sectional areas, c_k^t, estimated from three transverse images. To be consistent with ultrasonographic assessment, three transverse images are created from cadaveric muscle data by using the simulated ultrasound (described in Section 4.2.6) positioned at the corresponding locations (i.e., $\frac{1}{4}$, $\frac{1}{2}$ and $\frac{3}{4}$ of the proximo-distal axis). The intersections of the transverse plane centered at those locations and muscle surface produce three polygonal cross-sections, C_k^s $(k = 1, 2, 3)$, the areas (c_k^s) of which are averaged to obtain $\overline{c^s}$.

For each cross-section C_k^s, its nearby vertices on the surface are identified as G_k to constitute $G = \bigcup_k G_k$. Since the transformation is restricted to the transverse plane and it is uniform around the surface, new positions for vertices in G can be simply defined by symmetrically displacing them inward or outward from the surface. The amount of displacement is determined so that the associated cross-sectional area can be transformed to achieve the target value; $c_k^{s'} = \alpha_c c_k^s$. As the cross-section is represented by a closed polygon having a number of boundary points, its area is calculated as

$$c_k^s = \frac{1}{2} \sum_{i=1}^{n^e} \mathbf{n}_t \cdot (\mathbf{p}_i - \mathbf{x}_o) \times (\mathbf{p}_{i+1} - \mathbf{x}_o) \tag{6.5}$$

where $\mathbf{n}_t$ is a normal of the transverse plane, $\mathbf{x}_o$ is an arbitrary point on that plane, n^e is the number of edges representing the boundary of the cross-section, and $\mathbf{p}_i$ and $\mathbf{p}_{i+1}$ are the end points on the edge i. These boundary points $\mathbf{p}$ are determined by intersection of the transverse plane and the muscle surface. Likewise, a new cross-sectional area is calculated in terms of the displacement from the original points:

$$c_k^{s'} = \frac{1}{2} \sum_{i}^{n^e} \mathbf{n}_t \cdot (\mathbf{p}'_i - \mathbf{x}_o) \times (\mathbf{p}'_{i+1} - \mathbf{x}_o) \tag{6.6}$$

$$\mathbf{p}'_i = \mathbf{p}_i + \Delta r_k \mathbf{t}(\mathbf{p}_i) \tag{6.7}$$

where $\mathbf{t}(\mathbf{p}_i)$ is the unit vector representing the normal traction at $\mathbf{p}_i$ and Δr_k is the displacement along the traction. Substituting (6.7) into (6.6) solves for Δr_k to make (6.6) equal to the target value $c_k^{s'} = \alpha_c c_k^s$ $(k = 1, 2, 3)$. Similar to (6.7), new positions for vertices in G_k are determined by using Δr_k:

$$\mathbf{u}_i = \mathbf{v}_i + \Delta r_k \mathbf{t}(\mathbf{v}_i) \tag{6.8}$$

where $\mathbf{t}(\mathbf{v}_i)$ is the unit vector representing the normal traction at $\mathbf{v}_i$ (See Figure 6.4).

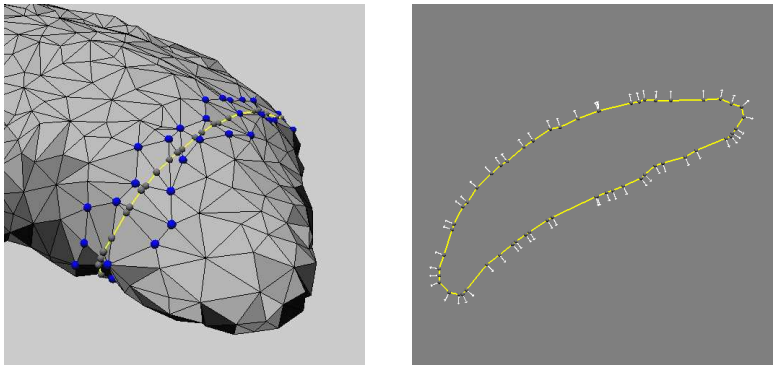

(a) (b)

Figure 6.4: Displacement for transverse transformation: (a) Cross-section C_k^s (yellow) with boundary points, $\mathbf{p}$ (gray), and adjacent vertices, G_k (blue), subject to the constraint in the transformation. (b) 2D view of cross-section with the displacement (white).

The muscle surface is reconstructed based on the enclosed fascicles, the trajectories of which directly represent geometric details of the surface. This geometric correspondence between the surface and fascicle arrangement is used to approximate the new architecture associated with the transformed surface. Thus, geometric surface details must be preserved as much as possible during the transformation. To this end, the Laplacian surface deformation technique [90] is used because it allows us to effectively transform global shape while preserving local details. These details are represented by the Laplacian coordinates to be described as the difference between the vertex and the average of its neighboring vertices:

$$\delta_i = \mathcal{L}(\mathbf{v}_i) = \mathbf{v}_i - \frac{1}{d_i}\sum_{j \in N_i} \mathbf{v}_j \tag{6.9}$$

where N_i is the set of vertices adjacent to $\mathbf{v}_i$ and d_i is the number of elements in N_i. The surface is transformed by constraining a set of vertices to the desired positions and fitting the Laplacian coordinates of new surface $\mathbf{v}'$ to the initial Laplacian δ of the original surface:

$$\mathbf{v}' = \arg\min_{\mathbf{v}}(||\mathcal{L}(\mathbf{v}) - \delta||^2 + \sum_{i \in G} \omega_i ||\mathbf{v}_i - \mathbf{u}_i||^2) \tag{6.10}$$

where $\mathcal{L}(\mathbf{v}) = (\mathcal{L}(\mathbf{v}_1), \mathcal{L}(\mathbf{v}_2), ..., \mathcal{L}(\mathbf{v}_n))^T$, $\delta = \mathcal{L}(\mathbf{v}^o) = (\delta_1, \delta_2, ..., \delta_n)^T$, n is the number of vertices on the surface, G is a set of vertices subject to the constraint during the transformation, $\mathbf{u}_i$ is the positional constraint (i.e., desired position) for $\mathbf{v}_i$ given by (6.8) and ω_i is its weight.

The supraspinatus is a pennate muscle for which fascicles originate from the broad proximal

region and insert into the narrow distal region. With this convergent fascicle orientation, their distal attachment exhibits strong linearity along the intramuscular tendon. Since the surface transformation determines the internal fascicle arrangement, a large transformation (e.g., $\alpha_c \ll 1$ or $\alpha_c \gg 1$) may perturb the architectural pattern that needs to be preserved. To this end, an additional static constraint ($\mathbf{u}_i = \mathbf{v}_i$) is used to restrict the movement of the vertices wrapping around the distal tendon. By incorporating this static constraint, (6.10) is expanded as

$$\mathbf{v}' = \arg\min_{\mathbf{v}}(||\mathcal{L}(\mathbf{v}) - \delta||^2 + \sum_{i \in G} \omega_i ||\mathbf{v}_i - \mathbf{u}_i||^2) + \sum_{j \in S} \omega_j ||\mathbf{v}_j - \mathbf{u}_j||^2) \tag{6.11}$$

where S is a set of vertices constituting the distal tendon area on the muscle surface.

While the surface is transformed by (6.11), the enclosed fascicles need to be transformed similarly, while ensuring that the appropriate geometry is maintained (See Figure 6.5). To this end, this study uses the generalized mean value coordinates technique [40], the common application of which is to manipulate object deformation by means of a surrounding control mesh. This technique geometrically associates the vertices of an arbitrary object with those of a control mesh, which embraces the construction of a weight function, w (namely, mean value coordinates) having the following properties: continuity, smoothness and linear precision. For a detailed description of this technique, the reader is referred to Ju et al. [40]. For the purpose of this study, the enclosed fascicles and their surrounding surface are considered to be the deformable object and the control mesh, respectively. For every fascicle point $\mathbf{x}_j$, its mean value coordinates w_i are computed with respect to each vertex $\mathbf{v}_i$ in the original surface (i.e., prior to the transformation) and set as constant during the transformation. By letting $\mathbf{v}'_i$ be the positions of the vertices from the transformed surface, the new interior fascicle point, $\mathbf{x}'_j$ in the enclosing surface is computed as

$$\mathbf{x}'_j \quad = \quad \frac{\sum_i^n w_{ij} \mathbf{v}'_i}{\sum_i^n w_{ij}} \tag{6.12}$$

where n is the number of vertices on the surface, w_{ij} is the mean value coordinate described in [40], for $\mathbf{x}_j$ and $\mathbf{v}_i$.

6.2.6 Longitudinal transformation

The longitudinal transformation not only matches the length of the muscles, but also minimizes the PA difference between the muscles. In contrast to the transverse transformation, it is directly applied to the fascicle arrangement because it is straightforward to adjust the length and the angle based on the fascicle trajectory. To minimize the perturbation of the tendinous at-

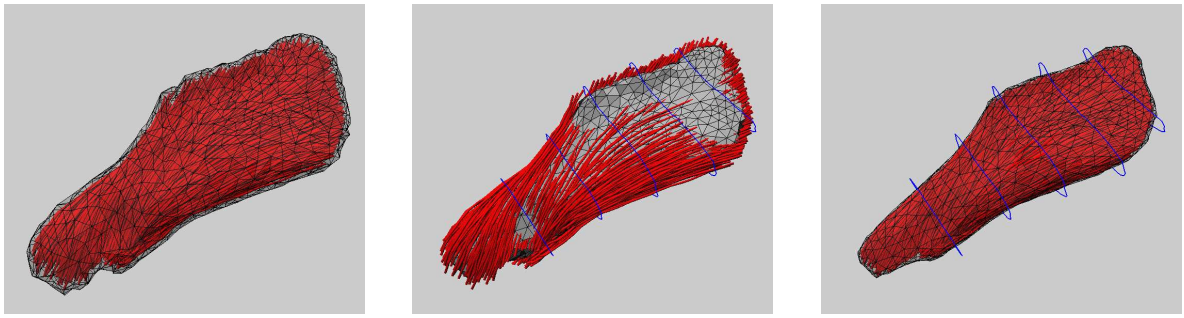

(a) (b) (c)

Figure 6.5: Transverse transformation for the supraspinatus: (a) Architecture (red) and its enclosing surface (transparent). (b) Transformed surface (gray) with respect to specified constraints. (c) Transformed architecture (red) corresponding to the transformed surface (transparent).

tachment, the transformation is restricted to the direction of the intramuscular tendon. While fascicles are fixed at the proximal attachment, they are elongated or shortened by translating their distal attachment along the tendon direction. Similar to (6.10), a least-squares-based optimization is used to transform the fascicle trajectory while preserving local curvatures. Associated translational displacements (Δh_1 and Δh_2) are specified with respect to the scaling factor in (6.3), and PA measurement, respectively.

$$\Delta h_1 = \alpha_h h^s - h^s \tag{6.13}$$

$$\Delta h_2 = \arg\min_{\Delta h} \left(\sum_i^{n^f} \cos^{-1} \left(\mathbf{a}^s \cdot \frac{(\mathbf{t}_i^s + \Delta h\, \mathbf{a}^s)}{||(\mathbf{t}_i^s + \Delta h\, \mathbf{a}^s)||} \right) - \overline{\mathrm{PA}_{2D}^t} \right)^2 \tag{6.14}$$

where n^f is the number of fascicles in the source muscle visible by the simulated ultrasound, $\mathbf{a}^s$ is the direction of the intramuscular tendon, $\mathbf{t}_i^s$ is the tangent of fascicle i at the distal attachment in the source muscle and $\overline{\mathrm{PA}_{2D}^t}$ is the average PA of fascicles sampled on the imaging plane in the target muscle. To be comparable with ultrasonographic assessment, the simulated ultrasound is used, in which a two-dimensional image is created from cadaveric muscle data by projecting its fascicles onto the mid-longitudinal plane. Their proximity to that plane is evaluated to identify visible portions of fascicles. All parameters given in (6.14) are based on 2D measurement. Ultrasonographic assessment accounts for three fascicles sampled at the most proximal, middle and most distal locations of the intramuscular tendon, which approximate the PA distribution of the target muscle in 2D. In contrast, cadaveric assessment takes into account all visible fascicles for angular measurement in (6.14). The transformation is carried out in two steps: translation of distal attachments by (6.13) and then by (6.14). The transformation by Δh_2 may alter the muscle length, but it is not critical problem in this study, because PCSA estimation is not dependent on the length.

6.3 Results

To validate the proposed method, three experiments were performed. Experiment 1 is based on synthetic muscles having uniform geometry and architecture. Experiment 2 uses seven cadaveric specimens of the supraspinatus that exhibit various degrees of inter- and intramuscular variations. Experiment 3 uses seven cadaveric specimens and ultrasonographic imaging from five living subjects. In each experimental setting, muscle data are paired with each other (source and target muscle) to perform the architectural mapping from one to the other and vice versa. Experiments 1 and 2 are based solely on the three-dimensional fascicle data. Note that the proposed method takes the 3D architectural model and the 2D geometric measurements as the source and target data, respectively. Thus, to be compatible, simulated ultrasound is used to obtain a 2D assessment (e.g., mean cross-sectional area, $\bar{c}$, and 2D pennation angle, PA_{2D}) from the 3D fascicle data. The simulated 2D data is referred to as the target muscle in experiments 1 and 2. In those experiments, since both the target muscle and the transformed architectural model have 3D fascicle data, their PCSA can be determined by using the method described in Chapter 3. The PCSA calculated solely from the 3D data is regarded as the true value and compared against the PCSA computed by the mapping method from the 3D to 2D data, which is referred to as $\mathrm{PCSA}_{s\to t}$. The relative error between them is calculated to evaluate the proposed method (i.e., $(\mathrm{PCSA}_{s\to t} - \mathrm{PCSA})/\mathrm{PCSA}$). The results for the PCSA estimation are presented in Tables 6.2, 6.4 and 6.6, respectively.

6.3.1 Experiment 1: Synthetic muscles

For parallel muscles, the relative differences in PCSA between $\mathrm{parallel}_1$ and $\mathrm{parallel}_2$ before the mapping, are 41.8% and −29.5%, respectively. After the mapping, those differences are significantly reduced to −1.5% and −2.5%, respectively. Similarly, for bipennate muscles, the relative differences in PCSA between $\mathrm{bipennate}_1$ and $\mathrm{bipennate}_2$ are significantly lowered from 55.6% to −0.6% and −35.7% to −7.5%, respectively. Results show that the proposed method performs slightly better when the muscle surface shrinks than when it expands, where shrink means that the source muscle has a bigger PCSA than the target muscle. Recall that fascicles located in the outermost layers have some degree of deficiency in that they are surrounded by a few neighboring fascicles only, not completely enclosed by them. That may result in an unbounded Voronoi region, the area of which must be extrapolated or discarded, depending on the deficiency. Generally, shrinking the muscle improves this deficiency problem by increasing the density of fascicle points inside the muscle. On the other hand, expanding the muscle disperses these points, making the problem described above for the outermost regions worse. Consequently this may yield an inaccurate estimation.

Muscle	N	h	$\overline{c}$	PA_{2D}	PCSA
$parallel_1$	390	20.0	453.9	0.0	448.7
$parallel_2$	154	20.0	334.5	0.0	316.5
$bipennate_1$	891	25.0	173.2	16.6	162.8
$bipennate_2$	750	20.0	115.3	13.4	104.6

Table 6.1: Measurements for synthetic muscles. N is the total number of digitized fascicles. h is the longitudinal length of muscle (mm). $\overline{c}$ is the mean cross-sectional area (mm^2). PA_{2D} is the mean pennation angle of fascicles projected onto the mid-longitudinal plane. PCSA is estimated based on the original fascicle data (mm^2).

$Muscle_s$ \ $Muscle_t$	$parallel_1$	$parallel_2$	$bipennate_1$	$bipennate_2$
$parallel_1$		311.6 (−1.5)		
$parallel_2$	437.6 (−2.5)			
$bipennate_1$				103.9 (−0.6)
$bipennate_2$			150.5 (−7.5)	

Table 6.2: PCSA estimation ($PCSA_{s\to t}$) for synthetic muscles. $PCSA_{s\to t}$ is estimated by mapping the architecture from $Muscle_s$ (source muscle) to $Muscle_t$ (target muscle). The relative errors, expressed as percentages, are given in parenthesis.

6.3.2 Experiment 2: Cadaveric specimens

From the seven cadaveric specimens, 42 ordered-pairs are selected to perform the experiment ($\mathcal{T}_{i,j} : S_i \to S_j, i \neq j$). The PCSA of the transformed source muscle is estimated by the proposed method and compared with that of the target muscle. Cadaveric specimens yield a wide range of absolute relative errors (for instance, 0.7 % for $\mathcal{T}_{1,3}$ to 15.2 % for $\mathcal{T}_{1,2}$). This is mainly due to the architectural complexity and the variation between specimens. It is observed that the supraspinatus has non-uniform architecture: bipennate in the anterior region and parallel in the posterior region. Depending on the distribution of the fascicle orientation (i.e., the pennation angle) and the relative thickness of these regions, PCSA may be larger than $\overline{c}$ (e.g., S_1, S_3, S_4 and S_6) or comparable to $\overline{c}$ (e.g., S_2, S_5 and S_7). Since the muscle architecture is not significantly altered in the proposed method, this discrepancy between PCSA and $\overline{c}$ may persist during the mapping. It is also found that some mappings that induce a large shrinkage, such as $\mathcal{T}_{1,2}$, $\mathcal{T}_{1,7}$, $\mathcal{T}_{6,2}$ and $\mathcal{T}_{4,7}$, yield more inaccurate results (above 12.0 %) than others do (below 8.0%). This is caused by the static constraints specified to prevent undesired geometric changes and perturbations of the intramuscular tendon. Recall that the displacement for the mapping is determined by the difference between mean cross-sectional areas of muscles. The bigger the difference, the larger the displacement needed to transform the entire surface. However, too large a displacement may collapse the narrow distal region of the muscle volume or affect the linearity of an intramuscular tendon. In such cases, the associated static constraints adversely affect the transformation. As a result, the PCSA may not reach the targeted value. As PA_{2D} variation is relatively small in this experiment, it is observed that, compared to the transverse

transformation, the longitudinal transformation has little effect on estimating the PCSA.

Statistical analysis of the estimated PCSA is also presented in Table 6.4 and Figure 6.6. Depending on architectural variation and volumetric differences between source and target muscles, the transformation can under- or over-estimate PCSA. However, compared to the distribution of original PCSA for all specimens (standard deviation: ± 153.2), that of the estimated PCSA for each target muscle is much narrower (standard deviation: $\pm 24.6 \sim \pm 35.7$). Furthermore, it is shown that the mean of each distribution ($\overline{\mathrm{PCSA}_{s\to t}}$) is much closer to the true PCSA of the corresponding target muscle ($-5.1\,\% \sim 8.4\,\%$) than that of the original PCSA distribution ($-29.4\,\% \sim 43.3\,\%$).

Muscle	N	h	$\overline{c}$	PA_{2D}	PCSA
S_1	1750	134.2	622.2	6.7	647.0
S_2	729	115.6	424.5	4.4	421.3
S_3	1081	125.9	506.6	8.3	543.8
S_4	1681	135.1	571.5	7.6	613.0
S_5	1294	131.7	698.3	7.5	694.8
S_6	1556	138.6	798.5	6.9	847.0
S_7	829	125.8	416.1	6.3	417.2

Table 6.3: Measurements for cadaveric specimens of the supraspinatus. N is the total number of digitized fascicles. h is the longitudinal length of the muscle (mm). $\overline{c}$ is the mean cross-sectional area (mm^2). PA_{2D} is the mean pennation angle of the fascicles projected onto the mid-longitudinal plane. PCSA is the estimated PCSA based on the original fascicle data (mm^2).

Muscle_s \ Muscle_t	S_1	S_2	S_3	S_4	S_5	S_6	S_7
S_1		485.6 (15.2)	539.9 (0.7)	618.9 (0.9)	716.3 (3.1)	855.5 (1.0)	470.5 (12.7)
S_2	603.4 (−6.7)		484.9 (−10.8)	547.8 (−10.6)	664.7 (−4.3)	758.8 (−10.4)	403.1 (−3.4)
S_3	618.6 (−4.4)	426.5 (1.2)		580.7 (−5.2)	652.7 (−6.0)	790.1 (−6.7)	412.4 (−1.1)
S_4	658.4 (1.7)	471.4 (11.9)	548.1 (0.8)		721.3 (3.8)	822.6 (−2.8)	476.6 (14.2)
S_5	635.9 (−1.7)	441.2 (4.7)	527.2 (−3.0)	586.0 (−4.4)		803.7 (−5.1)	434.7 (4.2)
S_6	670.2 (3.6)	478.3 (13.5)	558.6 (2.7)	622.6 (1.6)	744.8 (7.2)		464.0 (11.2)
S_7	615.4 (−4.8)	437.6 (3.9)	500.9 (−7.8)	564.6 (−7.8)	685.0 (−1.4)	791.6 (−6.5)	
$\overline{\mathrm{PCSA}_{s\to t}}$	633.6 ± 26.2	456.8 ± 24.6	526.6 ± 28.5	586.8 ± 29.5	697.6 ± 35.7	803.7 ± 32.8	443.6 ± 31.4
PCSA	647.0	421.3	543.8	613.0	694.8	847.0	417.2
Error (%)	−2.1	8.4	−3.2	−4.3	0.4	−5.1	6.3

Table 6.4: PCSA estimation ($\mathrm{PCSA}_{s\to t}$) for cadaveric specimens. $\mathrm{PCSA}_{s\to t}$ is the estimated PCSA for Muscle_t (target muscle) computed by mapping the architecture of Muscle_s (source muscle) to the 2D ultrasound version of Muscle_t. The percentage of the relative errors of $\mathcal{T}_{i,j}$ are given in parenthesis. Statistical analysis of $\mathrm{PCSA}_{s\to t}$ for each Muscle_t is given as 'the mean $\pm$ the standard deviation'.

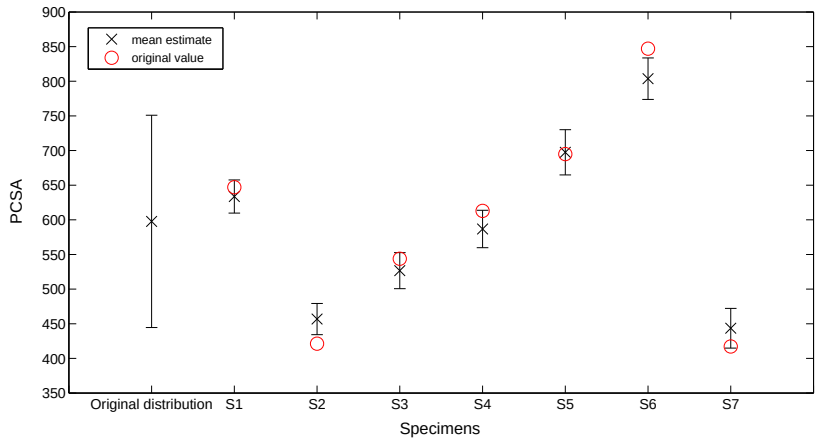

Figure 6.6: Distribution of the PCSA estimation. The distribution of estimated PCSA ($\text{PCSA}_{s\to t}$) for each specimen (in Table 6.4) is compared to its true value of the PCSA (red circle). The distribution of true PCSA for all specimens is also plotted as the leftmost line segment.

6.3.3 Experiment 3: Cadaveric specimens to living subjects

In contrast to the previous two experiments, it is impossible to validate the PCSA estimation in this experiment, because the PCSA of the target muscles are unknown. Thus, only statistical results from experiments on all pairs of muscles are presented in Table 6.6. Similar to experiment 2, lower and upper bounds on the PCSA estimation are determined by the smallest and the biggest source muscles, respectively. Also, the distribution of the estimated PCSA per target muscle is narrow (standard deviation: $\pm 23.7 \sim \pm 29.0$), which indicates that the mean estimates based on cadaveric specimens can be a practical approximation of PCSA for *in vivo* muscle based on ultrasonographic assessment.

Muscle	h	$\bar{c}$	PA_{2D}
US_1	111.4	625.8	11.7
US_2	88.5	549.4	8.4
US_3	81.2	503.2	11.8
US_4	99.1	433.9	14.3
US_5	97.1	515.1	8.9

Table 6.5: Ultrasonographic measurement for the supraspinatus of living subjects. h is the longitudinal length of the muscle (mm). $\bar{c}$ is the mean cross-sectional area (mm^2). PA_{2D} is the mean pennation angle of fascicles identified from the mid-longitudinal image.

6.4 Discussion

PCSA is an architectural parameter that directly determines the maximum capacity of muscle power. An accurate determination of PCSA is needed for both biomechanical and clinical stud-

Muscle$_s$ \ Muscle$_t$	US_1	US_2	US_3	US_4	US_5
S_1	651.2	583.1	528.4	468.8	555.5
S_2	603.0	551.0	498.1	432.7	517.8
S_3	640.5	560.4	527.8	459.7	542.8
S_4	662.7	587.6	540.6	470.3	555.0
S_5	624.1	545.8	505.6	444.4	516.9
S_6	677.9	603.3	553.8	483.7	569.2
S_7	602.7	541.8	482.3	403.9	490.2
$\overline{\text{PCSA}_{s\to t}}$	637.4 ± 29.0	567.6 ± 23.7	519.5 ± 25.2	451.9 ± 27.2	535.4 ± 27.9

Table 6.6: PCSA estimation ($\text{PCSA}_{s\to t}$) for *in-vivo* supraspinatus of living subjects.

ies because reliable functional analysis and associated clinical assessment are highly dependent on the quality of this measure. A commonly used approach is an algebraic formula based on measurement of volume and fascicle length from MRI and ultrasonography, respectively. Since this approach is non-invasive, it can be applied in a broad range of *in-vivo* studies. However, it may under- or over-estimate PCSA because architectural complexity and intramuscular variation are rarely accounted for. On the other hand, cadaveric assessment based on the 3D modeling provides a unique opportunity for an in-depth investigation into PCSA quantification associated with architectural complexity. But it is not straightforward to apply to *in-vivo* studies because comparable data acquisition is not achievable. Therefore, the purpose of this study is to overcome the limitation inherent in each approach by combining them to provide further capacity for PCSA quantification of *in-vivo* muscle. To this end, a subject-specific architecture is approximated by mapping a 3D detailed reference architecture model to the target muscle that is represented by 2D geometric measures. This approximated architecture model is used for PCSA quantification. An architectural reference model is created from cadaveric data whereas geometric measures are obtained from ultrasonographic assessment. Even though customized ultrasound imaging would provide a more extended set of features, this study aims at broader applicability by restricting ultrasonographic assessment to standard protocols that are commonly followed by most clinical studies. The proposed approach is based on the assumption that the same muscles in different subjects are sufficiently similar in terms of overall architectural pattern. Two validation experiments based on synthetic muscle and cadaveric specimens, respectively, demonstrate $0.4 - 8.4\,\%$ errors between original architecture and its approximation, depending on the anatomical complexity. No error analysis is conducted in the third experiment based on cadaveric specimens and ultrasound images because their exact PCSA is unknown. Nevertheless, the distribution of estimation results provides a practical insight into PCSA quantification for *in-vivo* muscle.

The proposed approach can not only be used for static analysis, but it can also be applied to an investigation of dynamic problems associated with muscle contraction or skeletal movement. A variable range of muscle activity can be assessed similarly in terms of 2D geometric measures

in the ultrasound images. Thus, one possible extension of the proposed method is to trace 2D image features in the sequence of ultrasound images obtained during muscle contraction and then fit a 3D architecture model to each of these images. Another possible application is to provide region-specific architectural analysis for *in-vivo* muscle, such as the anterior/posterior or the superficial/deep region. This may need only an additional localization in the ultrasonographic assessment because the architectural model can be easily re-organized into multi-layers or multi-regions.

Although this study provides improved capability for *in-vivo* PCSA estimation, there are some limitations that may be addressed in future work. First, only a small sample of data is considered in the present study. A more thorough validation needs more specimens and a variety of types of muscle. Second, the gap between superficial fascicles and the muscle surface may lead to a significant error, particularly when the muscle expands, because this gap is proportionally scaled with the amount of transformation. Thus, minimizing this gap, by possibly using a tighter surface, could further reduce the estimation error. Lastly, performance of the proposed method is highly sensitive to the consistency between cadaveric and ultrasonographic assessment, such as the orientation and location of their imaging planes. The present study uses only the proximal to distal length of the muscle to compare images. Additional image features, such as shape of cross-sections and bony landmarks, may enhance the reliability to the proposed method. To this end, further investigation into the correspondence between synthetic ultrasound and real ultrasound is needed.

Chapter 7

Conclusion

7.1 Summary

Muscle architecture is a primary determinant of the muscle function associated with body movement. An assessment of muscle architecture is therefore of great importance, not only for investigating anatomical aspects of muscle but also for predicting its functional capacity. Most muscles have a variable degree of complexity in their fascicle arrangement, making it challenging to accurately assess their architecture. Previous cadaveric approaches only take into account a small number of superficial fascicles of specimens. On the other hand, conventional radiological approaches, such as ultrasonography and MRI, examine two-dimensional projected images. Neither of these approaches provides an in-depth three-dimensional image of the entire muscle architecture. This may lead to under- or over-estimation of architectural parameters, consequently affecting the accuracy of associated computational models to be used for various analytical studies.

This thesis focuses on computational modeling of muscle architecture based on its detailed structure. Dissection and digitization are used to capture and reconstruct fascicle trajectories in much greater detail (e.g., sub-mm scale and throughout the volume) from cadaveric specimens than previous studies did. Based on those trajectories, a set of geometric properties representing the volume of each fascicle is estimated. Architectural parameters (e.g., FL, PA, PCSA and MV) are then determined associated with those properties. Those parameters are also used to approximate the surface geometry of the muscle encapsulating all fascicles. This modeling approach provides a unique opportunity to approximate more accurately anatomical and physiological details that were rarely explored but presumed to be significantly correlated with many clinical implications. This study carefully examines and handles the non-uniformity and complexity in the fascicle arrangement that must be appropriately taken into consideration to reconstruct muscle architecture consistently, regardless of muscle type and variability. Furthermore, this study accounts for further complexity that is imposed by some deficiency inherent in the data acquisition. Specifically, it is impossible to computationally replicate exact

muscle architecture by digitizing all fascicles, which only yields coarsely and unevenly sampled data. Nevertheless, the proposed method demonstrates robustness against this deficiency of data and performs consistently over various complexities of muscle architecture (below 10 % error in PCSA estimation). However, it is nearly impossible to obtain detailed architectural data, such as fascicular level of 3D data, from living tissues. That imposes a significant restriction on the cadaveric modeling approach to understand *in vivo* tissues, limited assessment of which is only available using conventional radiological approaches. To overcome this limitation in each approach, this study combines them by associating cadaveric models with ultrasound images computationally. Two applications are discussed. One is to illustrate the correspondence between 3D architecture in space and its projected features on images, providing practical insight into accurate estimation of PA in the ultrasonographic assessment. The other is to approximate *in vivo* architecture by matching detailed reference models with subject-specific measurements on ultrasound images, which enables us to estimate PCSA for *in vivo* muscle. Validation studies demonstrate that this matching method significantly reduces the distribution of PCSA for reference architectures (i.e., standard deviation: $\pm 150.3 \rightarrow \pm 24.6 \sim \pm 35.7$ mm^2), yielding $0.4 - 8.4$ % error between the mean value of this distribution and the known value of PCSA. Thus, the proposed combined approach is an effective way to determine PCSA for living subjects.

Main contributions are:

- Anatomy-based computational modeling of muscle architecture by carefully incorporating anatomical details and complexities.
- A uniform approach to reconstruct muscle geometry and to understand muscle physiology. No adjustment is needed for modeling parameters specific to inter-muscular variability.
- Robust and consistent quantification of architectural parameters (e.g., FL, PA, PCSA and MV) given some deficiencies in the quality of the data in terms of resolution, sampling and noise.
- Determination of architectural patterns (i.e., pennate and non-pennate) and line of action based on the geometric arrangement of fascicles.
- Geometric reconstruction of the muscle surface specific to the underlying architecture and structure, which is potentially useful for anatomical visualization and simulation.
- A novel approach to quantification of PCSA for *in vivo* muscle by combining cadaveric modeling and ultrasonographic assessment.

7.2 Discussion and future work

The proposed methods have been actively used in various anatomical studies [9, 58, 89, 57, 81] that mainly focus on modeling and analyzing architectural and structural aspects of skeletal muscle. The proposed modeling and analytical approach has been shown to provide an in-depth understanding of human skeletal muscle and the potential perspective for more reliable clinical applications. However, to be generally accepted by the clinical and research communities, there exist some problems to overcome. Firstly, most muscles have some range of structural and architectural variability both between cadaveric specimens and between *in vivo* muscles. The proposed method only accounts for the variability of global features. However, to be applicable to translational studies, including surgical and therapeutic treatment, local variations must be taken into account for the personalized and patient-specific modeling. Secondly, the modeling approach based on digitized fascicles needs to be further validated by incorporating other methodologies. For instance, the proposed surface reconstruction could be compared with other reconstructions based on MRI or laser scans. Thirdly, many dynamic human models, such as upper-limb motor control and lower-limb locomotion, commonly use a 1D linear mass-spring model to represent individual muscle force, making it challenging to incorporate the 3D architectural complexity and intra-muscular variation that is necessary to extend the analysis further. As the constitutive modeling approach is shown to effectively simulate some muscle behavior driven by the embedded architecture [13, 81], it is promising to expand this approach to represent more complex problems. Fourthly, the proposed methods rely on some control parameters to be specified, such as re-sampling rate of fascicle points, rejection threshold for the boundary problem and the amount of smoothing for surface reconstruction. Those parameters are currently determined by the experimental observation. To present a more rigorous model, they need to be specified in more analytic manner. Lastly, even though this study provides some insights for predicting functional aspects of muscle, much more needs to be done to clearly determine the correlation between muscle architecture and functional outcome associated with body movement. Further integrative modeling is needed, in conjunction with biomechanical assessment, such as electromyography and dynamometer.

Bibliography

[1] M. Ackerman. The visible human project. In *Proc. IEEE*, volume 86, pages 504–511, 1998.

[2] A. M. Agur, Victor Ng-Thow-Hing, K. A. Ball, E. Fiume, and N. H. McKee. Documentation and three-dimensional modelling of human soleus muscle architecture. *Clinical Anatomy*, 16(4):285–293, 2003.

[3] Irene Albrecht, Jörg Haber, and Hans-Peter Seidel. Construction and animation of anatomically based human hand models. In *SCA '03: Proceedings of the 2003 ACM SIGGRAPH/Eurographics Symposium on Computer Animation*, pages 98–109, Aire-la-Ville, Switzerland, Switzerland, 2003. Eurographics Association.

[4] R. M. Alexander and A. Vernon. The dimensions of knee and ankle muscles and the forces they exert. *Journal of Human Movement Studies*, 1:115–123, 1975.

[5] Brett Allen, Brian Curless, and Zoran Popović. Articulated body deformation from range scan data. *ACM Trans. Graph.*, 21(3):612–619, 2002.

[6] Brett Allen, Brian Curless, and Zoran Popović. The space of human body shapes: reconstruction and parameterization from range scans. In *SIGGRAPH '03: ACM SIGGRAPH 2003 Papers*, pages 587–594, New York, NY, USA, 2003. ACM.

[7] Frank C. Anderson and Marcus G. Pandy. Individual muscle contributions to support in normal walking. *Gait & Posture*, 17:159–169, 2003.

[8] Dragomir Anguelov, Praveen Srinivasan, Daphne Koller, Sebastian Thrun, Jim Rodgers, and James Davis. Scape: shape completion and animation of people. *ACM Trans. Graph.*, 24(3):408–416, 2005.

[9] Takamitsu Arakawa, Zhi Li, Robert Bobotsis, Dongwoon Lee, and Anne M. Agur. Three-dimensional architecture of the plantar intrinsic muscles of the foot. In *Clinical Anatomy*, pages 929–955, 2012.

[10] Amaury Aubel and Daniel Thalmann. Interactive modeling of the human musculature. In *Proceedings of Computer Animation*, pages 125–135, 2001.

[11] M. R. Bénard, J. G. Becher, J. Harlaar, P. A. Huijing, and R. T. Jaspers. Anatomical information is needed in ultrasound imaging of muscle to avoid potentially substantial errors in measurement of muscle geometry. *Muscle Nerve*, 39(5):652–665, 2009.

[12] S. S. Blemker and S. L. Delp. Three-dimensional representation of complex muscle architectures and geometries. *Annals of Biomedical Engineering*, 33(5):661–673, 2005.

[13] S. S. Blemker and S. L. Delp. Rectus femoris and vastus intermedius fiber excursions predicted by three-dimensional muscle models. *Journal of Biomechenics*, 39(8):1383–1391, 2006.

[14] Silvia Blemker. *3D Modeling of Complex Muscle Architecture and Geometry*. PhD thesis, Stanford University, July 2004.

[15] James F. Blinn. A generalization of algebraic surface drawing. *ACM Trans. Graph.*, 1(3):235–256, 1982.

[16] Jules Bloomenthal and Ken Shoemake. Convolution surfaces. In *SIGGRAPH Computer Graphics*, pages 251–256, 1991.

[17] Richard Branda, Douglas R. Pedersen, and James A. Friederich. The sensitivity of muscle force predictions to changes in physiologic cross-sectional area. *Journal of Biomechenics*, 19:589–596, 1986.

[18] Marie-Paule Cani-Gascuel and Mathieu Desbrun. Animation of deformable models using implicit surfaces. *IEEE Transactions on Visualization and Computer Graphics*, 3(1):39–50, 1997.

[19] E. Catmull and R. Rom. A class of local interpolating splines. *Computer Aided Geometric Design*, pages 317–326, 1974.

[20] J. E. Chadwick, D. R. Haumann, and R. E. Parent. Layered construction for deformable animated characters. In *SIGGRAPH Computer Graphics*, pages 243–252, 1989.

[21] David T. Chen and David Zeltzer. Pump it up: computer animation of a biomechanically based model of muscle using the finite element method. In *SIGGRAPH Computer Graphics*, pages 89–98, 1992.

[22] S. L. Delp, J. P. Loan, M. G. Hoy, F. E. Zajac, E. L. Topp, and J. M. Rosen. An interactive graphics-based model of the lower extremity to study orthopaedic surgical procedures. *IEEE Transactions on Biomedical Engineering*, 37:757–767, 1990.

[23] Scott L. Delp and J. Peter Loan. A computational framework for simulating and analyzing human and animal movement. *Computing in Science and Engg.*, 2:46–55, September 2000.

[24] E. Dow and S. Semwal. A framework for modeling the human muscle and bone shapes. In *Proceedings of the Third International Conference on CAD and Computer Graphics*, pages 110–113, 1993.

[25] Andrew Fitzgibbon, Maurizio Pilu, and Robert B. Fisher. Direct least square fitting of ellipses. *IEEE Trans. Pattern Anal. Mach. Intell.*, 21:476–480, May 1999.

[26] M. Froeling, A. J. Nederveen, D. F. Heijtel, A. Lataster, C. Bos, K. Nicolay, M. Maas, M. R. Drost, and G. J. Strijkers. Diffusion-tensor MRI reveals the complex muscle architecture of the human forearm. *Journal of Magnetic Resonance Imaging*, 36:237–248, July 2012.

[27] C. Gans and F. de Vree. Functional bases of fiber length and angulation in muscle. *Journal of Morphology*, 192:63–85, 1987.

[28] H. S. Gasser and A. V. Hill. The dynamics of mucular contraction. In *Royal Society of London Proceedings*, pages 398–437, 1924.

[29] Sarah F. F. Gibson and Brian Mirtich. A survey of deformable modeling in computer graphics. Technical report, Mitsubishi Electric Research Laboratories, 1997.

[30] A. W. J. Gielen, C. W. J. Oomens, P. H. M. Bovendeerd, T. Arts, and J. D. Janssen. A finite element approach for skeletal muscle using a distributed moment model of contraction. *Computer Methods in Biomechanics and Biomedical Engineering*, 3(3):231–244, 2000.

[31] A. M. Herrmann and S. L. Delp. Moment arm and force-generating capacity of the extensor carpi ulnaris after transfer to the extensor carpi radialis brevis. *The Journal of Hand Surgery*, 24:1083–1090, 1999.

[32] Walter Herzog and Henk E. D. J. Keurs. Force-length relation of in-vivo human rectus femoris muscles. *Pflügers Archiv European Journal of Physiology*, 411:642–647, 1988.

[33] A. V. Hill. *First and Last Experiments in Muscle Mechanics*. Cambridge University Press, 1970.

[34] Gentaro Hirota, Susan Fisher, Andrei State, Chris Lee, and Henry Fuchs. An implicit finite element method for elastic solids in contact. In *Computer Animation*, 2001.

[35] Katherine R. S. Holzbaura, Wendy M. Murrayc, Garry E. Gold, and Scott L. Delp. Upper limb muscle volumes in adult subjects. *Journal of Biomechenics*, 40:742–749, 2007.

[36] A. F. Huxley. Muscle structure and theories of contraction. *Progress in Biophysics and Biophysical Chemistry*, 7:255–318, 1957.

[37] A. F. Huxley and R. M. Simmons. Proposed mechanism of force generation in striated muscle. *Nature*, 233:533–538, 1971.

[38] R. H. Jensen and D. T. Davy. An investigation of muscle lines of action about the hip: A centroid line approach vs the straight line approach. *Journal of Biomechanics*, 8(2):105–110, 2004.

[39] David Jones, Arnold De Haan, and Joan Round. *Skeletal Muscle – Form and Function.* Churchill Livingstone, 2004.

[40] Tao Ju, Scott Schaefer, and Joe Warren. Mean value coordinates for closed triangular meshes. *ACM Trans. Graph.*, 24(3):561–566, July 2005.

[41] S Kim, R Bleakney, E Boynton, K Ravichandiran, T Rindlisbacher, N McKee, and A Agur. Investigation of the static and dynamic musculotendinous architecture of supraspinatus. *Clinical Anatomy*, 23:48–55, 2010.

[42] S. Y. Kim, E. L. Boynton, K. Ravichandiran, L. Y. Fung, R. Bleakney, and A. M. Agur. Three-dimensional study of the musculotendinous architecture of supraspinatus and its functional correlations. *Clinical Anatomy*, 20:648–655, 2007.

[43] Stephen M. Klischab and Jeffrey C. Lotza. Application of a fiber-reinforced continuum theory to multiple deformations of the annulus fibrosus. *Journal of Biomechanics*, 32(10):1027–1036, 1999.

[44] Koji Komatsu. Human skin model capable of natural shape variation. *The Visual Computer*, 3(5):265–271, 1988.

[45] J. H. Koolstra, T. M. G. J. van Eijden, and W. A. Weijs. An iterative procedure to estimate muscle lines of action in vivo. *Journal of Biomechenics*, 22:911–920, 1989.

[46] François Labelle and Jonathan Richard Shewchuk. Isosurface stuffing: fast tetrahedral meshes with good dihedral angles. *ACM Trans. Graph.*, 26:28–37, July 2007.

[47] Joseph Langenderfera, Seth A. Jerabekb, Vijay B. Thangamanib, John E. Kuhnc, and Richard E. Hughes. Musculoskeletal parameters of muscles crossing the shoulder and elbow and the effect of sarcomere length sample size on estimation of optimal muscle length. *Clinical Biomechanics*, 19:664–670, 2004.

[48] Dongwoon Lee, Michael Glueck, Azam Khan, Ken Jackson, and Eugene Fiume. Modeling and simulation of skeletal muscle for computer graphics: A survey. *Foundations and Trends in Computer Graphics and Vision*, 7(4):229–276, 2012.

[49] Dongwoon Lee, Soo Kim, Ken Jackson, Eugene Fiume, and Anne Agur. A practical approach to in vivo quantification of physiological cross-sectional area for human skeletal

muscle. *Computer Methods in Biomechanics and Biomedical Engineering (submitted)*, 2015.

[50] Dongwoon Lee, Zhi Li, Qazi Zain Sohail, Ken Jackson, Eugene Fiume, and Anne Agur. A three-dimensional approach to pennation angle estimation for human skeletal muscle. *Computer Methods in Biomechanics and Biomedical Engineering*, 18(13):1474–1484, 2014.

[51] Dongwoon Lee, Kajeandra Ravichandiran, Ken Jackson, Eugene Fiume, and Anne Agur. Robust estimation of physiological cross-sectional area and geometric reconstruction for human skeletal muscle. *Journal of Biomechanics*, 45(8):1507–13, 2012.

[52] Yuencheng Lee, Demetri Terzopoulos, and Keith Walters. Realistic modeling for facial animation. In *SIGGRAPH Computer Graphics*, pages 55–62, 1995.

[53] Robson Lemos, Marcelo Epstein, Walter Herzog, and Brian Wyvill. Realistic skeletal muscle deformation using finite element analysis. In *Proceedings of the XIV Brazilian Symposium on Computer Graphics and Image Processing*, pages 192–199, 2001.

[54] Randall J. LeVeque. *Finite Volume Methods for Hyperbolic Problems*. Cambridge University Press, 2002.

[55] David I. W. Levin, Benjamin Gilles, Burkhard Madler, and Dinesh K. Pai. Extracting skeletal muscle fiber fields from noisy diffusion tensor data. *Medical Image Analysis*, 15:340–353, 2011.

[56] J. P. Lewis, Matt Cordner, and Nickson Fong. Pose space deformation: a unified approach to shape interpolation and skeleton-driven deformation. In *SIGGRAPH '00: Proceedings of the 27th Annual Conference on Computer Graphics and Interactive Techniques*, pages 165–172, New York, NY, USA, 2000. ACM Press/Addison-Wesley Publishing Co.

[57] Zhi Li, Jeremy P.M. Mogk, Dongwoon Lee, Jacobo Bibliowicz, and Anne M. Agur. Development of an architecturally comprehensive database of forearm flexors and extensors from a single cadaveric specimen. *Computer Methods in Biomechanics and Biomedical Engineering: Imaging and Visualization*, 3:3–12, 2014.

[58] Zhi Li, Kajeandra Ravichandiran, Dongwoon Lee, Nancy Mckee, and Anne M. Agur. An architecturally comprehensive 3d computer model of the intrinsic musculotendinous structures of the hand. In *Clinical Anatomy*, pages 929–955, 2012.

[59] R. L. Lieber and J. Friden. Functional and clinical significance of skeletal muscle architecture. *Muscle Nerve*, 23:1647–1666, November 2000.

[60] Yong-You Ma, Hui Zhang, and Shou-Wei Jiang. Realistic modeling and animation of human body based on scanned data. *J. Comput. Sci. Technol.*, 19(4):529–537, 2004.

[61] J. Mendez and A. Keys. Density and composition of mammalian muscle. *Metabolism*, 9:184–188, 1960.

[62] K. H. Min, S. M. Baek, G. A. Lee, H. Choi, and C. M. Park. Anatomically-based modeling and animation of human upper limbs. In *Proceedings of International Conference on Human Modeling and Animation*, 2000.

[63] Laurent Moccozet and Nadia Magnenat Thalmann. Dirichlet free-form deformations and their application to hand simulation. In *CA '97: Proceedings of the Computer Animation*, page 93, Washington, DC, USA, 1997. IEEE Computer Society.

[64] M. Mooney. A theory of large elastic deformation. *Journal of Applied Physics*, 11:582–592, 1940.

[65] Wendy M. Murray, Thomas S. Buchanan, and Scott L. Delp. The isometric functional capacity of muscles that cross the elbow. *Journal of Biomechanics*, 33:943–952, 2000.

[66] A. I. Namburete, M. Rana, and J. M. Wakeling. Computational methods for quantifying in vivo muscle fascicle curvature from ultrasound images. *Journal of Biomechanics*, 44:2538–2543, 2011.

[67] Andrew Nealen, Matthias Mueller, Richard Keiser, Eddy Boxerman, and Mark Carlson. Physically based deformable models in computer graphics. *Computer Graphics Forum*, 25(4):809–836, December 2006.

[68] Luciana Porcher Nedel and Daniel Thalmann. Real time muscle deformations using mass-spring systems. In *Proceedings of Computer Graphics International*, pages 156–165. IEEE, 1998.

[69] Victor Ng-Thow-Hing. *Anatomically-Based Models For Physical and Geometric Reconstruction of Humans and Other Animals*. PhD thesis, University of Toronto, Toronto, Canada, June 2001.

[70] Victor Ng-Thow-Hing and E. Fiume. B-spline solids as physical and geometric muscle models for musculoskeletal systems. In *Proceedings of the VIIth International Symposium of Computer Simulation in Biomechanics*, pages 68–71, 1999.

[71] C. W. J. Oomens, M. Maenhout, C. H. van Oijen, M. R. Drost, and F. P. Baaijens. Finite element modelling of contracting skeletal muscle. *Philosophical Transactions: Biological Sciences*, 358:1453–1460, 2003.

[72] Marcus G. Pandy. Computer modeling and simulation of human movement. *Annual Review of Biomedical Engineering*, 3:245–273, 2001.

[73] Sang Il Park and Jessica K. Hodgins. Capturing and animating skin deformation in human motion. *ACM Trans. Graph.*, 25(3):881–889, 2006.

[74] Sang Il Park and Jessica K. Hodgins. Data-driven modeling of skin and muscle deformation. *ACM Trans. Graph.*, 27(3):1–6, 2008.

[75] William H. Press, Brian P. Flannery, Saul A. Teukolsky, and William T. Vetterling. *Numerical Recipes in C: The Art of Scientific Computing*. Cambridge University Press, 1992.

[76] M. Rana and J. M. Wakeling. In-vivo determination of 3D muscle architecture of human muscle using free hand ultrasound. *Journal of Biomechanics*, 44:2129–2135, 2011.

[77] Kajeandra Ravichandiran, Mayoorendra Ravichandiran, M. L. Oliver, K. S. Singh, N. H. McKee, and A. M. Agur. Determining physiological cross-sectional area of extensor carpi radialis longus and brevis as a whole and by regions using 3D computer muscle models created from digitized fiber bundle data. *Comput. Methods Prog. Biomed.*, 95:203–212, September 2009.

[78] Kajeandra Ravichandiran, Mayoorendra Ravichandiran, M. L. Oliver, K. S. Singh, N. H. McKee, and A. M. Agur. Fibre bundle element method of determining physiological cross-sectional area from three-dimensional computer muscle models created from digitised fibre bundle data. *Comput. Methods Prog. Biomed.*, 13:741–748, December 2010.

[79] A. L. Rosatelli, Kajeandra Ravichandiran, and A. M. Agur. Three-dimensional study of the musculotendinous architecture of lumbar multifidus and its functional implications. *Clinical Anatomy*, 21:539–546, 2008.

[80] R. D. Sacks and R. R. Roy. Architecture of the hindlimb muscles of cats: functional significance. *Journal of Morphology*, 173:185–195, 1982.

[81] C. Antonio Sánchez, John E. Lloyd, Sidney Fels, and Purang Abolmaesumi. Embedding digitized fibre fields in finite element models of muscles. *Computer Methods in Biomechanics and Biomedical Engineering: Imaging & Visualization*, 2(4):223–236, 2014.

[82] Peter Sand, Leonard McMillan, and Jovan Popović. Continuous capture of skin deformation. *ACM Trans. Graph.*, 22(3):578–586, 2003.

[83] Ferdi Scheepers, Richard E. Parent, Wayne E. Carlson, and Stephen F. May. Anatomy-based modeling of the human musculature. In *SIGGRAPH Computer Graphics*, pages 163–172, 1997.

[84] P. Schenk, T. Siebert, P. Hiepe, D. Gullmar, J. R. Reichenbach, C. Wick, R. Blickhan, and M. Böl. Determination of three-dimensional muscle architectures: validation of the dti-based fiber tractography method by manual digitization. *Journal of Anatomy*, 223:61–68, 2013.

[85] Thomas W. Sederberg and Scott R. Parry. Free-form deformation of solid geometric models. In *SIGGRAPH Computer Graphics*, pages 151–160, 1986.

[86] Hyewon Seo and Nadia Magnenat-Thalmann. An automatic modeling of human bodies from sizing parameters. In *I3D '03: Proceedings of the 2003 Symposium on Interactive 3D Graphics*, pages 19–26, New York, NY, USA, 2003. ACM.

[87] Karan Singh and Eugene Fiume. Wires: a geometric deformation technique. In *SIGGRAPH '98: Proceedings of the 25th Annual Conference on Computer Graphics and Interactive Techniques*, pages 405–414, New York, NY, USA, 1998. ACM.

[88] Peter-Pike J. Sloan, Charles F. Rose, III, and Michael F. Cohen. Shape by example. In *I3D '01: Proceedings of the 2001 Symposium on Interactive 3D Graphics*, pages 135–143, New York, NY, USA, 2001. ACM.

[89] Zain Sohail, Kate Sauks, Kajeandra Ravichandiran, Judi Laprade, Dongwoon Lee, and Anne M. Agur. A 3d model of vastus medialis oblique fiber bundle architecture. In *Clinical Anatomy*, pages 929–955, 2012.

[90] O. Sorkine, D. Cohen-Or, Y. Lipman, M. Alexa, C. Rössl, and H.-P. Seidel. Laplacian surface editing. In *Proceedings of the 2004 Eurographics/ACM SIGGRAPH symposium on Geometry processing*, SGP '04, pages 175–184, New York, NY, USA, 2004. ACM.

[91] Jack T Stern. Computer modelling of gross muscle dynamics. *Journal of biomechanics*, 7(5):411–28, 1974.

[92] Gilbert Strang and George Fix. *An Analysis of the Finite Element Method, 2nd Edition.* Wellesley-Cambridge, 2008.

[93] C. Y. Tang, G. Zhang, and C. P. Tsui. A 3D skeletal muscle model coupled with active contraction of muscle fibres and hyperelastic behaviour. *Journal of Biomechanics*, 42(7):865–872, 2009.

[94] J. Teran, S. Blemker, V. Ng Thow Hing, and R. Fedkiw. Finite volume methods for the simulation of skeletal muscle. In *SCA '03: Proceedings of the 2003 ACM SIGGRAPH/Eurographics Symposium on Computer Animation*, pages 68–74, 2003.

[95] Joseph Teran, Eftychios Sifakis, Silvia S. Blemker, Victor Ng-Thow-Hing, Cynthia Lau, and Ronald Fedkiw. Creating and simulating skeletal muscle from the visible human data set. *IEEE Transactions on Visualization and Computer Graphics*, 11(3):317–328, 2005.

[96] Daniel Thalmann, Jianhua Shen, and Eric Chauvineau. Fast realistic human body deformations for animation and vr applications. In *CGI '96: Proceedings of the 1996 Conference on Computer Graphics International*, pages 166–174, 1996.

[97] A. J. van den Bogerta, K. G. M. Gerritsena, and G. K. Cole. Human muscle modelling from a user's perspective. *Journal of Electromyography and Kinesiology*, 8:119–124, 1998.

[98] C. C. Van Donkelaar, L. J. Kretzers, P. H. Bovendeerd, L. M. Lataster, K. Nicolay, J. D. Janssen, and M. R. Drost. Diffusion tensor imaging in biomechanical studies of skeletal muscle function. *Journal of Anatomy*, 194:79–88, 1999.

[99] A. J. van Soest and M. F. Bobbert. The contribution of muscle properties in the control of explosive movements. *Biological Cybernetics*, 69:195–204, 1993.

[100] P. H. van Spronsen, J. Valk, W. A. Weijs, and B. Prahl-Andersen. Analysis of masticatory muscle orientation in adults by means of MRI. *Acta Anatomica*, 130:96–97, 1987.

[101] D. R. Veronda and R. A. Westmann. Mechanical characterization of skin-finite deformations. *Journal of Biomechanics*, 3(1):111–124, 1970.

[102] S. R. Ward, C. W. Kim, C. M. Eng, L. J. Gottschalk, A. Tomiya, S. R. Garfin, and R. L. Lieber. Architectural analysis and intraoperative measurements demonstrate the unique design of the multifidus muscle for lumbar spine stability. *Journal of Bone and Joint Surgery, American Volume*, 91:176–185, 2009.

[103] S. R. Ward and R. L. Lieber. Density and hydration of fresh and fixed human skeletal muscle. *Journal of Biomechanics*, 38:2317–2320, 2005.

[104] Jane Wilhelms. Animals with anatomy. *IEEE Comput. Graph. Appl.*, 17(3):22–30, 1997.

[105] Jane Wilhelms and Allen Van Gelder. Anatomically based modeling. In *SIGGRAPH Computer Graphics*, pages 173–180, 1997.

[106] Brian Wyvill and Geoff Wyvill. Field functions for implicit surfaces. *The Visual Computer*, 5(1–2):75–82, 1989.

[107] Can A. Yucesoy, Bart H. F. J. M. Koopman, Peter A. Huijing, and Henk J. Grootenboer. Three-dimensional finite element modeling of skeletal muscle using a two-domain approach: linked fiber-matrix mesh model. *Journal of Biomechanics*, 35(9):1253–1262, 2002.

[108] George Ireneus Zahalak. A distribution-moment approximation for kinetic theories of muscular contraction. *Mathematical Biosciences*, 55(1–2):89–114, 1981.

[109] F. E. Zajac. Muscle and tendon: properties, models, scaling, and application to biomechanics and motor control. *Critical Reviews in Biomedical Engineering*, 17:359–411, 1989.

[110] F. E. Zajac. How musculotendon architecture and joint geometry affect the capacity of muscles to move and exert force on objects: a review with application to arm and forearm tendon transfer design. *The Journal of Hand Surgery*, 17(5):799–804, 1992.

[111] F. E. Zajac and M. E. Gordon. Determining muscle's force and action in multi-articular movement. *Exercise and Sport Sciences Reviews*, 17:187–230, 1989.

[112] Qing-hong Zhu, Yan Chen, and Arie Kaufman. Real-time biomechanically-based muscle volume deformation using FEM. *Computer Graphics Forum*, 17(3):275–284, December 2001.

[113] Yongning Zhu and Robert Bridson. Animating sand as a fluid. *ACM Trans. Graph.*, 24:965–972, July 2005.

[114] Victor Brian Zordan, Bhrigu Celly, Bill Chiu, and Paul C. DiLorenzo. Breathe easy: model and control of simulated respiration for animation. In *SCA '04: Proceedings of the 2004 ACM SIGGRAPH/Eurographics Symposium on Computer Animation*, pages 29–37, 2004.